

Carnegie Supernova Project-I & -II: Measurements of H_0 using Cepheid, TRGB, and SBF Distance Calibration to Type Ia Supernovae*

SYED A. UDDIN ^{1,2,3,4} CHRISTOPHER R. BURNS ¹ M M. PHILLIPS ⁵ NICHOLAS B. SUNTZEFF ²
WENDY L. FREEDMAN ^{6,7} PETER J. BROWN ² NIDIA MORRELL ⁵ MARIO HAMUY ^{8,9} KEVIN KRISCIUNAS ²
LIFAN WANG ² ERIC Y. HSIAO ¹⁰ ARIEL GOOBAR ¹¹ SAUL PERLMUTTER ^{12,13} JING LU ¹⁰
MAXIMILIAN STRITZINGER ¹⁴ JOSEPH P. ANDERSON ¹⁵ CHRIS ASHALL ¹⁶ PETER HOEFLICH ¹⁰
BENJAMIN J. SHAPPEE ¹⁷ S. E. PERSSON ⁶ ANTHONY L. PIRO ⁶ E BARON ^{18,19,20} CARLOS CONTRERAS ⁵
LLUÍS GALBANY ^{21,22} SAHANA KUMAR ¹⁰ MELISSA SHAHBANDEH ¹⁰ SCOTT DAVIS ²³ JORGE ANAIS ²⁴
LUIS BUSTA ⁵ ABDO CAMPILAY ^{5,25} SERGIO CASTELLÓN, ⁵ CARLOS CORCO, ^{5,26} TIARA DIAMOND ^{10,27}
CHRISTA GALL ²⁸ CONSUELO GONZALEZ, ⁵ SIMON HOLMBO ¹⁴ MIGUEL ROTH ^{5,29} JACQUELINE SERÓN ³⁰
FRANCESCO TADDIA ³¹ SIMÓN TORRES, ²⁶ CHARLES BALTAY ³² GASTÓN FOLATELLI ³³ ELLIE HADJIYSKA, ³²
MANSI KASLIWAL ³⁴ PETER E. NUGENT ^{12,13} DAVID RABINOWITZ, ³² AND STUART D. RYDER ^{35,36}

¹ *Observatories of the Carnegie Institution for Science, 813 Santa Barbara St, Pasadena, CA, 91101, USA*

² *George P. and Cynthia Woods Mitchell Institute for Fundamental Physics and Astronomy, Texas A&M University, Department of Physics and Astronomy, College Station, TX 77843, USA*

³ *US Naval Observatory, 3450 Massachusetts Ave NW, Washington, DC 20392*

⁴ *Center for Space Studies, American Public University System, 111 W. Congress Street, Charles Town, WV 25414, USA*

⁵ *Carnegie Observatories, Las Campanas Observatory, Casilla 601, La Serena, Chile*

⁶ *Observatories of the Carnegie Institution for Science, 813 Santa Barbara St., Pasadena, CA 91101, USA*

⁷ *Department of Astronomy and Astrophysics, University of Chicago, 5640 S. Ellis Ave, Chicago, IL 60637, USA*

⁸ *Hagler Institute for Advanced Studies, Texas A&M University, College Station, TX 77843, USA*

⁹ *Fundación Chilena de Astronomía, El Vergel 2252, Santiago, Chile*

¹⁰ *Department of Physics, Florida State University, 77 Chieftan Way, Tallahassee, FL 32306, USA*

¹¹ *The Oskar Klein Centre, Department of Physics, Stockholm University, SE-106 91 Stockholm, Sweden*

¹² *Lawrence Berkeley National Laboratory, Department of Physics, 1 Cyclotron Road, Berkeley, CA 94720, USA*

¹³ *Astronomy Department, University of California at Berkeley, Berkeley, CA 94720, USA*

¹⁴ *Department of Physics and Astronomy, Aarhus University, Ny Munkegade 120, DK-8000 Aarhus C, Denmark*

¹⁵ *European Southern Observatory, Alonso de Córdova 3107, Casilla 19, Santiago, Chile*

¹⁶ *Department of Physics, Virginia Tech, Blacksburg, VA 24061, USA*

¹⁷ *Institute for Astronomy, University of Hawaii, 2680 Woodlawn Drive, Honolulu, HI 96822, USA*

¹⁸ *Planetary Science Institute, 1700 East Fort Lowell Road, Suite 106, Tucson, AZ 85719-2395, USA*

¹⁹ *Hamburger Sternwarte, Gojenbergsweg 112, D-21029 Hamburg, Germany*

²⁰ *Homer L. Dodge Department of Physics and Astronomy, University of Oklahoma, 440 W. Brooks, Rm 100, Norman, OK 73019-2061, USA*

²¹ *Institute of Space Sciences (ICE, CSIC), Campus UAB, Carrer de Can Magrans, s/n, E-08193 Barcelona, Spain*

²² *Institut d'Estudis Espacials de Catalunya (IEEC), E-08034 Barcelona, Spain*

²³ *Department of Physics, University of California, 1 Shields Avenue, Davis, CA 95616-5270, USA*

²⁴ *Centro de Astronomía (CITEVA), Universidad de Antofagasta, Av. Angamos 601, Antofagasta, Chile*

²⁵ *Departamento de Física, Universidad de La Serena, Cisternas 1200, La Serena, Chile*

²⁶ *SOAR Telescope, Casilla 603, La Serena, Chile*

²⁷ *Laboratory of Observational Cosmology, Code 665, NASA Goddard Space Flight Center, Greenbelt, MD 20771, USA*

²⁸ *DARK, Niels Bohr Institute, University of Copenhagen, Jagtvej 128, 2200 Copenhagen, Denmark*

²⁹ *GMTO Corporation, Presidente Riesco 5335, Of. 501, Nueva Las Condes, Santiago*

³⁰ *Cerro Tololo Inter-American Observatory/NSF's NOIRLab, Casilla 603, La Serena, Chile*

³¹ *The Oskar Klein Centre, Department of Astronomy, Stockholm University, SE-106 91 Stockholm, Sweden*

Corresponding author: Syed A. Uddin

saushuvo@gmail.com

* This paper includes data gathered with the 6.5 meter Magellan Telescopes located at Las Campanas Observatory, Chile.

arXiv:2308.01875v2 [astro-ph.CO] 25 Oct 2023

³²*Department of Physics, Yale University, 217 Prospect Street, New Haven, CT 06511, USA*

³³*Facultad de Ciencias Astronómicas y Geofísicas, Universidad Nacional de La Plata, Instituto de Astrofísica de La Plata (IALP), CONICET, Paseo del Bosque S/N, B1900FWA La Plata, Argentina*

³⁴*Caltech, 1200 East California Boulevard, MC 249-17, Pasadena, CA 91125, USA*

³⁵*School of Mathematical and Physical Sciences, Macquarie University, NSW 2109, Australia*

³⁶*Astronomy, Astrophysics and Astrophotonics Research Centre, Macquarie University, Sydney, NSW 2109, Australia*

Submitted to ApJ

ABSTRACT

We present an analysis of Type Ia Supernovae (SNe Ia) from both the Carnegie Supernova Project I (CSP-I) and II (CSP-II), and extend the Hubble diagram from the optical to the near-infrared wavelengths (*uBgVriYJH*). We calculate the Hubble constant, H_0 , using various distance calibrators: Cepheids, Tip of the Red Giant Branch (TRGB), and Surface Brightness Fluctuations (SBF). Combining all methods of calibrations, we derive $H_0 = 71.76 \pm 0.58$ (stat) ± 1.19 (sys) $\text{km s}^{-1} \text{Mpc}^{-1}$ from *B*-band, and $H_0 = 73.22 \pm 0.68$ (stat) ± 1.28 (sys) $\text{km s}^{-1} \text{Mpc}^{-1}$ from *H*-band. By assigning equal weight to the Cepheid, TRGB, and SBF calibrators, we derive the systematic errors required for consistency in the first rung of the distance ladder, resulting in a systematic error of $1.2 \sim 1.3 \text{ km s}^{-1} \text{Mpc}^{-1}$ in H_0 . As a result, relative to the statistics-only uncertainty, the tension between the late-time H_0 we derive by combining the various distance calibrators and the early-time H_0 from the Cosmic Microwave Background is reduced. The highest precision in SN Ia luminosity is found in the *Y* band (0.12 ± 0.01 mag), as defined by the intrinsic scatter (σ_{int}). We revisit SN Ia Hubble residual-host mass correlations and recover previous results that these correlations do not change significantly between the optical and the near-infrared wavelengths. Finally, SNe Ia that explode beyond 10 kpc from their host centers exhibit smaller dispersion in their luminosity, confirming our earlier findings. Reduced effect of dust in the outskirts of hosts may be responsible for this effect.

1. INTRODUCTION

A solution to the field equations of the General Theory of Relativity (Einstein 1915) points to a Universe that must be expanding. Aleksandr Friedmann and George Lemaître independently predicted this Universal expansion in the early twentieth century (Friedmann 1922; Lemaître 1927). Edwin Hubble used the Period-Luminosity relation of classical Cepheid variable stars (Leavitt Law; Leavitt & Pickering 1912) to measure distances to external galaxies (Hubble 1926), revolutionizing the understanding of the distance scale of the Universe. These new distance measurements and techniques, in turn, led to estimates of the local expansion of the Universe which is commonly parameterized as the Hubble constant, H_0 . This constant is one of the six fundamental parameters in the Λ CDM cosmological framework, where the expansion of the Universe is accelerating due to an unknown force called dark energy (Perlmutter et al. 1999, Riess et al. 1998).

The first measurements of H_0 using distances tied to the 1926 work of Hubble and velocities from Slipher (Slipher 1915, 1917) were made by Lemaître (Lemaître 1927) and Robertson (Robertson 1928), who found values of 625 and 490 $\text{km s}^{-1} \text{Mpc}^{-1}$. Until the 1927 work of Lemaître, where an expansion in the form of

$V/c = (R'/R) r$ was predicted¹, there was some confusion whether there was a quadratic term in the distance-velocity relationship in de Sitter’s “Solution B” (de Sitter 1916a,b), an empty and expanding universe with a cosmological constant. Both Lemaître and Robertson showed that in their world models, the local expansion should be linear in theory, and they fit the distance-velocity relationship as such. Neither stressed that the data required a linear fit.

Hubble published his value for the expansion of the universe in 1929 of 500 $\text{km s}^{-1} \text{Mpc}^{-1}$ (Hubble 1929). He did not cite the source of the distances and velocities used, but it is clear that most of the velocities came from Slipher. These values of H_0 are much higher than the modern values due to a number of factors including stellar crowding, the admixture of W Virginis (Pop II) Cepheids, and refinement in the photometric scale. As with the previous work of Lemaître and Robinson, Hubble fit a linear law but did not show that the fit must be linear. What was new was that he plotted the data in his famous Figure 1 which showed that a linear relation

¹ In Lemaître’s expression V is the recession velocity, c is the speed of light in vacuum, r is the distance from earth, and R'/R is a constant in which R is the scale factor. Lemaître calculated R'/R to be $0.68 \times 10^{-27} \text{ cm}^{-1}$.

was a good fit to the data. The issue of the order of the fit was laid to rest in the monumental paper of [Hubble & Humason \(1931\)](#) when the new data on galaxy velocities and magnitudes from Mt. Wilson became available, which extended out to the Leo and Ursa Majoris clusters, and velocities up to $20,000 \text{ km s}^{-1}$. We now refer to the linear relationship between distance and velocity as the “Hubble-Lemaître” law². Excellent reviews of the history of early measurements of the Hubble constant can be found in [Kragh & Smith \(2003\)](#) and somewhat tongue-in-cheek in [Trimble \(2013\)](#).

The value of H_0 published by Hubble gave the Universe an age of 2 billion years, while the radioactive dating showed that the Earth was 3 billion years old³. This apparent contradiction was not resolved until the mid-1950s when [Humason et al. \(1956\)](#) published a reduced value of $H_0 = 180 \pm 36 \text{ km s}^{-1}\text{Mpc}^{-1}$. While [Sandage \(1958\)](#) reduced it further down to $75 \pm 25 \text{ km s}^{-1}\text{Mpc}^{-1}$, after a series of papers, [Sandage & Tammann \(1982\)](#) reached a global value of $H_0 = 50 \pm 7 \text{ km s}^{-1}\text{Mpc}^{-1}$. A number of H_0 measurements ranging between 100 and $200 \text{ km s}^{-1}\text{Mpc}^{-1}$ were also published during this time by Sydney van den Berg and Gerard deVaucouleurs (see [Trimble 1996](#) for a historical perspective on this).

Besides Cepheids, a number of other methods have been developed to measure extra-galactic distances (and H_0). **For example, [Sandage & Tammann \(1974\)](#) introduced a distance ladder concept for extra-galactic H II regions.** [Tully & Fisher \(1977\)](#) proposed a method in which the line profile widths of global neutral hydrogen in spiral galaxies are correlated with their luminosity, and obtained $H_0 = 80 \pm 8 \text{ km s}^{-1}\text{Mpc}^{-1}$. [Mould et al. \(1980\)](#) also used the Tully-Fisher relation in the near-infrared to obtain $H_0 = 65 \pm 4 \text{ km s}^{-1}\text{Mpc}^{-1}$. **[Jacoby et al. \(1992\)](#) summarizes various methods on extra-galactic distance measurements.**

In recent times, a number of other methods have emerged such as the Tip of the Red Giant Branch method (TRGB; [Madore & Freedman 1995](#)), Surface Brightness Fluctuations (SBF; [Tonry & Schneider 1988](#), [Ferrarese et al. 2000](#)), time-delay cosmography ([Refsdal 1964](#), [Shajib et al. 2020](#)), and more recently, gravitational-wave standard sirens ([Holz & Hughes 2005](#), [Vitale & Chen 2018](#)). These extra-galactic distance measurements (except the time-delay cosmography⁴ and the gravitational-wave standard sirens) are anchored to geometrical distances, such as stellar par-

allaxes, detached eclipsing binaries ([Pietrzyński et al. 2019](#)), and masers ([Reid et al. 2019](#)). However, most of these methods are for nearby galaxies where peculiar velocities from local matter density fluctuations are of a similar order of magnitude as the cosmological redshift. Therefore, more distant cosmological probes are required to accurately measure the expansion rate.

The first use of SNe to measure the expansion rate of the Universe was published in [Zwicky et al. \(1961\)](#) who reported an upper limit of H_0 of $175 \text{ km s}^{-1}\text{Mpc}^{-1}$ from the observations of 10 SNe⁵ in the Virgo cluster. The first use of SN Ia in the Hubble flow was presented in [Kowal \(1968\)](#), who derived an average absolute magnitude of $-16.8 + 5\log(H_0/100)$ from 33 SNe Ia, with a dispersion of 0.6 mag. Later, [Branch & Patchett \(1973\)](#) made an extensive spectroscopic study of SNe Ia, determined a peak luminosity of $-20.8^{+0.9}_{-0.7}$ mag, and estimated $H_0 = 40^{+25}_{-13} \text{ km s}^{-1}\text{Mpc}^{-1}$. In the following year, [Kirshner & Kwan \(1974\)](#) used Type II SNe and the expanding photosphere method to obtain $H_0 = 65 \pm 15 \text{ km s}^{-1}\text{Mpc}^{-1}$. While most values of H_0 using SNe Ia were hovering between $50 - 60 \text{ km s}^{-1}\text{Mpc}^{-1}$ until the early 1990s (e.g., [Cadonau et al. 1985](#); [Tammann & Leibundgut 1990](#); [Branch & Miller 1993](#); [Sandage & Tammann 1993](#)), [Fukugita & Hogan \(1991\)](#) presented values of H_0 that ranged between $75 - 100 \text{ km s}^{-1}\text{Mpc}^{-1}$. As [Arnett et al. \(1985\)](#) provided theoretical reasoning for SNe Ia to be good standard candles, improvements in SNe Ia luminosity calibration would be the key to make precision measurements of H_0 , and other cosmological parameters.

[Rust \(1974\)](#) and [Pskovskii \(1977, 1984\)](#) suggested there existed a relationship between the peak luminosity in the B -band and light curve width for SNe Ia. [Phillips \(1993\)](#) pioneered the widely used “luminosity-width” relationship for the light curves of SNe Ia and showed that SN Ia luminosity can be precisely standardized within ± 0.15 mag using the luminosity-width relation with the later addition of a luminosity-color relation ([Tripp 1998](#))⁶. The relationship was further refined by the Calán-Tololo Supernova Project ([Hamuy et al. 1996](#)). With improved standardization of SN Ia luminosity, [Hamuy et al. \(1995\)](#) derived $H_0 \simeq 62 - 67 \text{ km s}^{-1}\text{Mpc}^{-1}$ and [Riess et al. \(1995\)](#) derived $H_0 = 67 \pm 7 \text{ km s}^{-1}\text{Mpc}^{-1}$. A few other studies, such as

² This law is expressed as $V = H_0 D$, where V is the recession velocity and D is the distance to external galaxies.

³ <https://web.cfa.harvard.edu/~dfabricant/huchra/hubble/>

⁴ Time-delay cosmography is also a geometrical distance indicator.

⁵ It was not clear from the paper that whether these 10 SNe were SNe Ia or a mix of various types.

⁶ Recently, [Boone et al. \(2021\)](#) published a spectrophotometry-based standardization method trained on 173 nearby SNe Ia that yielded an rms dispersion of ± 0.084 mag in a carefully blinded analysis.

the one in [Hoeftlich & Khokhlov \(1996\)](#), used theoretical models to predict SNe Ia luminosity, and derived $H_0 = 67 \pm 9 \text{ km s}^{-1} \text{ Mpc}^{-1}$.

SNe Ia thus became the most reliable tool to measure luminosity distances at higher redshifts, corresponding to look-back times of billions of years, where the observed velocity becomes cosmologically dominated (see [Leibundgut & Sullivan 2018](#); [Goobar & Leibundgut 2011](#) for general reviews on SN Ia cosmology). Thanks to their brightness and the use of rolling searches, numerous SNe Ia can be discovered in a short time. They can be used to measure the expansion rate far into the Universe, fairly accurately, when calibrated with Cepheids, TRGB, SBF, or any other appropriate distance calibrators (e.g., [Burns et al. 2018](#); [Riess et al. 2021](#); [Freedman 2021](#); [Khetan et al. 2021](#); [Garnavich et al. 2022](#)).

The Hubble Space Telescope (HST) Key Project initiated a campaign to achieve a 10% precision measurement of H_0 by observing Cepheid variables in the nearby universe ($\lesssim 20 \text{ Mpc}$; [Freedman et al. 2001](#)). When using these Cepheid variables to calibrate SNe Ia, they obtained $H_0 = 71 \pm 2 \text{ (stat)} \pm 6 \text{ (sys)} \text{ km s}^{-1} \text{ Mpc}^{-1}$. After the success of the HST Key Project, two major campaigns have been ongoing to determine H_0 using SNe Ia: Supernovae, H0 for the Equation of State of dark energy (SH0Es; [Riess et al. 2016](#)) and the Carnegie-Chicago Hubble Program (CCHP; [Freedman et al. 2019](#)).

While the SH0Es program has continued to rely primarily on Cepheid variables to calibrate the SN Ia distance scale and determine H_0 , the CCHP has been using TRGB as another independent distance anchor. Along with low halo reddening, another advantage of using TRGB *I*-band observations is that they are less sensitive to metallicity effects ([Freedman et al. 2019](#)). Moreover, it can be applied in the halos of galaxies, where crowding and blending effects are negligible. The CCHP has also extended TRGB data to the near-infrared *JHK* bands ([Madore et al. 2018](#)) to further improve SN Ia calibration. More recently, a third method of calibrating the SN Ia distance ladder has been put forward using SBF distances ([Blakeslee et al. 2021](#); [Khetan et al. 2021](#)). While the SBF distance scale is itself calibrated with Cepheids, it is nonetheless an independent path to calibrating the SNe Ia distances.

Alternatively, analysis of the Cosmic Microwave Background (CMB) can provide H_0 directly from the angular scale of the sound horizon ([Planck Collaboration et al. 2018](#)). This method requires extrapolating a cosmological model fit to the CMB over three orders of magnitude in redshift into a local value of H_0 . Similarly, H_0 can be derived using the Baryon Acoustic Oscillation (BAO) standard ruler in a distance ladder tied to the CMB

([Macaulay et al. 2019](#)). We summarize representative measurements of H_0 from various methods in Table 1.

It is clear from Table 1 that there are differences in H_0 obtained using various methods. In particular, H_0 inferred using methods tied to the CMB are significantly lower than those that are determined using local distance measurements. In addition, Cepheid-calibrated H_0 are also significantly higher than TRGB-calibrated H_0 . **Recently, Tully (2023) provided a historical review on H_0 .**

A number of solutions have been proposed to resolve the tension in H_0 . [Valentino et al. \(2021\)](#) presented a detailed review of possible solutions to the differences in H_0 that range from neutrino interactions to dynamical dark energy. [Bernal et al. \(2021\)](#) proposed a “new cosmic triangle” approach to break H_0 tension using the ages of older globular clusters. Alternatively, [Hamuy et al. \(2021\)](#) compared Cepheid and TRGB calibrations to various SN Ia samples and concluded that the mismatch in H_0 using these two calibrators is a consequence of the systematic difference in the distance moduli. Previously, [Dhawan et al. \(2020\)](#) showed that the value of H_0 does not change with various cosmological model selections. [Addison \(2021\)](#) found H_0 to be consistent with local calibrator methods using E-mode data of CMB. New datasets can bring new insights to H_0 , even with existing calibration methods.

The Carnegie Supernova Project (CSP; [Hamuy et al. 2006](#)) obtained high-quality light-curves of SNe Ia in *uBgVriYJH* bands from 2004 to 2015. Data from the CSP-I campaign, which ran from 2004 to 2009, played an important role in determining H_0 measurements for some of the above-mentioned studies (e.g., [Freedman et al. 2019](#), [Burns et al. 2018](#)). CSP-I SN Ia photometry was released in three papers: [Contreras et al. \(2010\)](#), [Stritzinger et al. \(2011\)](#), and [Krisciunas et al. \(2017\)](#); the latter included a re-calibration of the entire CSP-I dataset. Spectroscopic data is presented in [Folatelli et al. \(2013\)](#). In the CSP-I campaign, most of the SNe Ia observed were discovered in targeted galaxy searches, such as, Lick Observatory Supernova Search (LOSS; [Li et al. 2000](#)), and therefore are biased towards massive galaxies⁷.

A second follow-up campaign, the CSP-II, began in 2011 with the goal of extending the NIR SN Ia sample further out into the Hubble flow ($0.01 < z < 0.1$). The CSP-II ran for 4 years, observing SNe discovered by rolling searches, primarily the La Silla-Quest Low

⁷ See [Uddin et al. \(2017a\)](#) for a study on host galaxy bias in SN Ia cosmology.

Table 1. Recent H_0 measurements with statistical uncertainties. Systematic uncertainty in the Cepheid calibration has the least value of $1.04 \text{ km s}^{-1}\text{Mpc}^{-1}$, while for TRGB and SBF-based calibrations, they range between 1.6 and $3.4 \text{ km s}^{-1}\text{Mpc}^{-1}$.

Method	Calibration	H_0 ($\text{km s}^{-1}\text{Mpc}^{-1}$)	Reference
SN Ia	Cepheid	73.04 ± 1.01	Riess et al. (2022)
SN Ia	TRGB	69.80 ± 0.60	Freedman (2021)
SN Ia	Cepheid	72.70 ± 1.60	Burns et al. (2018)
SN Ia	SBF	70.50 ± 2.40	Khetan et al. (2021)
SN Ia	SBF	74.60 ± 0.90	Garnavich et al. (2022)
SBF	Cepheid	73.30 ± 0.07	Blakeslee et al. (2021)
SN Ia	BAO+CMB	67.80 ± 1.20	Macaulay et al. (2019)
CMB	-	67.40 ± 0.50	Planck Collaboration et al. (2018)

Redshift Survey (LSQ; Baltay et al. 2013). The project is summarized in Phillips et al. (2019) and Hsiao et al. (2019).

A total of 214 SNe Ia were observed in the redshift range $0.004 < z < 0.137$ during the CSP-II campaign. Of these, there are 125 “cosmology sample” SNe Ia in the smooth Hubble flow ($0.03 \lesssim z \lesssim 1.0$). Of the same 214 SNe, NIR spectra were obtained for 90 “physics sample” SNe Ia in the nearby universe ($z \lesssim 0.04$). Both optical and near-infrared ($uBgVriYJH$) light-curves were obtained out to higher redshifts to reduce the error due to peculiar velocities. This also enables one to compare SN Ia standard candles between optical and near-infrared wavelengths. In addition, 339 near-infrared spectra of 98 SNe were obtained in order to improve near-infrared K-corrections.

Combining the CSP-I and CSP-II samples has increased the total number of CSP SNe Ia by almost a factor of three compared to CSP-I alone. We will denote this combined sample as the CSP SN Ia sample for the rest of the paper. We will publish the CSP-II SN Ia photometry data and optical spectra in separate papers (Suntzeff et al. in preparation; Morrell et al., submitted). The near-infrared spectra have been published by Lu et al. (2022).

In this paper, we aim to determine H_0 by calibrating the full CSP SN Ia sample using a combination of two primary distance calibrators: Cepheids and TRGB, and a secondary distance indicator, SBF. Combining all calibrators may reveal the systematic uncertainties that originate due to the variation of the SN Ia distance scales among various calibrators, and may explain the H_0 tension from various methods. We also aim to determine H_0 in the $uBgVriYJH$ bands using various calibrators separately, and investigate intrinsic scatter of SNe Ia at these wavelengths. Finally, we revisit correlations between SN Ia Hubble residuals and host galaxy properties.

The outline of this paper is as follows: in §2 we describe sources of data; in §3 we perform analysis to calibrate SNe Ia and obtain values of H_0 ; in §4 we discuss the results; and finally we present our conclusions in §5.

2. DATA

2.1. Light-curve Fit

SNe Ia from the CSP-I and CSP-II samples are tabulated in Krisciunas et al. (2017) and Phillips et al. (2019), respectively. We present the number of SN Ia that we use in this work in each filter, along with the total number of calibrators, in Table 2. Selection of CSP-I SNe Ia is described by Uddin et al. (2020). From the CSP-II sample, we exclude iPTF13dym, and iPTF13dyt because of the peculiar behavior of their near-infrared light-curves. We also exclude PS1-13eao due to its high extinction. We did not use 03fg-like SNe Ia: ASASSN-15hy, SN 2007if, SN 2009dc, SN 2013ao, CSS140501-170414+174839 (Ashall et al. 2021; Lu et al. 2021; Hsiao et al. 2020), and also no Type Iax SNe Ia were included.

We fit SN Ia light-curves using SNooPy (Burns et al. 2011), using the `max_model` method, which provides peak magnitudes for each observed filter, the time of maximum, $(B - V)$ color⁸, and the color-stretch parameter s_{BV} (Burns et al. 2014) as well as all the covariances between the parameters. SNooPy computes K-corrections and S-corrections (when needed) using the optical Hsiao et al. (2007) and the new near-infrared SN Ia spectral energy templates from Lu et al. (2023) along with the CSP filter functions (Krisciunas et al. 2017; Phillips et al. 2019). From the peak magnitudes, we compute colors after applying Milky-Way reddening corrections using the dust maps of Schlafly & Finkbeiner (2011). SNooPy fitting is also done for SNe Ia from the literature that have distance measurements from

⁸ Throughout the paper our definition of $(B - V)$ color of SNe Ia corresponds to $(B_{max} - V_{max})$ color.

Table 2. Number of SNe Ia and calibrators available in each filter that are used in this work.

Band	Number				
	SNe Ia ^a	Cepheids ^b	TRGB ^c	SBF ^d	SBF ^e
<i>u</i>	216	17	11	12	11
<i>B</i>	322	25	18	24	22
<i>g</i>	235	11	5	4	5
<i>V</i>	323	25	18	24	22
<i>r</i>	323	24	16	19	19
<i>i</i>	322	24	16	19	19
<i>Y</i>	275	11	5	2	4
<i>J</i>	246	20	15	9	8
<i>H</i>	213	20	15	9	8

^a CSPI & II

^b Riess et al. (2021)

^c Freedman et al. (2019)

^d Khetan et al. (2021)

^e Jensen et al. (2021)

Cepheid, TRGB, and/or SBF methods. In all cases, we use the same version of SNOoPy using the same spectral templates. We show distributions of SN Ia color and color-stretch parameters in Figure 1. We also present them as a function of redshift to reveal the selection effects in Figure 2. The most notable difference is the larger number of slow-declining SNe Ia with bluer colors in the CSP-II sample compared to CSP-I.

2.2. Distance Calibrators

Cepheid and TRGB distances to SN Ia hosts are taken from Riess et al. (2022) and Freedman et al. (2019) respectively. Distances of two TRGB hosts are updated to Hoyt et al. (2021). They are the hosts of SN2007on and SN2011iv (NGC 1401) and SN2013aa and SN2017cbv (NGC 5643).

SBF distances to SNe Ia hosts come from two sources: one is a collection compiled in Khetan et al. (2021) from various sources, and the other consists of systematic measurements using the WFC3/IR camera on the HST published in Jensen et al. (2021). The Jensen et al. (2021) observations extend to greater distances than the Khetan et al. (2021) measurements — the average of the Jensen et al. (2021) distance moduli is 1.5 mag larger than the average of the Khetan et al. (2021) values.

While the multi-band light-curves of all 24 SBF-calibrated SNe Ia from Khetan et al. (2021) are available publicly, the same is true for only three out of the 22 from Jensen et al. (2021). These are the hosts of SN 2016arc (NGC 1272), SN 2007gi (NGC 4036), and SN 2018aaz (NGC 3158). There are seven ob-

jects that are common between Khetan et al. (2021) and Jensen et al. (2021). These are the hosts of SN 1970J (NGC 7619), SN 1995D (NGC 2962), SN 1997E (NGC 2258), SN 2003hv (NGC 1201), SN 2014bv (NGC 4386), SN 2015bp (NGC 5839), and SN 2000cx (NGC 0524). We compared the distance moduli of the common SBF hosts between Khetan et al. (2021) and Jensen et al. (2021) and found them to be comparable.

A detailed discussion on various calibration methods is beyond the scope of this paper, and we encourage readers to consult the references in the footnotes of Table 2 for details about various calibration processes. The distribution of calibrator host distances is shown in Figure 3. SBF calibrators extend to larger distances, while TRGB hosts are found to be relatively nearer than the other two. As we have noted earlier, that SBF distances are calibrated using Cepheid distances to a set of nearby early-type galaxies in the Virgo cluster, so they have an additional rung in the distance ladder.

2.3. Host Galaxy Stellar Mass

The host galaxy stellar masses of CSP SNe Ia have been derived using procedures described by Uddin et al. (2020). Briefly, we measure *uBgVriYJH* photometry using host galaxy follow-up images taken after the SNe Ia have faded, and build spectral energy distributions. We then use Z-PEG (Le Borgne & Rocca-Volmerange 2002) to determine the best-fit templates and derive stellar masses. Stellar masses of the hosts containing calibrating SNe Ia are taken from Burns et al. (2018) and Neill et al. (2009). Although host masses of galaxies from these two papers have offsets of 0.3 dex and 0.18 dex, respectively, with respect to those calculated by Uddin et al. (2020), our results have not changed (see §3.2). For consistency, the host masses of the calibrating SNe were adjusted for these offsets. Distributions of the host galaxy stellar masses of distant and calibrating SNe Ia are shown in Figure 4.

There are 19 SNe Ia from CSP-II for which no hosts are identified. This could be either the hosts are very faint or there are no hosts at all. We randomly assign stellar masses between $\text{Log}(M_*/M_\odot) = 7.1 - 7.9$ for the hosts of these apparently hostless SNe Ia. We also calculate stellar masses of 10 SBF hosts from Jensen et al. (2021) for which we do not have multi-band photometry. We use *K*-band photometry from the Two Micron all Sky Survey, and use an empirical formula described in Ma et al. (2014), to estimate their stellar mass.

It is evident that host stellar mass in the CSP-I sample is biased towards higher mass, since most SNe Ia followed were discovered in targeted surveys. Host mass in CSP-II sample is spread over a wider mass range,

since most of the observed SNe Ia were followed from untargeted surveys, such as, LSQ, Catalina Real Time Transit Survey (CRTS; Djorgovski et al. 2011), All-Sky Automated Survey for SuperNovae (ASAS-SN; Shappee et al. 2014), and a few other supernova surveys⁹.

We present the CSP sample used in this paper in Appendix §A. We also present Cepheid, TRGB, and SBF calibrators. Appendix §A lists peak magnitudes in the B -band. Similar data in all other bands are available online.¹⁰

3. ANALYSIS

3.1. SN Ia Luminosity Standardization

The luminosity-decline rate relation (Phillips 1993; Phillips et al. 1999) paved the way to standardize SN Ia luminosity to an accuracy of ~ 0.15 mag. This relation shows that luminous SNe Ia decline more slowly than less luminous events. However, this relation shows increasing scatter for faster-declining events. This is primarily due to the fact that the light-curve width parameter, $\Delta m_{15}(B)$ (defined as the change in magnitude in the B -band between peak and 15 days after peak) was not able to accurately measure the rate of evolution of the sub-luminous SNe (Phillips 2012). Burns et al. (2014) discuss issues related to $\Delta m_{15}(B)$ and introduced a color-stretch parameter s_{BV} , which better captures the diversity of the fastest-declining events by reducing scatter. In this analysis, we use s_{BV} to measure the decline rate of our SNe Ia.

Also, to deal with the effect of dust extinction and intrinsic color dependence, a correction is required. A simple approach is to apply a color correction as proposed by Tripp (1998), which we shall refer to as the Tripp method. Bluer SNe Ia are found to be more luminous, though this can be a combination of both the effects of dust, and intrinsic color variations, since the measured color is known to correlate with s_{BV} (see Figure 1, right panel). One could also use such correlations between observed color and s_{BV} to compute and apply a proper extinction correction, as was done by Burns et al. (2018). However, this introduces large correlated errors between the magnitudes in each filter. One of the goals of this analysis is to compare the dispersion and host mass correction in different bands. We thus wish to avoid such correlated errors as much as possible.

The final standardization correction that we apply is due to an empirical correlation between SN Ia luminos-

ity and host mass (see Uddin et al. 2020 and references therein). This is often applied as a mass step, where the sample is split in two at a particular mass threshold. This approach, while simple, has several problems. First, the choice of the mass threshold is somewhat arbitrary and due to the typically large uncertainties in stellar mass which are not normally distributed, assigning hosts to one side or the other of this threshold is itself an uncertain task and could introduce biases. Second, it is not obvious how to deal with the well-known bias in regression analysis introduced by large uncertainties in the independent variable (Kelly 2007), whereas there exists well-developed software for handling these errors in linear regression. We therefore opt to apply a linear correction for the host stellar mass with slope α .

We apply the above-mentioned corrections in the observed light-curves of SNe Ia. The observed distance moduli (μ_{obs}) of SNe Ia are defined by:

$$\mu_{obs} = m_x - P^N(s_{BV} - 1) - \beta(B - V) - \alpha(\mathcal{M}_* - \mathcal{M}_0) \quad (1)$$

Here, m_x is the peak magnitude in band x . $P^N(s_{BV} - 1)$ is a polynomial of order N . The coefficient of the zeroth term of this polynomial, P_0 , denotes the absolute magnitude, M_x of a SN Ia with zero $(B - V)$ color, color-stretch $s_{BV} = 1$, and host galaxy with stellar mass $\mathcal{M}_* = \mathcal{M}_0$. Here, $\mathcal{M}_* = \log_{10}(M_*/M_\odot)$ is the host stellar mass, and $\mathcal{M}_0 = \log_{10}(M_0/M_\odot)$ is a mass zero point, which we set at the median value of the host stellar mass in each band. **The choice of splitting the sample at the median mass ensures that equal weights are given above and below the median mass.** The parameter α is the slope of the luminosity-host mass correlation.

In this paper, we expand the polynomial up to second order ($N = 2$), and the coefficients are denoted as P_0 , P_1 , and P_2 . β is the slope of the luminosity-color relation. We define model distance moduli to SN Ia hosts in the Λ CDM cosmological framework as:

$$\mu_{\Lambda CDM} = 5 \log_{10} \left[\left(\frac{1 + z_{hel}}{1 + z_{cmb}} \right) \frac{cz_{cmb}}{H_0} \left(1 + \frac{1 - q_0}{2} z_{cmb} \right) \right] + 25 \quad (2)$$

Here q_0 is the deceleration parameter. The observed distance moduli (μ_{obs}) for all SNe Ia are calculated using Eqn. 1. In calculating model distance moduli (μ_{model}) we use Cepheid/TRGB/SBF-based distances when available, otherwise we use Eqn. 2 to predict distance. That is:

⁹ Phillips et al. (2019) describes all surveys from which CSP-II sample was generated.

¹⁰ <https://github.com/syeduddin/h0csp>

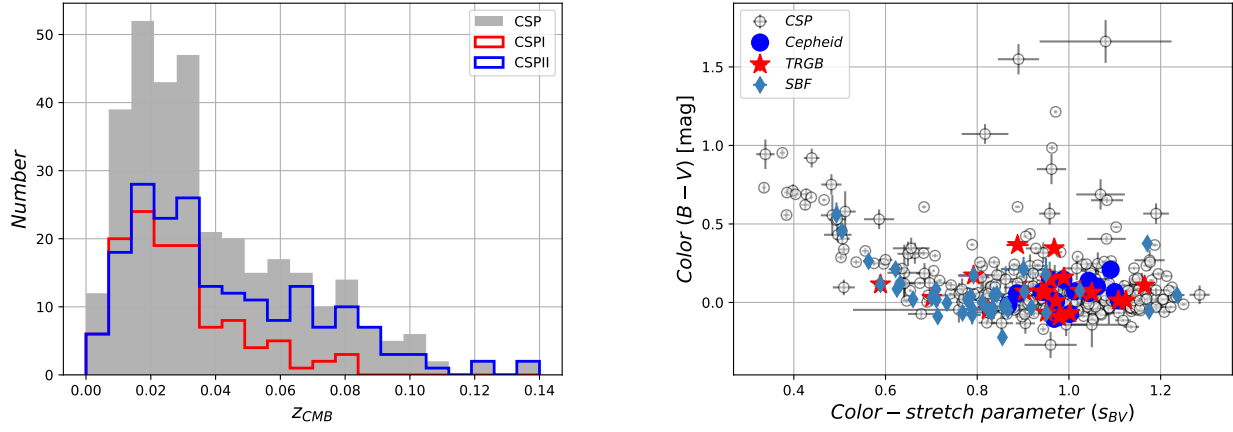


Figure 1. *Left:* Distribution of SN Ia redshifts in CSP-I and in CSP-II. *Right:* Distribution of SN Ia color and color-stretch parameters used in this study.

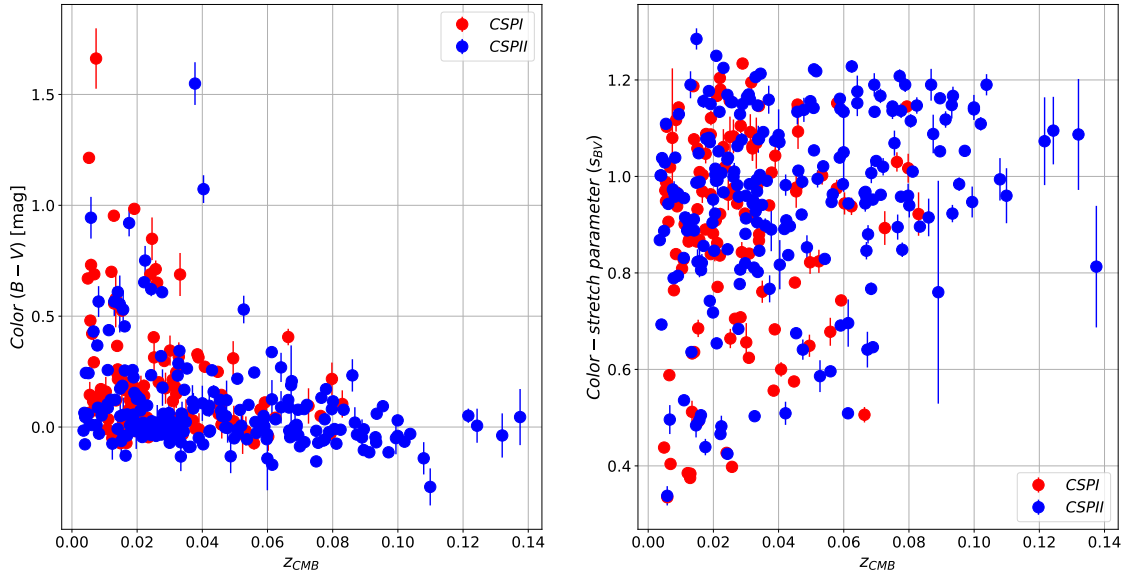


Figure 2. Distribution of SN Ia color (left) and the color-stretch parameter (right) as a function of redshift. Due to selection effects, we find bluer and slower-declining SNe Ia at higher redshift.

$$\mu_{model} = \begin{cases} \mu_{\Lambda\text{CDM}} & \text{SNe Ia} \\ \mu & \text{Cepheid/TRGB/SBF} \end{cases} \quad (3)$$

We compare the observationally-determined distance modulus with the model distance modulus by defining a χ^2 as:

$$\chi^2 = \sum_i \frac{(\mu_{obs,i} - \mu_{model,i})^2}{\sigma_i^2 + \sigma_{int}^2 + \sigma_{pec,i}^2} \quad (4)$$

Eqn. 4 has three error terms. The first error term, σ_i , is the sum of the individual errors on observed quantities along with the covariance between peak magnitude and color, and the covariance between peak magnitude and color-stretch parameter. Ignoring the index, the first error term can be expanded as:

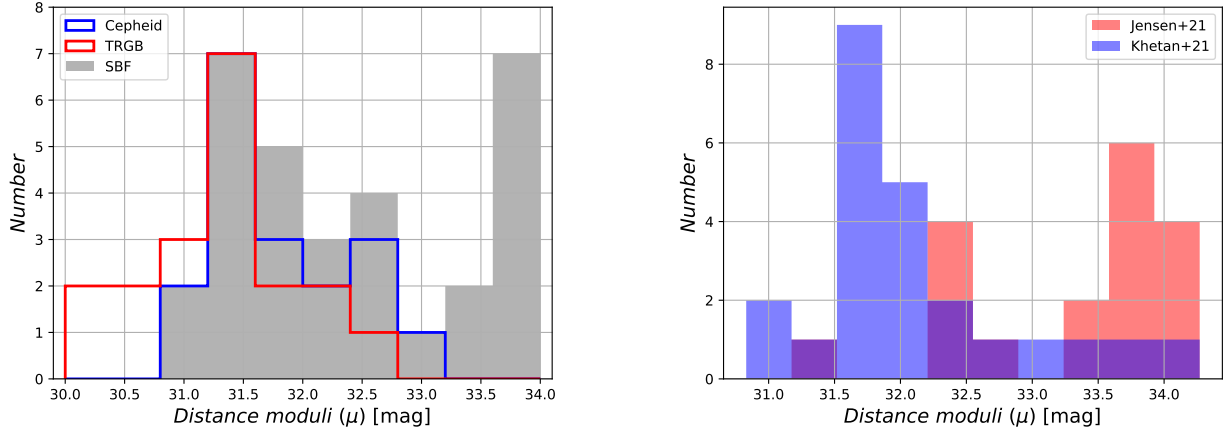


Figure 3. *Left:* Distribution of calibrator distance moduli. We note that SBF distances extend to higher values than TRGB and Cepheid distances. *Right:* Comparison of two SBF calibration samples. Note that SBF hosts from [Jensen et al. \(2021\)](#) are peaked at higher distances.

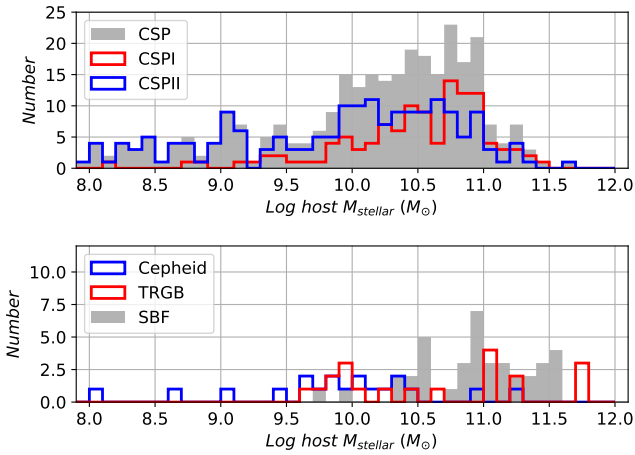


Figure 4. Distribution of host galaxy stellar mass for the CSP sample (top) and the calibrating SNe Ia (bottom). See text for discussion.

$$\begin{aligned}
 \sigma^2 = & \sigma_{m_x}^2 + (P1 + 2P2 (s_{BV} - 1))^2 \sigma_{s_{BV}}^2 \\
 & + \beta^2 \sigma_{B-V}^2 - 2(P1 + 2P2 (s_{BV} - 1)) \text{cov}(m_x, s_{BV}) \\
 & + 2\beta(P1 + 2P2 (s_{BV} - 1)) \text{cov}(s_{BV}, B - V) \\
 & - 2\beta \text{cov}(m_x, B - V) + \alpha^2 \sigma_M^2
 \end{aligned} \tag{5}$$

The second error term, σ_{int} , is the intrinsic random scatter that we add to the error budget as a free parameter to account for SN-to-SN variations not accounted for by σ_i or σ_{pec} . The final error term σ_{pec} is the error due to uncertainty in distance measurements resulting from galaxy peculiar velocities that scales with redshift.

This term can be expressed as¹¹:

$$\sigma_{pec} = 2.17 \frac{V_{pec}}{cz_{cmb}} \tag{6}$$

where V_{pec} is a free parameter that represents the average peculiar velocity of SN Ia sample. V_{pec} is **allowed to vary in each filter because the sample size and redshift distribution are different in each filter.**¹² Note that σ_{int} and σ_{pec} are calculated for SNe Ia that do not have distance measurements from calibrators. For calibrators, uncertainties from their distances are included.

To find the best values and uncertainties of all variables, we explore the parameter space with Markov Chain Monte Carlo (MCMC) techniques after converting the χ^2 into a log-likelihood function

$$\mathcal{L} = -0.5[\chi^2 + N \log(2\pi\sigma^2)] \tag{7}$$

where σ includes all error terms mentioned in Eqn. 4, and N is the total number of data points.

We use a Python package, EMCEE ([Foreman-Mackey et al. 2013](#)) to explore the likelihood of each variable. EMCEE utilizes an affine invariant MCMC ensemble sampler proposed by [Goodman & Weare \(2010\)](#). The

¹¹ One can obtain this term by taking the partial derivatives of the first order term of the distance equation,

$$\mu(z) = 5 \log_{10} \left(\frac{cz}{H_0} \right)$$

¹² Recently, [Peterson et al. \(2022\)](#) demonstrated that by separating the component of redshift due to peculiar velocity, the value of H_0 can change by $\sim 0.4 \text{ km s}^{-1} \text{ Mpc}^{-1}$. We discuss this further in § 3.2.2.

advantage of this sampler over traditional Metropolis-Hastings sampling is that it significantly reduces auto-correlation time. Another advantage of an affine invariant sampler is that we need to tune only two parameters to get the desired output: number of walkers and number of steps.

Briefly, we start by assigning initial maximum likelihood values of variables to the walkers. The walkers then start wandering and explore the full posterior distribution. After an initial run, we inspect the samplers for their performance. A good way to do this is to look at the time series of variables in the chain and compute the autocorrelation time, τ . We then set the number of steps to greater than 50τ as suggested by the online documentation¹³. When the chains are sufficiently burnt-in (e.g., they forget their initial start point), we can safely throw away some steps that are a few times higher than the burnt-in steps. Another criterion of good sampling is the acceptance fraction, a_f . This is the fraction of steps that are accepted after the sampling is done. The suggested value of a_f is between 0.2–0.5 (Gelman et al. 1996).

We run EMCEE with 80 walkers. We sample 3000 steps and throw away the first 500. In each run, we obtain $a_f \sim 0.46$. One can visualize the output of two-dimensional and one-dimensional posterior probability distributions in a corner plot, and check for any unwanted multi-modal distribution. From the marginalized distributions we take the 16th, 50th, and 84th percentiles to obtain best-fit values and uncertainties.

Previously, Burns et al. (2018) employed the ‘No U-Turn Sampler’ using the STAN data modeling language. We can therefore check the consistency between the two sampling methods. We set $H_0 = 72 \text{ km s}^{-1} \text{ Mpc}^{-1}$ and the deceleration parameter $q_0 = \Omega_m/2 - \Omega_\Lambda = -0.53$ as priors as used in Burns et al. (2018). We compare the luminosity calibration between this work and Burns et al. (2018) using the Tripp method in the B -band. This comparison is shown in Table 3 for the Cepheid calibration. Tripp nuisance variables for both CSP-I and the combined CSP-I & II samples are shown. We confirm that for the CSP-I sample, results from both EMCEE (this work) and STAN (Burns et al. 2018) agree.

We note that both σ_{int} and V_{pec} have increased for the combined sample in comparison to CSP-I. This is due to the addition of more low-redshift SNe Ia in the combined sample. For example, for $z < 0.01$, there are 14 SNe Ia in CSP-I, and 13 SNe Ia in CSP-II. Therefore, in the combined sample, there is almost a two-fold increase of

low-redshift SNe Ia. To prove the effect of low-redshift SNe Ia on V_{pec} , we calculate V_{pec} by removing $z < 0.01$ SNe Ia. With this restricted sample V_{pec} is 243 km s^{-1} in CSP-I, and 251 km s^{-1} in the combined sample. The values of σ_{int} in these cases are 0.14 mag and 0.18 mag, respectively. **The β parameter is also steeper in the combined sample than CSP-I sample. This could be due to the fact that in the combined sample, we have more star-forming galaxies that produce more dust.**

3.2. Measurement of H_0

3.2.1. Using Calibrators Separately

The principal objective of this paper is to determine H_0 using various distance calibrators: Cepheids, TRGB, and SBF. In this section, we calculate H_0 using various calibrators separately. In the next section (§ 3.2.2), we combine all calibrators to obtain global values of H_0 . We follow the procedure described in § 3.1, but now include H_0 as a variable. We note that we solve for H_0 and all other nuisance parameters simultaneously so that all errors and co-variances propagate to the final uncertainty in H_0 .

We present H_0 and other nuisance variables using different calibration methods across $uBgVriYJH$ bands in Table 4. Figure 5 represents a corner plot of posterior probability distributions of variables from EMCEE output using the Cepheid calibration. Using the B -band light-curve fit, we get $H_0 = 72.24 \pm 0.74 \text{ km s}^{-1} \text{ Mpc}^{-1}$ from the Cepheid calibration and $H_0 = 70.31 \pm 0.70 \text{ km s}^{-1} \text{ Mpc}^{-1}$ from the TRGB calibration. When we use the SBF calibration, we obtain different values depending on the compilation used. We obtain $H_0 = 69.52 \pm 0.93 \text{ km s}^{-1} \text{ Mpc}^{-1}$ using the SBF compilation from Khetan et al. (2021) and $H_0 = 77.11 \pm 1.11 \text{ km s}^{-1} \text{ Mpc}^{-1}$ using the compilation from Jensen et al. (2021). If we combine these two compilations, we obtain $H_0 = 72.62 \pm 0.90 \text{ km s}^{-1} \text{ Mpc}^{-1}$. Throughout this paper, we present statistical errors unless otherwise stated. We define statistical errors as the 1- σ confidence interval of the marginalized parameter in question. For H_0 , this includes the uncertainty in all nuisance parameters in Eqn. 1. We discuss systematic errors due to the variation in the SN Ia distance scales among various calibrators and due to SN Ia sample selection effects in § 4.1 and in § 4.3, respectively.

When we compare H_0 using Cepheid and TRGB calibrations, we find them to be consistent with previously published studies (See Table 1). When we compare H_0 using the SBF calibration from Khetan et al. (2021), we also obtain a consistent result. Similarly, we obtain consistent H_0 using the SBF calibrators from Jensen

¹³ <https://emcee.readthedocs.io/en/stable/tutorials/autocorr/>

Table 3. Comparing the Cepheid calibration of CSP SNe Ia using the Tripp method. We include 1σ statistical uncertainties in the parentheses.

Parameter	Burns et al. (2018) (CSP-I)	This Work (CSP-I)	This Work (CSP-I & II)
$P0$ (mag)	-19.18 (06)	-19.18 (02)	-19.09 (01)
$P1$ (mag)	-0.89 (11)	-0.87 (12)	-1.22 (08)
$P2$ (mag)	-0.02 (30)	-0.07 (30)	-1.45 (30)
β	2.65 (08)	2.76 (10)	3.06 (08)
α (mag/dex)	-0.06 (03)	-0.08 (04)	-0.02 (01)
σ_{int} (mag)	0.13	0.13	0.17
V_{pec} (km s $^{-1}$)	310	297	442

et al. (2021), with a recent study by Garnavich et al. (2022), who also used SBF calibrators from Jensen et al. (2021). However, these SBF-calibrated H_0 values differ depending on which SBF sample is used: Khetan et al. (2021) or Jensen et al. (2021). The difference is significant ($> 5\sigma$) when we consider statistical error only, but reduced to $< 2\sigma$, when we consider systematic errors of ~ 3.0 km s $^{-1}$ Mpc $^{-1}$.

It is currently not clear why we are observing significant differences in H_0 from the two SBF compilations. As noted earlier, the average distance moduli of 22 SBF hosts that we use in this work from Jensen et al. (2021) is 1.5 mag fainter than that of 24 SBF hosts from Khetan et al. (2021). In the rest of this study (from Table 5 onward), we concatenate SBF distances from Jensen et al. (2021) and Khetan et al. (2021), and use the combined sample as the SBF sample¹⁴.

We also note from Table 4 that SN Ia absolute magnitudes ($P0$ values) are different among the calibration methods. H_0 decreases with increasing SN Ia luminosity, which is a direct consequence of Eqn. 2. These two terms are also dependent on each other (See Figure 5). In the absence of any distance calibration, they are fully degenerate. It is the systematic differences in the calibrator distances that drive differences in H_0 . We compare various calibrators in §4.1.

Next, we investigate how H_0 varies when SNe Ia are observed across various photometric bandpasses. In the Cepheid calibration, H_0 is consistent among $BVri$ bands, but gives larger values in $ugYJH$ bands¹⁵. In the TRGB calibration, H_0 is different ($\sim 2\sigma$) between optical ($uBgVri$) and near-infrared (YJH) bands. Pre-

viously, Freedman et al. (2019) found smaller value of H_0 in the H band compare to the B band, using the CSP-I SN Ia sample. We also obtain similar result when we use the CSP-I sample. It is the addition of SNe Ia from CSP-II that changes the trend in H_0 (see Figure 7). In the combined SBF calibration, we find smaller H_0 in the J and H bands compared to rest of the bands.

A conspicuous trend in the TRGB-calibrated values of H_0 can be seen in Figure 7. While the combined CSP-I and II sample always yields a value for H_0 between the CSP-I and CSP-II subsamples (as one would expect), CSP-I tends to give a higher value of H_0 than CSP-II in the optical, but the opposite is true in the NIR. This raises the concern that there is a systematic error in the NIR photometry that has been introduced when switching our NIR camera (RetroCam) from the Swope telescope to the du Pont. Yet there does not appear to be any such systematic in the photometry of the local sequence photometry (see Suntzeff et al., in preparation). Examining the distribution of residuals reveals that they are significantly non-Gaussian in the NIR, with a bright “tail” (see Figure 8). This tail is seen in both the CSP-I and CSP-II subsamples, indicating it is not likely that a systematic offset is responsible for the different values of H_0 . Fitting with a two-component Gaussian indicates that nearly 20% of the combined CSP-I and CSP-II sample originate from this brighter tail in the NIR, yet no such tail is seen in the optical. These overly bright residuals do not correlate with any of the corrections we apply (s_{BV} , $B - V$ color, host mass, or red-shift). Interestingly, the mode of the residuals in the optical appear to line up with the mode of residuals in the NIR for the same H_0 , as shown in Figure 8. This could indicate the existence of an overly-NIR-bright subpopulation of SNe Ia and warrants further investigation.

¹⁴ For the seven hosts that are common between Jensen et al. (2021) and Khetan et al. (2021), we use distances from Jensen et al. (2021), since Jensen et al. (2021) provide the most recent measurements of them.

¹⁵ We note that Galbany et al. (2022) used publicly available CSP-I data to calculate H_0 utilizing Cepheid calibration in YJH bands. Their results are consistent with ours within systematic uncertainties.

We also calculate H_0 and other variables by excluding 91T and 91bg-like SNe Ia¹⁶. We show our results in Table 5. Although they are *bona fide* SNe Ia, they have peculiar spectra, and may have separate progenitor channels. Moreover, 91T-like SNe Ia (Filippenko et al. 1992a; Phillips et al. 1992; Ruiz-Lapuente et al. 1992) are relatively over-luminous (Boone et al. 2021; Phillips et al. 2022; Yang et al. 2022), and 91bg-like events are sub-luminous (Filippenko et al. 1992b; Leibundgut et al. 1993). In both Tables 4 and 5, we see slightly larger values of H_0 when the TRGB calibration is used in near-infrared (YJH) bands. This scenario is reversed in the SBF calibration. H_0 in the Cepheid calibration remains consistent across the bands.

The use of nine $uBgVriYJH$ bands from optical to near-infrared provides us an opportunity to measure inter-band scatter in the values of H_0 , which can be considered as an additional systematic uncertainty. We show inter-band scatter in Table 14 and find that the inter-band scatter is $\sim 0.03 \text{ km s}^{-1} \text{ Mpc}^{-1}$, which is much smaller than the statistical error in H_0 .

Finally, in measuring H_0 , we have used host stellar mass as an additional correction factor in the SN Ia luminosity calibration. If we do not use this correction, H_0 does not change significantly. We show this in Table 6.

3.2.2. Combining All Calibrators

In this section, we combine all calibrators from Cepheid, TRGB, and SBF to derive H_0 . We utilize B and H band data to represent optical and near-infrared results, respectively. Combining all calibrators also allows us to determine systematic error that may originate from the variation in distance scales among different calibrators (see § 4.1). We follow the same procedure as in § 3.2.1 and present H_0 in Table 7.

It has been common in SN Ia cosmology analyses since Joint Light Curve Analysis (JLA; Beuoule et al. 2014) to correct SN Ia redshifts using estimates of peculiar velocities to account for local, large scale structures, with estimates most commonly derived from the 2M++ survey (Carrick et al. 2015). These have been shown to improve the overall fit (χ^2 and dispersion) in large SN Ia samples (Peterson et al. 2023). Here, starting with the combined analysis, we include these velocity corrections calculated from Carrick et al. (2015). The mean sample velocity correction for the CSP survey is 90 km sec^{-1} and the standard deviation of the

corrections is 320 km sec^{-1} . At the sample mean, $cz = 10,800 \text{ km sec}^{-1}$, this is equivalent to a mean correction of $5\log((cz + 90)/cz) = 0.017 \text{ mag}$ and a standard deviation of the corrections of 0.064 mag . To assess the significance of these corrections to the Hubble diagram, we can compare the SN σ_{int} with the corrections to σ_{int} with randomized application of corrections drawn from a gaussian of the same width as the corrections. For the B -band analysis, which is the largest sample, the improvement would occur by chance 1% of the time, i.e., $\sim 99\%$ confidence in the usefulness of the corrections. For the smaller H -band analysis, it is 90% confidence. The impact to H_0 is to increase it by $0.55 \text{ km s}^{-1} \text{ Mpc}^{-1}$ for B and $0.6 \text{ km s}^{-1} \text{ Mpc}^{-1}$ for H .

From the B and H bands we obtain $H_0 = 71.76 \pm 0.58 \text{ km s}^{-1} \text{ Mpc}^{-1}$ and $H_0 = 73.22 \pm 0.68 \text{ km s}^{-1} \text{ Mpc}^{-1}$. We consider these two values of H_0 as agnostic values of H_0 from this work, since we do not prefer one calibration method over others. We discuss and calculate systematic uncertainties among various distance scales by performing an analysis in §4.1.

4. DISCUSSION

4.1. Systematic Difference among Various Calibrators

We see in Table 4 that H_0 and $P0$ are different when they are obtained using different calibration methods. In this context, we can address the question of how absolute magnitudes of SNe Ia would vary between the calibrating SNe Ia samples. To answer this, we perform a MCMC analysis where we use all three calibrations simultaneously, and assign a separate absolute magnitude for each case (e.g. $P0_{Cepheid}$, $P0_{TRGB}$, and $P0_{SBF}$). The absolute magnitude of a distant SN Ia is $P0_{dist}$. In performing the MCMC sampling, we draw $P0s$ of calibrating SNe Ia from a normal distribution that has a mean of $P0_{dist}$ and a standard deviation, σ_{cal} that we add as an additional fitting parameter. The advantage of fitting simultaneously, rather than fitting each calibrator separately, is that all other nuisance parameters are solved consistently, and their uncertainties are propagated correctly. We show this analysis in Table 8.

The complete uncertainty in H_0 is given as the error in the posterior and including marginalization over σ_{cal} . We use the error in $P0_{dist}$ to calculate the systematic error in H_0 . To do this, we first remove the statistical error in $P0$ (Table 7) from the total error in $P0_{dist}$ (Table 8) to get the systematic error. Since $\mu \sim 5 \times \log_{10}(cz/H_0)$, $\sigma_{H_0}/H_0 \sim \sigma_{P0}/2.17$. Therefore, σ_{H_0} corresponds to $1.19 \text{ km s}^{-1} \text{ Mpc}^{-1}$ in B -band, and

¹⁶ We note that not all SNe Ia have spectroscopic information at the right phase for sub-typing.

Table 4. H_0 and all other nuisance parameters for the full sample in various bands. The number of calibrators used in each band is mentioned in Table 2. For H_0 , if the uncertainty is greater than one $\text{km s}^{-1} \text{Mpc}^{-1}$, we explicitly include decimals in quoting uncertainties. For all other cases, they should be read as the first two digits after decimals. We keep this convention throughout the paper.

Calibration	Band	H_0 ($\text{km s}^{-1} \text{Mpc}^{-1}$)	σ_{int} (mag)	V_{pec} (km s^{-1})	$P0$ (mag)	$P1$ (mag)	$P2$ (mag)	α (mag/dex)	β
Cepheid	<i>u</i>	73.61 (1.07)	0.23 (02)	479 (62)	-18.721 (021)	-1.89 (14)	-1.89 (48)	-0.06 (01)	4.30 (13)
	<i>B</i>	72.24 (0.74)	0.18 (01)	440 (48)	-19.119 (015)	-1.25 (09)	-1.23 (30)	-0.02 (01)	3.03 (08)
	<i>g</i>	72.93 (0.94)	0.15 (01)	471 (46)	-19.156 (023)	-1.21 (11)	-1.18 (33)	-0.03 (01)	2.59 (09)
	<i>V</i>	72.39 (0.66)	0.19 (01)	463 (48)	-19.116 (014)	-1.28 (09)	-1.40 (31)	-0.02 (01)	2.08 (07)
	<i>r</i>	71.37 (0.65)	0.17 (01)	442 (44)	-19.070 (015)	-1.14 (08)	-0.83 (28)	-0.03 (00)	1.57 (06)
	<i>i</i>	72.41 (0.63)	0.15 (01)	422 (41)	-18.462 (014)	-0.74 (08)	-0.54 (25)	-0.03 (00)	1.11 (06)
	<i>Y</i>	72.48 (0.80)	0.12 (01)	360 (37)	-18.476 (021)	-0.40 (07)	0.66 (23)	-0.03 (00)	0.49 (06)
	<i>J</i>	74.75 (0.81)	0.17 (01)	370 (47)	-18.616 (017)	-0.68 (1)	0.12 (30)	-0.03 (01)	0.51 (08)
	<i>H</i>	73.78 (0.71)	0.14 (01)	369 (45)	-18.386 (015)	-0.41 (09)	0.45 (30)	-0.03 (01)	0.23 (08)
TRGB	<i>u</i>	69.67 (1.06)	0.23 (02)	446 (62)	-18.844 (025)	-1.47 (14)	-0.20 (40)	-0.07 (02)	3.87 (10)
	<i>B</i>	70.31 (0.70)	0.18 (01)	431 (49)	-19.179 (015)	-1.08 (09)	-0.53 (28)	-0.00 (01)	2.87 (06)
	<i>g</i>	71.00 (1.15)	0.15 (01)	464 (49)	-19.216 (032)	-1.08 (11)	-0.64 (33)	-0.01 (01)	2.50 (09)
	<i>V</i>	70.15 (0.64)	0.18 (01)	452 (48)	-19.186 (014)	-1.08 (09)	-0.59 (27)	-0.01 (01)	1.91 (06)
	<i>r</i>	69.26 (0.64)	0.17 (01)	441 (44)	-19.137 (015)	-0.96 (08)	-0.11 (25)	-0.01 (00)	1.43 (05)
	<i>i</i>	69.76 (0.62)	0.15 (01)	429 (44)	-18.540 (014)	-0.56 (07)	0.04 (22)	-0.01 (00)	0.97 (05)
	<i>Y</i>	71.65 (0.99)	0.12 (01)	348 (38)	-18.502 (028)	-0.33 (07)	0.80 (24)	-0.03 (00)	0.50 (06)
	<i>J</i>	72.92 (0.81)	0.18 (01)	332 (47)	-18.674 (016)	-0.55 (10)	0.77 (29)	-0.04 (01)	0.30 (06)
	<i>H</i>	71.45 (0.74)	0.15 (01)	340 (42)	-18.467 (016)	-0.29 (09)	0.85 (26)	-0.05 (01)	0.19 (06)
SBF ^a	<i>u</i>	66.24 (1.50)	0.22 (01)	466 (54)	-18.949 (045)	-1.39 (17)	-0.27 (49)	-0.02 (02)	4.01 (14)
	<i>B</i>	69.52 (0.93)	0.18 (01)	441 (40)	-19.214 (026)	-0.90 (09)	-0.06 (29)	-0.01 (01)	2.85 (08)
	<i>g</i>	68.86 (1.75)	0.14 (01)	464 (48)	-19.269 (052)	-0.92 (12)	-0.56 (34)	0.00 (01)	2.51 (09)
	<i>V</i>	69.63 (0.91)	0.18 (01)	453 (42)	-19.211 (024)	-0.90 (09)	-0.22 (29)	-0.01 (01)	1.91 (08)
	<i>r</i>	69.40 (0.91)	0.17 (01)	408 (39)	-19.139 (025)	-0.90 (08)	-0.10 (26)	-0.01 (01)	1.49 (07)
	<i>i</i>	70.03 (0.89)	0.15 (01)	394 (37)	-18.538 (025)	-0.59 (07)	-0.06 (23)	-0.02 (01)	1.04 (06)
	<i>Y</i>	64.11 (1.66)	0.12 (01)	346 (35)	-18.745 (056)	-0.34 (08)	0.85 (25)	-0.02 (01)	0.48 (06)
	<i>J</i>	67.54 (1.17)	0.17 (01)	372 (39)	-18.838 (033)	-0.61 (11)	0.41 (32)	-0.03 (01)	0.41 (09)
	<i>H</i>	64.99 (1.02)	0.14 (01)	386 (39)	-18.665 (03)	-0.37 (10)	0.63 (30)	-0.03 (01)	0.21 (08)
SBF ^b	<i>u</i>	73.04 (1.64)	0.22 (02)	480 (62)	-18.724 (047)	-1.34 (16)	-0.24 (48)	-0.01 (02)	3.93 (14)
	<i>B</i>	77.11 (1.11)	0.17 (01)	462 (49)	-18.963 (028)	-0.84 (08)	-0.68 (29)	0.02 (01)	2.95 (08)
	<i>g</i>	76.71 (1.76)	0.14 (01)	487 (47)	-19.035 (049)	-0.95 (12)	-0.68 (35)	-0.00 (01)	2.50 (09)
	<i>V</i>	77.56 (1.08)	0.18 (01)	484 (48)	-18.949 (028)	-0.85 (09)	-0.84 (28)	0.02 (01)	1.99 (08)
	<i>r</i>	76.37 (0.98)	0.16 (01)	461 (45)	-18.913 (025)	-0.81 (08)	-0.38 (26)	0.01 (01)	1.53 (07)
	<i>i</i>	76.70 (1.01)	0.14 (01)	446 (43)	-18.327 (026)	-0.58 (07)	-0.40 (25)	-0.00 (01)	1.07 (06)
	<i>Y</i>	73.90 (1.64)	0.12 (01)	367 (37)	-18.428 (048)	-0.36 (08)	0.64 (24)	-0.02 (01)	0.48 (06)
	<i>J</i>	75.46 (1.47)	0.17 (01)	374 (46)	-18.594 (04)	-0.61 (10)	0.24 (30)	-0.02 (01)	0.48 (08)
	<i>H</i>	76.08 (1.39)	0.14 (01)	375 (46)	-18.315 (038)	-0.33 (10)	0.50 (30)	-0.01 (01)	0.26 (07)
SBF (combined)	<i>u</i>	69.81 (1.44)	0.22 (02)	474 (62)	-18.843 (04)	-1.36 (16)	-0.14 (46)	-0.02 (02)	4.04 (14)
	<i>B</i>	72.62 (0.90)	0.18 (01)	449 (49)	-19.115 (022)	-0.87 (08)	-0.04 (28)	-0.00 (01)	2.84 (08)
	<i>g</i>	73.32 (1.39)	0.14 (01)	481 (51)	-19.138 (039)	-0.94 (12)	-0.62 (36)	-0.00 (01)	2.52 (09)
	<i>V</i>	72.87 (0.85)	0.18 (01)	470 (50)	-19.112 (02)	-0.84 (08)	-0.12 (28)	-0.01 (01)	1.90 (07)
	<i>r</i>	72.12 (0.83)	0.17 (01)	447 (45)	-19.056 (02)	-0.85 (08)	0.04 (26)	-0.01 (01)	1.46 (07)
	<i>i</i>	72.65 (0.81)	0.15 (01)	433 (45)	-18.460 (02)	-0.59 (07)	-0.01 (22)	-0.02 (00)	1.04 (06)
	<i>Y</i>	70.12 (1.32)	0.12 (01)	363 (37)	-18.547 (040)	-0.35 (08)	0.70 (24)	-0.03 (00)	0.50 (06)
	<i>J</i>	70.69 (1.11)	0.17 (01)	362 (47)	-18.747 (029)	-0.63 (11)	0.47 (31)	-0.03 (01)	0.44 (08)
	<i>H</i>	68.58 (0.99)	0.14 (01)	361 (46)	-18.560 (026)	-0.41 (10)	0.88 (29)	-0.03 (01)	0.20 (07)

^a Khetan et al. 2021

^b Jensen et al. 2021

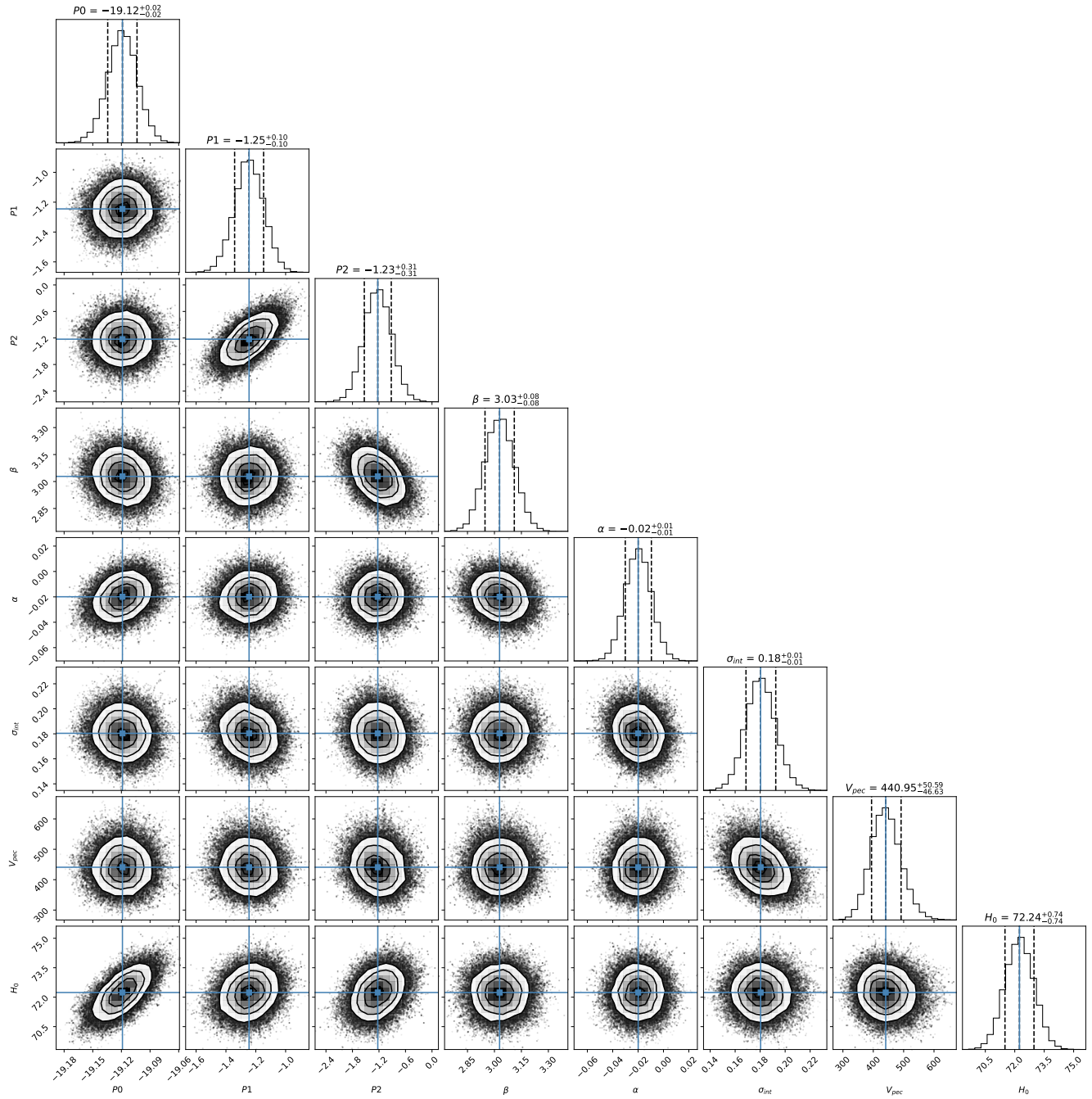
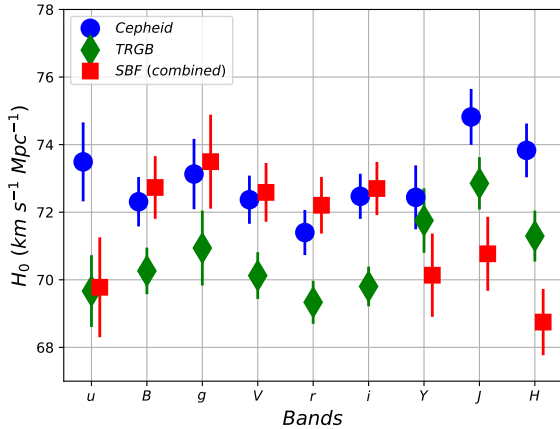
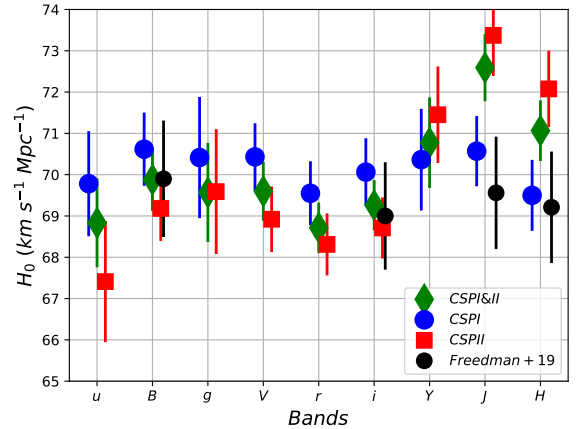


Figure 5. Posterior distribution of MCMC fitting parameters in determining H_0 using the B -band peak magnitude based on a Cepheid calibration. See Table 3 for the units of parameters.

Table 5. H_0 and all other nuisance parameters. Here, we exclude 91T and 91bg-like SNe Ia.

Calibration	Band	H_0	σ_{int}	V_{pec}	$P0$	$P1$	$P2$	α	β
		($\text{km s}^{-1} \text{Mpc}^{-1}$)	(mag)	(km s^{-1})	(mag)	(mag)	(mag)	(mag/dex)	
Cepheid	<i>u</i>	72.59 (1.10)	0.19 (02)	501 (66)	-18.717 (024)	-1.88 (15)	-2.85 (57)	-0.07 (01)	4.33 (14)
	<i>B</i>	71.67 (0.68)	0.15 (01)	456 (48)	-19.117 (016)	-1.22 (10)	-1.39 (37)	-0.03 (01)	3.01 (08)
	<i>g</i>	72.61 (0.89)	0.12 (01)	473 (51)	-19.151 (024)	-1.27 (12)	-1.70 (43)	-0.03 (01)	2.55 (09)
	<i>V</i>	71.67 (0.69)	0.15 (01)	471 (52)	-19.114 (015)	-1.26 (09)	-1.71 (33)	-0.03 (01)	2.06 (08)
	<i>r</i>	70.75 (0.63)	0.14 (01)	451 (46)	-19.070 (015)	-1.10 (09)	-0.93 (32)	-0.03 (00)	1.53 (06)
	<i>i</i>	71.88 (0.60)	0.12 (01)	442 (41)	-18.462 (015)	-0.59 (08)	-0.35 (30)	-0.03 (00)	1.11 (06)
	<i>Y</i>	71.99 (0.77)	0.10 (01)	370 (38)	-18.475 (022)	-0.23 (08)	0.83 (27)	-0.03 (00)	0.51 (06)
	<i>J</i>	73.80 (0.72)	0.14 (01)	365 (44)	-18.614 (016)	-0.47 (10)	0.10 (38)	-0.03 (01)	0.52 (07)
<i>H</i>	73.57 (0.70)	0.11 (01)	387 (44)	-18.378 (016)	-0.22 (11)	0.51 (41)	-0.03 (01)	0.23 (07)	
TRGB	<i>u</i>	69.26 (1.08)	0.21 (02)	453 (65)	-18.839 (025)	-1.47 (18)	-0.48 (57)	-0.09 (02)	3.87 (11)
	<i>B</i>	69.87 (0.69)	0.16 (01)	436 (49)	-19.171 (016)	-1.09 (10)	-0.68 (30)	-0.01 (01)	2.86 (07)
	<i>g</i>	70.73 (1.16)	0.13 (01)	462 (51)	-19.216 (033)	-1.14 (12)	-0.77 (43)	-0.02 (01)	2.45 (09)
	<i>V</i>	69.91 (0.66)	0.16 (01)	458 (50)	-19.167 (016)	-1.21 (09)	-1.15 (26)	-0.01 (01)	1.86 (06)
	<i>r</i>	68.93 (0.63)	0.15 (01)	449 (47)	-19.136 (015)	-0.91 (09)	0.01 (33)	-0.01 (01)	1.43 (05)
	<i>i</i>	69.41 (0.61)	0.12 (01)	443 (45)	-18.534 (015)	-0.44 (07)	0.25 (23)	-0.01 (00)	0.99 (05)
	<i>Y</i>	71.48 (1.02)	0.10 (01)	360 (37)	-18.494 (029)	-0.16 (07)	0.99 (24)	-0.03 (00)	0.53 (06)
	<i>J</i>	72.29 (0.74)	0.14 (01)	335 (42)	-18.665 (017)	-0.34 (10)	0.92 (34)	-0.04 (01)	0.33 (06)
<i>H</i>	71.08 (0.74)	0.12 (01)	363 (44)	-18.463 (016)	-0.05 (10)	1.18 (29)	-0.04 (01)	0.16 (06)	
SBF (combined)	<i>u</i>	69.75 (1.51)	0.21 (02)	477 (61)	-18.825 (046)	-1.22 (21)	0.04 (59)	-0.03 (02)	4.06 (14)
	<i>B</i>	72.74 (0.90)	0.16 (01)	454 (50)	-19.090 (023)	-0.92 (13)	-0.53 (49)	-0.01 (01)	2.90 (09)
	<i>g</i>	73.94 (1.54)	0.13 (01)	474 (47)	-19.109 (045)	-0.99 (14)	-0.94 (39)	-0.01 (01)	2.51 (09)
	<i>V</i>	72.86 (0.87)	0.16 (01)	478 (53)	-19.080 (026)	-1.20 (12)	-1.59 (36)	-0.02 (01)	1.96 (1)
	<i>r</i>	72.03 (0.86)	0.15 (01)	459 (48)	-19.048 (022)	-0.79 (10)	0.17 (40)	-0.02 (01)	1.47 (07)
	<i>i</i>	72.65 (0.78)	0.12 (01)	453 (43)	-18.446 (021)	-0.46 (07)	0.22 (25)	-0.03 (00)	1.04 (06)
	<i>Y</i>	70.92 (1.37)	0.10 (01)	377 (39)	-18.506 (041)	-0.17 (08)	0.84 (25)	-0.03 (01)	0.52 (06)
	<i>J</i>	71.15 (1.10)	0.14 (01)	363 (41)	-18.710 (029)	-0.35 (12)	0.86 (34)	-0.04 (01)	0.47 (08)
<i>H</i>	69.36 (1.04)	0.11 (01)	390 (47)	-18.526 (028)	-0.09 (11)	1.44 (29)	-0.03 (01)	0.21 (08)	

**Figure 6.** H_0 across various bands. Values of H_0 are taken from Table 4. See text for discussion.**Figure 7.** H_0 across various bands in TRGB calibration. See text for discussion.

1.28 $\text{km s}^{-1} \text{Mpc}^{-1}$ in *H*-band. These values of σ_{H_0}

are the systematic uncertainties as determined

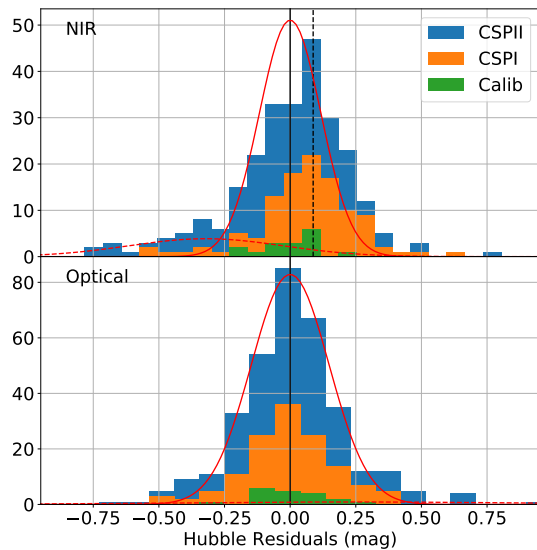


Figure 8. The Hubble diagram residuals in the optical (bottom panel) and NIR (top panel). The histograms are stacked with the green corresponding to the TRGB calibrations, the orange corresponding to the CSP-I sample, and the blue corresponding to the CSP-II. A two-component Gaussian fit is shown for the NIR residuals. **The vertical dashed line shows the location of zero-residuals in the NIR if we force H_0 to the value that we obtain from optical.**

Table 6. Effect of host mass correction in determining H_0 . We do not find significant differences in H_0 whether host mass correction is applied or not. Shown here are the values of H_0 from B -band light-curve fits and using various distance calibration.

Calibration	H_0 (km s $^{-1}$ Mpc $^{-1}$)	
	Linear correction	No correction
Cepheid	72.24 (0.74)	72.37 (0.71)
TRGB	70.31 (0.70)	70.25 (0.71)
SBF	72.62 (0.90)	72.45 (0.94)

from the variation of distance scales among the calibrators.

Adding systematic errors to H_0 , we can write $H_0 = 71.76 \pm 0.58$ (stat) ± 1.19 (sys) km s $^{-1}$ Mpc $^{-1}$ from SNe Ia B -band luminosity, and $H_0 = 73.22 \pm 0.68$ (stat) ± 1.28 (sys) km s $^{-1}$ Mpc $^{-1}$ from SNe Ia H -band luminosity. These results provide important insight on the differences in H_0 that we see from various calibrators. The most recent result from the SH0Es program (Riess et al. 2022), that uses Cepheid calibrators, reports $H_0 = 73.04 \pm 1.04$ (total) km s $^{-1}$ Mpc $^{-1}$. The CCHP program (Freedman 2021), that uses TRGB calibrators, reports

$H_0 = 69.80 \pm 0.60$ (stat) ± 1.6 (sys) km s $^{-1}$ Mpc $^{-1}$. Moreover, using SBF calibrators, Garnavich et al. (2022) reports $H_0 = 74.60 \pm 0.90$ (stat) ± 2.7 (sys) km s $^{-1}$ Mpc $^{-1}$ and Khetan et al. (2021) reports $H_0 = 70.50 \pm 2.37$ (stat) ± 3.38 (sys) km s $^{-1}$ Mpc $^{-1}$. **If we combine Cepheids, TRGB and the space-based SBF from Jensen et al. (2021) (i.e., excluding the ground-based SBF from Khetan et al. 2021) we find $H_0 = 72.21 \pm 0.60$ (stat) km s $^{-1}$ Mpc $^{-1}$ for B -band.** It is evident from our analysis that the differences in H_0 between previously published studies can be explained simply by the systematic differences in the SN Ia distance scales among various calibrators.

It is not immediately clear what could cause this level of disagreement between different calibration methods. Therefore, we will not give preference to one method over others. Our measurements of H_0 with added systematic uncertainties can be considered as representative values of H_0 with the current state of uncertainty in the SN Ia distance scale. We visualize these numbers in Figure 9.

4.2. SN Ia Hubble Residual and Intrinsic Luminosity Scatter

In this section, we investigate the precision of SNe Ia distances as a function of the observed photometric band by investigating the Hubble residuals. Hubble residuals ($\Delta\mu$) are the differences between the observed and the predicted distance moduli in the sense that a negative $\Delta\mu$ indicates an over-luminous SN Ia compared to its expected brightness, after corrections and distance predicted by the Hubble-Lemaître law. Hubble residuals when plotted against redshifts show how well the model fits the data. In Figure 10 we show Hubble residuals in $uBgVriYJH$ bands when Cepheid calibration is used in determining H_0 .

A parameter we are interested to study is the intrinsic luminosity scatter of SNe Ia, σ_{int} , introduced earlier. This term describes how well we can standardize SN Ia distances. It will be interesting to see how σ_{int} varies between optical and near-infrared bands, and at which band it has the smallest value. Smaller values of σ_{int} indicate better calibration. We present σ_{int} for the whole sample in Table 4. We also show the same, but excluding 91T and 91bg-like SNe Ia, in Table 5. Figure 11 shows σ_{int} as a function of wavelength for various cases in Cepheid calibration.

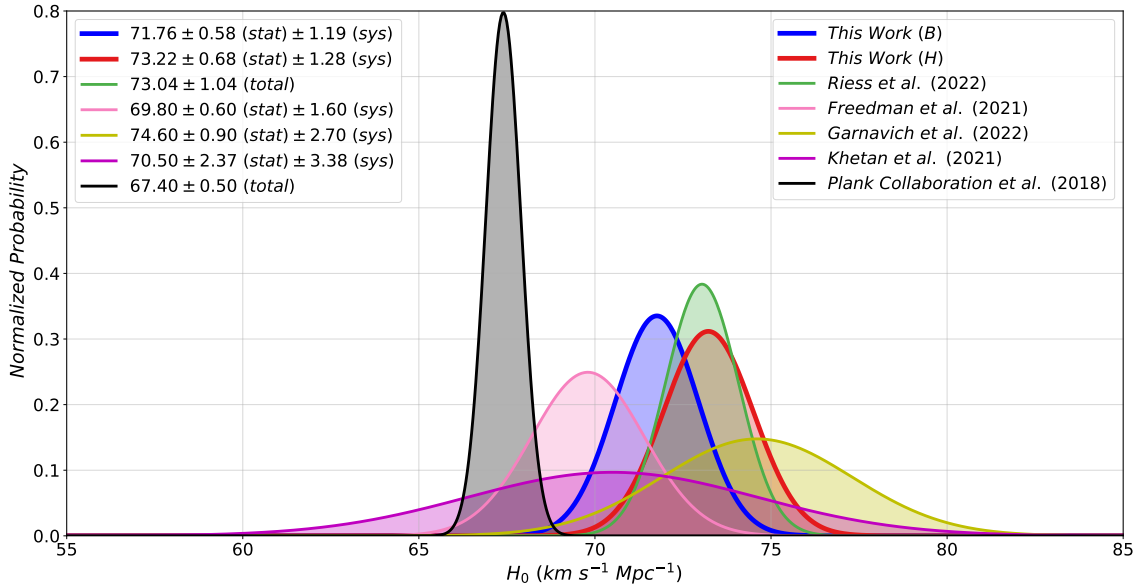
It is easy to see that σ_{int} is reduced in all bands when excluding 91T and 91bg-like objects, but this reduction is not significant. In both cases, we find that SNe Ia show the smallest value of σ_{int} in the Y -band. This can be visually inspected in Figure 10, where we see the

Table 7. Determination of H_0 from the combined Cepheid, TRGB, and SBF distance calibrators.

Band	H_0 ($\text{km s}^{-1} \text{Mpc}^{-1}$)	σ_{int} (mag)	V_{pec} (km s^{-1})	$P0$ (mag)	$P1$ (mag)	$P2$ (mag)	α (mag/dex)	β
<i>B</i>	71.76 (0.58)	0.17 (01)	466 (56)	-19.138 (01)	-1.48 (09)	-1.76 (26)	-0.02 (00)	2.90 (06)
<i>H</i>	73.22 (0.68)	0.16 (01)	373 (48)	-18.451 (011)	-0.18 (09)	1.13 (26)	-0.07 (00)	0.23 (06)

Table 8. Absolute magnitude (M) of various calibrating SNe I as discussed in §4.1. We convert error in the absolute magnitude (σ_{P0}) of distant SNe Ia to corresponding σ_{H_0} . The values of σ_{H_0} represent the systematic uncertainty in H_0 that originates from the variation in the SN Ia luminosity among various distance calibrators.

Parameter	Values			
	M_B (mag)	$\sigma_{H_0}(B)$ ($\text{km s}^{-1} \text{Mpc}^{-1}$)	M_H (mag)	$\sigma_{H_0}(H)$ ($\text{km s}^{-1} \text{Mpc}^{-1}$)
$P0_{dist}$	-19.147 (038)		-18.435 (040)	
$P0_{Cepheid}$	-19.138 (037)		-18.400 (040)	
$P0_{TRGB}$	-19.165 (047)	1.19	-18.476 (050)	1.28
$P0_{SBF}$	-19.105 (036)		-18.462 (044)	


Figure 9. Normalized probability distributions of H_0 . We show H_0 for *B* and *H* bands that we obtain from combining Cepheid, TRGB, and SBF distance calibrations. We also show most recent H_0 measurements from Riess et al. (2022), Freedman (2021), Garnavich et al. (2022), Khetan et al. (2021), and Planck Collaboration et al. (2018). Combined statistical and systematic errors are used to construct these distributions. It is easy to see the effect of systematic uncertainties that are dominating in each case. We discuss this in detail in §4.1. Note that the two H_0 values from this work overlap with all SN Ia based published H_0 values shown here.

scatter in SN Ia distances is the smallest in the Y -band. Red curves represent the combined uncertainty due to V_{pec} and σ_{int} . The effect of V_{pec} becomes insignificant for redshifts greater than ~ 0.02 .

It is interesting to note that, among the three near-infrared bands (YJH), Y provides the best calibration, and σ_{int} increases as one moves to longer wavelengths. While the number of available calibrators in Y -band is smaller (see Table 2), Phillips (2012) interprets this as being due to a combined effect of higher signal-to-noise and relative insensitivity to color effects (both reddening from dust and intrinsic color variations).

4.3. Effect of Various Cuts

So far, we have studied H_0 and σ_{int} both from our full sample and when excluding 91T and 91bg-like SNe Ia. In this section, we apply various cuts and perform additional calculations for a number of specific cases. We exclude: low-redshift objects ($z < 0.01$), faster decliners ($s_{BV} < 0.5$), redder objects ($B - V > 0.5$ mag), and objects for which the earliest observation is later than five days post maximum ($t_0 > 5$ day). We also combine all these cuts. Values of H_0 and σ_{int} using these cuts are shown in Table 9 for Cepheid calibration, in Table 10 for TRGB calibration, and in Table 11 for SBF calibration. In Table 12 we show the same combining all three calibrators in B and H bands.

It is interesting to note that (when comparing with Table 4) excluding low-redshift SNe Ia increases (with low significance) σ_{int} in all bands (see Figure 11). Note that in this case V_{pec} decreases. It is because they both contribute to the denominator of the χ^2 . In all other cuts, we do not see appreciable changes in σ_{int} . When we combine all cuts, the $z > 0.01$ cut dominates the change in σ_{int} . As we have seen before, σ_{int} is the smallest in the Y band, especially for $t_0 < 5$ days, where we find $\sigma_{int} = 0.11 \pm 0.01$ mag.

It has been suggested that SNe Ia in the near-infrared could be better standard candles since the effect of dust is reduced. A few studies (e.g. Krisciunas et al. 2004, Barone-Nugent et al. 2012, Avelino et al. 2019, Peterson et al. 2023, and Do et al. in preparation) present Hubble residual dispersion and σ_{int} of SNe Ia in near-infrared bands, but do not compare the same SNe Ia with the optical bands. Also, these studies are made with either a much smaller sample or with a number of selection criteria. Our results do not show a monotonic decrease in σ_{int} from optical to near-infrared, but we do find the smallest σ_{int} in the Y -band, and the second-smallest in the H -band.

We recall that in § 3.2, we found values of H_0 in YJH bands to be higher in TRGB calibration and lower in

SBF calibration. Here, we see that, except for $z > 0.01$ cut, TRGB gives consistent values of H_0 across various bands. However, these cuts do not make SBF-based H_0 consistent between optical and near-infrared.

Exploring the values of H_0 by applying various cuts, we can investigate the scatter that is introduced in H_0 measurements due to SNe Ia sample selection. To compute this scatter, we gather all H_0 measurements in a given band for a particular calibration, and calculate the standard deviation. We show these scatters in Table 13 for B and H band.

We find comparable scatter between B and H bands in the Cepheid and SBF calibrations. In the TRGB calibration, we find larger scatter in H band compared to B band. Also, H_0 is the least sensitive to SNe Ia sample selection in the TRGB calibration in the optical ($0.14 \text{ km s}^{-1} \text{ Mpc}^{-1}$), and most sensitive in the combined calibration ($0.60 \text{ km s}^{-1} \text{ Mpc}^{-1}$) followed by the Cepheid calibration ($0.46 \text{ km s}^{-1} \text{ Mpc}^{-1}$) in the near-infrared. Finally, we investigate inter-band scatter for various criteria. They are shown in Table 14.

4.4. SN Ia-Host Correlation

4.4.1. SN Ia Luminosity-Host Mass

A number of works have studied the correlations between the properties of SNe Ia and their hosts (e.g., Uddin et al. 2020; Ponder et al. 2021; Johansson et al. 2021; Uddin et al. 2017b; Sullivan et al. 2010; Lampeitl et al. 2010; Neill et al. 2009; Childress et al. 2013; Rigault et al. 2013; Roman et al. 2018; Brown & Crumpler 2020 and references therein). The most significant outcome is how the decline-rate and color-corrected luminosity of SNe Ia varies with the stellar mass of their host galaxies. In contrast to most other studies, Uddin et al. (2020), using CSP-I data, showed this correlation in nine bandpasses ($uBgVriYJH$), and found evidence that the correlation between SN Ia luminosity and host mass is insignificant except for the u -band. They also found that the Hubble residual offsets (Δ_{HR}) do not vary strongly from optical to near-infrared wavelengths. Here, we define Δ_{HR} as the difference of mean $\Delta\mu$ of SNe Ia between massive hosts and low-mass hosts, often called the mass-step. In this work, CSP-I data have been refit with the latest SNOOPy version, and we obtain a different set of Δ_{HR} values, which weakens correlations and mass-steps¹⁷.

We find similar results using the CSP-II and the combined CSP-I & II samples. We show the correlation between $\Delta\mu$ and host galaxy mass from this work in

¹⁷ For example, in Uddin et al. (2020), Δ_{HR} in the u -band was 0.147 ± 0.044 mag for CSP-I data, compared to 0.090 ± 0.088 mag for the same sample in this work.

Table 9. H_0 and all other nuisance parameters in Cepheid calibration when applying various cuts.

Selection	Band	H_0 (km s ⁻¹ Mpc ⁻¹)	σ_{int} (mag)	V_{pec} (km s ⁻¹)	$P0$ (mag)	$P1$ (mag)	$P2$ (mag)	α (mag/dex)	β
$z > 0.01$	<i>u</i>	74.02 (1.13)	0.25 (01)	184 (122)	-18.705 (022)	-1.87 (14)	-2.13 (44)	-0.06 (01)	4.38 (13)
	<i>B</i>	72.60 (0.73)	0.19 (01)	189 (97)	-19.110 (015)	-1.22 (09)	-1.18 (28)	-0.02 (01)	3.03 (07)
	<i>g</i>	73.40 (0.97)	0.17 (01)	268 (88)	-19.140 (023)	-1.18 (10)	-1.19 (31)	-0.03 (01)	2.61 (09)
	<i>V</i>	72.75 (0.70)	0.19 (01)	222 (95)	-19.106 (014)	-1.25 (09)	-1.45 (27)	-0.02 (00)	2.10 (07)
	<i>r</i>	71.75 (0.64)	0.18 (01)	252 (74)	-19.062 (014)	-1.11 (08)	-0.80 (25)	-0.03 (00)	1.57 (07)
	<i>i</i>	72.89 (0.62)	0.17 (01)	239 (73)	-18.452 (014)	-0.72 (07)	-0.43 (24)	-0.03 (00)	1.11 (06)
	<i>Y</i>	72.82 (0.78)	0.13 (01)	186 (76)	-18.469 (020)	-0.38 (07)	0.65 (22)	-0.03 (00)	0.53 (06)
	<i>J</i>	74.95 (0.72)	0.19 (01)	202 (112)	-18.611 (015)	-0.68 (09)	0.08 (29)	-0.03 (01)	0.56 (08)
	<i>H</i>	73.97 (0.73)	0.16 (01)	184 (98)	-18.377 (014)	-0.38 (09)	0.44 (28)	-0.03 (01)	0.27 (07)
$s_{BV} > 0.5$	<i>u</i>	73.64 (1.15)	0.22 (02)	497 (66)	-18.698 (021)	-1.90 (13)	-2.57 (53)	-0.06 (01)	4.30 (14)
	<i>B</i>	72.48 (0.74)	0.17 (01)	457 (51)	-19.108 (015)	-1.24 (09)	-1.33 (36)	-0.02 (01)	3.03 (08)
	<i>g</i>	73.21 (0.99)	0.14 (01)	486 (50)	-19.139 (024)	-1.20 (10)	-1.45 (41)	-0.03 (01)	2.58 (10)
	<i>V</i>	72.59 (0.75)	0.17 (01)	472 (50)	-19.105 (015)	-1.28 (08)	-1.57 (34)	-0.02 (01)	2.08 (08)
	<i>r</i>	71.60 (0.66)	0.16 (01)	461 (45)	-19.061 (015)	-1.13 (08)	-0.79 (35)	-0.03 (00)	1.55 (07)
	<i>i</i>	72.68 (0.65)	0.15 (01)	441 (44)	-18.453 (014)	-0.73 (08)	-0.50 (30)	-0.03 (00)	1.09 (06)
	<i>Y</i>	72.47 (0.82)	0.12 (01)	371 (41)	-18.464 (020)	-0.40 (07)	0.37 (31)	-0.02 (00)	0.47 (06)
	<i>J</i>	74.28 (0.76)	0.16 (01)	391 (51)	-18.605 (015)	-0.74 (09)	-0.83 (37)	-0.02 (01)	0.46 (08)
	<i>H</i>	73.66 (0.77)	0.13 (01)	382 (50)	-18.374 (015)	-0.46 (10)	-0.17 (46)	-0.02 (01)	0.22 (07)
$B - V < 0.5$ (mag)	<i>u</i>	73.96 (1.09)	0.23 (02)	432 (64)	-18.699 (021)	-1.92 (13)	-2.41 (57)	-0.06 (01)	4.24 (16)
	<i>B</i>	72.60 (0.72)	0.18 (01)	372 (50)	-19.107 (015)	-1.23 (09)	-1.01 (37)	-0.01 (01)	2.86 (11)
	<i>g</i>	73.30 (0.94)	0.15 (01)	390 (46)	-19.140 (023)	-1.20 (09)	-0.98 (41)	-0.02 (01)	2.36 (14)
	<i>V</i>	72.75 (0.72)	0.18 (01)	369 (46)	-19.103 (015)	-1.25 (08)	-1.17 (36)	-0.02 (01)	1.92 (10)
	<i>r</i>	71.90 (0.64)	0.17 (01)	365 (43)	-19.057 (014)	-1.10 (08)	-0.34 (33)	-0.02 (00)	1.33 (09)
	<i>i</i>	72.84 (0.66)	0.15 (01)	367 (44)	-18.448 (014)	-0.72 (07)	-0.32 (31)	-0.02 (00)	0.96 (10)
	<i>Y</i>	72.39 (0.84)	0.12 (01)	343 (41)	-18.463 (022)	-0.41 (07)	0.20 (31)	-0.02 (00)	0.46 (10)
	<i>J</i>	74.31 (0.81)	0.16 (01)	368 (53)	-18.607 (016)	-0.76 (09)	-1.03 (38)	-0.03 (01)	0.57 (12)
	<i>H</i>	73.60 (0.76)	0.13 (01)	367 (49)	-18.375 (015)	-0.47 (09)	-0.46 (41)	-0.03 (01)	0.29 (11)
$t_0 < 5$ (day)	<i>u</i>	73.70 (1.15)	0.22 (02)	494 (67)	-18.708 (021)	-1.88 (14)	-2.24 (44)	-0.06 (01)	4.42 (13)
	<i>B</i>	72.27 (0.73)	0.17 (01)	443 (52)	-19.112 (015)	-1.25 (10)	-1.27 (30)	-0.02 (01)	3.05 (08)
	<i>g</i>	73.12 (0.98)	0.14 (01)	471 (48)	-19.145 (023)	-1.20 (11)	-1.25 (34)	-0.03 (01)	2.63 (10)
	<i>V</i>	72.49 (0.71)	0.18 (01)	459 (48)	-19.107 (015)	-1.29 (09)	-1.47 (29)	-0.02 (01)	2.10 (08)
	<i>r</i>	71.52 (0.66)	0.17 (01)	444 (47)	-19.061 (014)	-1.14 (08)	-0.81 (28)	-0.03 (00)	1.57 (07)
	<i>i</i>	72.72 (0.66)	0.15 (01)	435 (45)	-18.455 (014)	-0.73 (08)	-0.41 (24)	-0.03 (01)	1.11 (07)
	<i>Y</i>	72.67 (0.85)	0.11 (01)	379 (46)	-18.466 (023)	-0.37 (08)	0.77 (25)	-0.02 (00)	0.51 (08)
	<i>J</i>	74.72 (0.82)	0.17 (01)	371 (54)	-18.609 (016)	-0.70 (10)	0.26 (33)	-0.02 (01)	0.48 (08)
	<i>H</i>	74.17 (0.74)	0.13 (01)	374 (50)	-18.374 (015)	-0.38 (10)	0.59 (33)	-0.02 (01)	0.19 (08)
All cuts	<i>u</i>	73.49 (1.19)	0.24 (02)	191 (122)	-18.700 (022)	-1.92 (13)	-2.59 (55)	-0.06 (01)	4.35 (17)
	<i>B</i>	72.55 (0.76)	0.19 (01)	147 (97)	-19.106 (016)	-1.25 (08)	-1.16 (39)	-0.01 (01)	2.93 (11)
	<i>g</i>	73.04 (0.94)	0.17 (01)	213 (89)	-19.140 (022)	-1.21 (10)	-1.15 (42)	-0.03 (01)	2.46 (14)
	<i>V</i>	72.62 (0.73)	0.20 (01)	148 (93)	-19.102 (015)	-1.27 (09)	-1.33 (36)	-0.01 (01)	1.96 (11)
	<i>r</i>	71.77 (0.65)	0.18 (01)	194 (90)	-19.058 (014)	-1.11 (08)	-0.48 (36)	-0.02 (00)	1.40 (10)
	<i>i</i>	72.73 (0.66)	0.17 (01)	207 (92)	-18.452 (014)	-0.75 (08)	-0.40 (33)	-0.03 (00)	1.01 (09)
	<i>Y</i>	72.52 (0.83)	0.14 (01)	186 (94)	-18.464 (022)	-0.39 (08)	0.36 (33)	-0.02 (00)	0.51 (10)
	<i>J</i>	73.76 (0.85)	0.18 (01)	195 (116)	-18.609 (016)	-0.76 (10)	-0.95 (48)	-0.03 (01)	0.63 (12)
	<i>H</i>	73.22 (0.75)	0.15 (01)	193 (101)	-18.373 (015)	-0.45 (09)	-0.58 (41)	-0.02 (01)	0.21 (11)

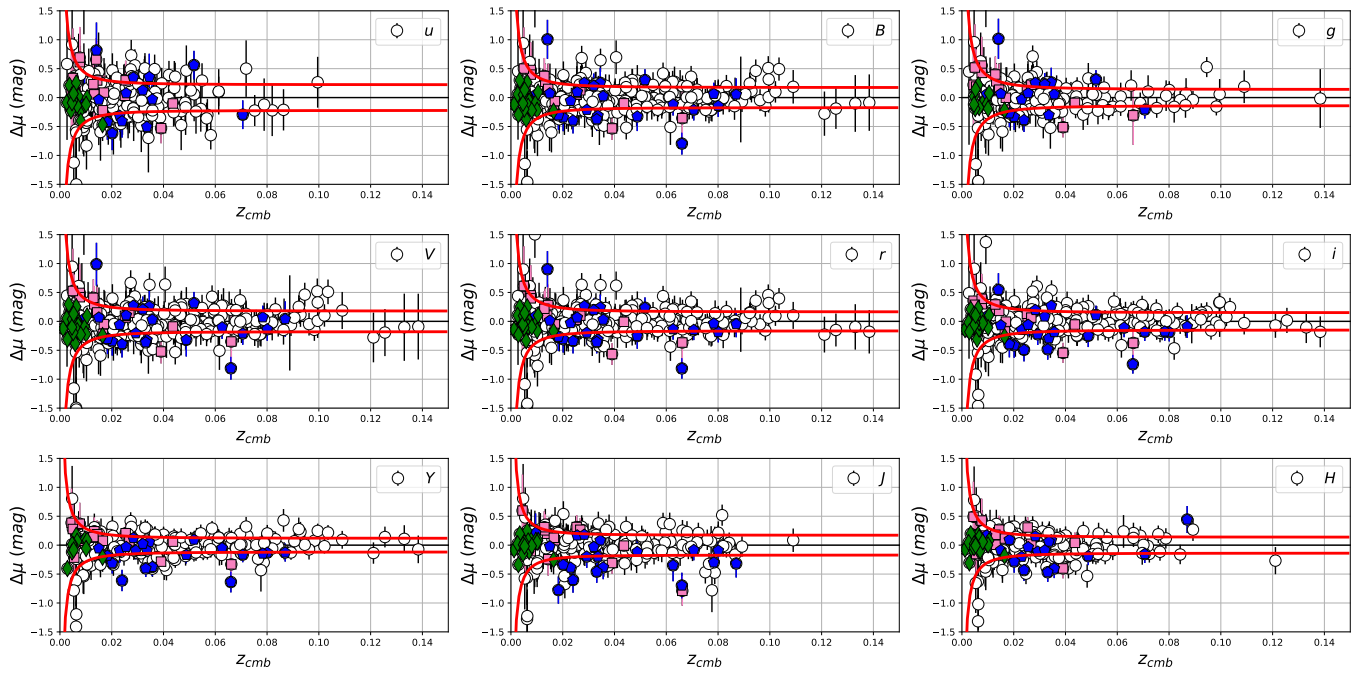


Figure 10. Hubble residuals in different bands with the Cepheid calibration. The red curves are combined errors due to peculiar velocity (V_{pec}) and intrinsic scatter (σ_{int}). Blue points are 91T-like, and pink squares are 91bg-like objects. Green diamonds are Cepheid calibrators.

Table 10. H_0 and all other nuisance parameters in TRGB calibration when applying various cuts.

Selection	Band	H_0 ($\text{km s}^{-1} \text{Mpc}^{-1}$)	σ_{int} (mag)	V_{pec} (km s^{-1})	$P0$ (mag)	$P1$ (mag)	$P2$ (mag)	α (mag/dex)	β
$z > 0.01$	<i>u</i>	69.00 (1.00)	0.25 (01)	193 (120)	-18.863 (025)	-1.46 (14)	-0.31 (44)	-0.07 (02)	3.89 (11)
	<i>B</i>	70.21 (0.67)	0.19 (01)	200 (94)	-19.178 (016)	-1.11 (09)	-0.67 (25)	-0.00 (01)	2.87 (06)
	<i>g</i>	71.09 (1.25)	0.17 (01)	251 (89)	-19.209 (033)	-1.06 (10)	-0.66 (32)	-0.01 (01)	2.51 (09)
	<i>V</i>	70.12 (0.65)	0.20 (01)	225 (100)	-19.178 (015)	-1.19 (08)	-0.98 (23)	-0.01 (01)	1.90 (06)
	<i>r</i>	69.31 (0.61)	0.18 (01)	242 (79)	-19.137 (015)	-0.94 (09)	-0.10 (25)	-0.01 (01)	1.43 (05)
	<i>i</i>	69.77 (0.58)	0.17 (01)	237 (79)	-18.542 (014)	-0.56 (07)	0.07 (21)	-0.01 (00)	0.98 (05)
	<i>Y</i>	72.13 (1.04)	0.13 (01)	175 (73)	-18.491 (029)	-0.32 (07)	0.76 (21)	-0.03 (01)	0.54 (06)
	<i>J</i>	72.29 (0.75)	0.19 (01)	149 (103)	-18.688 (016)	-0.56 (10)	0.69 (27)	-0.04 (01)	0.34 (06)
<i>H</i>	70.80 (0.71)	0.17 (01)	153 (95)	-18.482 (015)	-0.25 (09)	0.89 (27)	-0.05 (01)	0.21 (06)	
$s_{B-V} > 0.5$	<i>u</i>	68.82 (1.03)	0.23 (02)	463 (63)	-18.862 (027)	-1.53 (15)	-0.55 (53)	-0.07 (02)	3.87 (11)
	<i>B</i>	70.22 (0.69)	0.17 (01)	442 (49)	-19.176 (016)	-1.12 (09)	-0.69 (31)	-0.00 (01)	2.85 (07)
	<i>g</i>	70.94 (1.23)	0.14 (01)	473 (50)	-19.217 (035)	-1.08 (11)	-0.59 (40)	-0.01 (01)	2.51 (09)
	<i>V</i>	69.92 (0.62)	0.18 (01)	462 (51)	-19.177 (015)	-1.21 (09)	-1.11 (27)	-0.01 (01)	1.87 (06)
	<i>r</i>	69.18 (0.64)	0.17 (01)	452 (46)	-19.142 (015)	-0.94 (08)	0.04 (28)	-0.01 (01)	1.45 (06)
	<i>i</i>	69.70 (0.59)	0.15 (01)	439 (45)	-18.541 (014)	-0.56 (07)	0.03 (24)	-0.01 (00)	0.97 (05)
	<i>Y</i>	72.03 (0.99)	0.12 (01)	364 (40)	-18.482 (03)	-0.33 (07)	0.57 (28)	-0.02 (01)	0.48 (06)
	<i>J</i>	72.24 (0.74)	0.17 (01)	345 (49)	-18.672 (017)	-0.65 (10)	-0.01 (33)	-0.04 (01)	0.24 (06)
<i>H</i>	70.80 (0.71)	0.14 (01)	356 (48)	-18.480 (015)	-0.29 (11)	0.73 (37)	-0.05 (01)	0.17 (06)	
$B - V < 0.5$ (mag)	<i>u</i>	69.25 (1.02)	0.23 (01)	389 (57)	-18.844 (025)	-1.51 (14)	-0.38 (47)	-0.06 (02)	3.68 (12)
	<i>B</i>	70.52 (0.66)	0.18 (01)	359 (46)	-19.167 (016)	-1.11 (08)	-0.51 (28)	0.00 (01)	2.68 (08)
	<i>g</i>	70.17 (1.17)	0.15 (01)	374 (46)	-19.236 (033)	-1.04 (10)	-0.10 (37)	-0.01 (01)	2.17 (13)
	<i>V</i>	70.29 (0.64)	0.18 (01)	358 (46)	-19.169 (015)	-1.19 (08)	-0.87 (24)	-0.00 (01)	1.68 (07)
	<i>r</i>	69.61 (0.61)	0.17 (01)	350 (42)	-19.128 (014)	-0.92 (08)	0.20 (25)	0.00 (00)	1.25 (07)
	<i>i</i>	69.94 (0.62)	0.15 (01)	361 (45)	-18.530 (014)	-0.56 (07)	0.14 (22)	-0.00 (00)	0.81 (07)
	<i>Y</i>	72.10 (1.07)	0.12 (01)	332 (41)	-18.478 (029)	-0.33 (07)	0.47 (27)	-0.02 (01)	0.49 (10)
	<i>J</i>	72.32 (0.71)	0.18 (01)	320 (51)	-18.671 (016)	-0.65 (10)	0.04 (33)	-0.04 (01)	0.18 (08)
<i>H</i>	70.82 (0.71)	0.15 (01)	332 (45)	-18.479 (016)	-0.31 (12)	0.59 (42)	-0.05 (01)	0.15 (08)	
$t_0 < 5$ (day)	<i>u</i>	68.60 (1.01)	0.23 (02)	450 (65)	-18.867 (024)	-1.51 (15)	-0.40 (45)	-0.08 (02)	3.93 (11)
	<i>B</i>	70.09 (0.68)	0.18 (01)	421 (51)	-19.178 (015)	-1.13 (09)	-0.67 (26)	-0.01 (01)	2.87 (06)
	<i>g</i>	70.89 (1.22)	0.15 (01)	453 (48)	-19.212 (032)	-1.08 (11)	-0.62 (34)	-0.02 (01)	2.51 (10)
	<i>V</i>	69.84 (0.63)	0.18 (01)	450 (51)	-19.179 (015)	-1.23 (09)	-1.00 (24)	-0.01 (01)	1.88 (06)
	<i>r</i>	69.14 (0.64)	0.17 (01)	438 (46)	-19.138 (014)	-0.96 (09)	-0.08 (27)	-0.01 (01)	1.43 (06)
	<i>i</i>	69.69 (0.59)	0.15 (01)	435 (48)	-18.542 (014)	-0.56 (08)	0.14 (22)	-0.01 (01)	0.98 (06)
	<i>Y</i>	71.46 (1.03)	0.11 (01)	369 (44)	-18.502 (028)	-0.28 (08)	0.89 (24)	-0.02 (01)	0.54 (07)
	<i>J</i>	71.96 (0.79)	0.17 (01)	341 (52)	-18.687 (017)	-0.55 (11)	0.87 (30)	-0.03 (01)	0.29 (07)
<i>H</i>	70.92 (0.74)	0.14 (01)	354 (47)	-18.480 (016)	-0.21 (10)	1.10 (29)	-0.05 (01)	0.14 (06)	
All cuts	<i>u</i>	68.69 (1.09)	0.23 (02)	179 (125)	-18.856 (031)	-1.26 (21)	0.71 (91)	-0.03 (02)	3.69 (15)
	<i>B</i>	70.32 (0.68)	0.16 (01)	225 (93)	-19.173 (016)	-1.16 (10)	-0.26 (44)	0.00 (01)	2.66 (1)
	<i>g</i>	68.89 (1.19)	0.14 (01)	211 (74)	-19.290 (036)	-0.98 (11)	1.32 (46)	0.00 (01)	1.60 (25)
	<i>V</i>	70.03 (0.68)	0.17 (01)	222 (89)	-19.169 (016)	-1.27 (08)	-0.85 (27)	0.00 (01)	1.62 (09)
	<i>r</i>	69.14 (0.65)	0.15 (01)	267 (71)	-19.140 (015)	-1.00 (08)	0.70 (30)	0.00 (00)	1.25 (09)
	<i>i</i>	69.69 (0.65)	0.14 (01)	293 (85)	-18.534 (016)	-0.59 (08)	0.43 (26)	0.00 (00)	0.78 (09)
	<i>Y</i>	71.21 (1.14)	0.13 (01)	166 (103)	-18.497 (034)	-0.31 (08)	0.64 (36)	-0.02 (01)	0.65 (22)
	<i>J</i>	72.06 (0.84)	0.18 (01)	116 (93)	-18.672 (017)	-0.57 (13)	0.53 (47)	-0.03 (01)	0.13 (09)
<i>H</i>	70.99 (0.85)	0.15 (02)	261 (130)	-18.476 (017)	-0.27 (12)	0.84 (44)	-0.05 (01)	0.10 (07)	

Table 11. H_0 and all other nuisance parameters in combined SBF calibration when applying various cuts.

Selection	Band	H_0 ($\text{km s}^{-1} \text{Mpc}^{-1}$)	σ_{int} (mag)	V_{pec} (km s^{-1})	$P0$ (mag)	$P1$ (mag)	$P2$ (mag)	α (mag/dex)	β
$z > 0.01$	<i>u</i>	69.71 (1.35)	0.25 (01)	180 (123)	-18.839 (040)	-1.36 (16)	-0.26 (47)	-0.01 (02)	4.07 (14)
	<i>B</i>	72.73 (0.82)	0.19 (01)	215 (101)	-19.106 (020)	-0.98 (10)	-0.60 (35)	-0.00 (01)	2.93 (08)
	<i>g</i>	73.33 (1.38)	0.17 (01)	305 (85)	-19.136 (040)	-0.92 (11)	-0.62 (33)	-0.00 (01)	2.54 (09)
	<i>V</i>	72.55 (0.79)	0.19 (01)	265 (92)	-19.098 (020)	-1.19 (09)	-1.42 (26)	-0.01 (01)	2.01 (07)
	<i>r</i>	72.09 (0.75)	0.18 (01)	262 (81)	-19.057 (02)	-0.87 (08)	-0.10 (28)	-0.01 (01)	1.49 (07)
	<i>i</i>	72.39 (0.75)	0.16 (01)	255 (77)	-18.468 (019)	-0.60 (07)	-0.05 (23)	-0.02 (01)	1.04 (06)
	<i>Y</i>	69.66 (1.21)	0.13 (01)	181 (77)	-18.562 (038)	-0.35 (07)	0.68 (21)	-0.03 (01)	0.53 (06)
	<i>J</i>	70.10 (1.05)	0.19 (01)	180 (112)	-18.761 (028)	-0.63 (11)	0.39 (31)	-0.04 (01)	0.49 (08)
	<i>H</i>	68.31 (0.99)	0.16 (01)	173 (101)	-18.563 (026)	-0.34 (11)	0.94 (3)	-0.03 (01)	0.23 (08)
$s_{BV} > 0.5$	<i>u</i>	69.18 (1.47)	0.22 (02)	489 (67)	-18.861 (045)	-1.39 (17)	-0.16 (50)	-0.02 (02)	4.07 (14)
	<i>B</i>	72.64 (0.89)	0.17 (01)	464 (53)	-19.102 (023)	-1.00 (11)	-0.73 (39)	-0.00 (01)	2.92 (08)
	<i>g</i>	73.62 (1.55)	0.14 (01)	498 (49)	-19.124 (046)	-0.95 (12)	-0.80 (39)	-0.00 (01)	2.53 (09)
	<i>V</i>	72.63 (0.82)	0.17 (01)	479 (51)	-19.089 (021)	-1.22 (09)	-1.60 (26)	-0.01 (01)	1.98 (08)
	<i>r</i>	71.84 (0.80)	0.16 (01)	469 (47)	-19.064 (021)	-0.85 (09)	0.05 (34)	-0.01 (01)	1.49 (07)
	<i>i</i>	72.35 (0.76)	0.15 (01)	449 (46)	-18.466 (021)	-0.60 (08)	-0.07 (26)	-0.02 (01)	1.04 (06)
	<i>Y</i>	70.66 (1.40)	0.12 (01)	381 (41)	-18.521 (045)	-0.36 (08)	0.40 (29)	-0.02 (01)	0.48 (06)
	<i>J</i>	70.50 (1.06)	0.17 (01)	383 (49)	-18.739 (03)	-0.68 (12)	0.00 (35)	-0.03 (01)	0.41 (08)
	<i>H</i>	68.04 (0.99)	0.14 (01)	374 (48)	-18.575 (029)	-0.34 (11)	1.14 (30)	-0.03 (01)	0.20 (08)
$B - V < 0.5$ (mag)	<i>u</i>	68.77 (1.58)	0.23 (01)	410 (60)	-18.869 (047)	-1.36 (16)	0.26 (52)	-0.01 (02)	3.80 (18)
	<i>B</i>	72.07 (0.86)	0.18 (01)	390 (50)	-19.134 (025)	-0.79 (12)	0.78 (55)	0.01 (01)	2.45 (14)
	<i>g</i>	72.76 (1.47)	0.15 (01)	396 (47)	-19.150 (045)	-0.92 (11)	-0.23 (39)	0.01 (01)	2.24 (13)
	<i>V</i>	71.72 (0.84)	0.19 (01)	392 (53)	-19.155 (022)	-0.53 (08)	1.92 (25)	0.01 (01)	1.19 (11)
	<i>r</i>	71.46 (0.78)	0.17 (01)	366 (44)	-19.076 (021)	-0.82 (08)	0.63 (27)	-0.00 (01)	1.14 (10)
	<i>i</i>	72.06 (0.75)	0.15 (01)	378 (46)	-18.474 (020)	-0.59 (07)	0.23 (25)	-0.01 (01)	0.84 (08)
	<i>Y</i>	71.05 (1.47)	0.12 (01)	354 (43)	-18.505 (047)	-0.35 (07)	0.28 (31)	-0.02 (00)	0.48 (10)
	<i>J</i>	70.88 (1.13)	0.17 (01)	360 (52)	-18.733 (032)	-0.70 (11)	-0.16 (39)	-0.04 (01)	0.51 (13)
	<i>H</i>	68.16 (1.00)	0.14 (01)	357 (49)	-18.573 (029)	-0.36 (11)	1.02 (36)	-0.04 (01)	0.25 (13)
$t_0 < 5$ (day)	<i>u</i>	69.38 (1.44)	0.22 (02)	476 (67)	-18.847 (043)	-1.40 (17)	-0.40 (47)	-0.02 (02)	4.14 (14)
	<i>B</i>	72.43 (0.85)	0.17 (01)	449 (50)	-19.109 (022)	-1.01 (11)	-0.66 (39)	-0.00 (01)	2.93 (09)
	<i>g</i>	73.11 (1.40)	0.14 (01)	480 (50)	-19.139 (041)	-0.94 (12)	-0.66 (36)	-0.01 (01)	2.55 (10)
	<i>V</i>	72.22 (0.84)	0.17 (01)	471 (53)	-19.101 (021)	-1.22 (09)	-1.49 (25)	-0.01 (01)	2.02 (08)
	<i>r</i>	71.77 (0.77)	0.17 (01)	448 (48)	-19.060 (020)	-0.88 (09)	-0.05 (32)	-0.01 (01)	1.48 (08)
	<i>i</i>	72.12 (0.78)	0.15 (01)	441 (47)	-18.472 (021)	-0.60 (08)	0.01 (25)	-0.02 (01)	1.04 (07)
	<i>Y</i>	69.50 (1.33)	0.11 (01)	388 (43)	-18.560 (041)	-0.31 (09)	0.77 (26)	-0.02 (01)	0.53 (08)
	<i>J</i>	69.11 (1.08)	0.17 (01)	373 (55)	-18.781 (029)	-0.63 (12)	0.67 (32)	-0.02 (01)	0.41 (09)
	<i>H</i>	68.10 (0.96)	0.14 (01)	369 (51)	-18.575 (027)	-0.32 (12)	1.24 (27)	-0.03 (01)	0.15 (07)
All cuts	<i>u</i>	68.85 (1.51)	0.25 (01)	167 (117)	-18.861 (047)	-1.38 (17)	-0.00 (54)	-0.01 (02)	3.92 (19)
	<i>B</i>	72.15 (0.88)	0.20 (01)	167 (99)	-19.125 (024)	-0.86 (13)	0.30 (59)	0.01 (01)	2.56 (14)
	<i>g</i>	72.67 (1.49)	0.17 (01)	223 (94)	-19.147 (045)	-0.96 (11)	-0.45 (40)	-0.00 (01)	2.33 (14)
	<i>V</i>	72.21 (0.84)	0.19 (01)	173 (97)	-19.101 (023)	-1.18 (10)	-1.21 (33)	-0.00 (01)	1.76 (12)
	<i>r</i>	71.35 (0.77)	0.18 (01)	209 (92)	-19.078 (021)	-0.83 (08)	0.56 (30)	-0.00 (01)	1.16 (10)
	<i>i</i>	71.93 (0.78)	0.17 (01)	217 (95)	-18.477 (022)	-0.61 (07)	0.18 (27)	-0.01 (01)	0.88 (1)
	<i>Y</i>	70.80 (1.46)	0.14 (01)	181 (96)	-18.512 (046)	-0.33 (08)	0.34 (33)	-0.02 (01)	0.52 (11)
	<i>J</i>	69.86 (1.19)	0.19 (01)	179 (113)	-18.748 (034)	-0.69 (13)	0.02 (44)	-0.03 (01)	0.54 (15)
	<i>H</i>	67.90 (1.01)	0.16 (01)	169 (108)	-18.573 (028)	-0.33 (12)	1.13 (35)	-0.03 (01)	0.21 (12)

Table 12. H_0 and all other nuisance parameters in combined calibration when applying various cuts.

Selection	Band	H_0	σ_{int}	V_{pec}	$P0$	$P1$	$P2$	α	β
		(km s ⁻¹ Mpc ⁻¹)	(mag)	(km s ⁻¹)	(mag)	(mag)	(mag)	(mag/dex)	
$z > 0.01$	<i>B</i>	71.75 (0.64)	0.19 (01)	276 (110)	-19.139 (011)	-1.47 (08)	-1.71 (24)	-0.02 (00)	2.90 (06)
	<i>H</i>	73.14 (0.64)	0.17 (01)	311 (88)	-18.452 (011)	-0.19 (09)	1.06 (27)	-0.07 (00)	0.25 (06)
$s_{BV} > 0.5$	<i>B</i>	71.73 (0.59)	0.17 (01)	470 (56)	-19.133 (011)	-1.52 (09)	-1.99 (28)	-0.02 (00)	2.88 (06)
	<i>H</i>	73.31 (0.67)	0.15 (01)	396 (55)	-18.448 (012)	-0.18 (09)	1.10 (29)	-0.07 (00)	0.24 (06)
$(B - V) < 0.5$	<i>B</i>	71.94 (0.58)	0.17 (01)	395 (52)	-19.131 (01)	-1.46 (09)	-1.68 (28)	-0.02 (00)	2.75 (07)
	<i>H</i>	73.32 (0.62)	0.15 (01)	378 (59)	-18.448 (011)	-0.19 (09)	1.08 (30)	-0.07 (00)	0.21 (08)
$t_0 < 5$	<i>B</i>	71.58 (0.58)	0.17 (01)	478 (55)	-19.137 (010)	-1.50 (09)	-1.78 (28)	-0.02 (00)	2.91 (06)
	<i>H</i>	73.38 (0.74)	0.16 (02)	415 (57)	-18.446 (010)	-0.12 (09)	1.30 (27)	-0.07 (00)	0.22 (06)
All cuts	<i>B</i>	71.79 (0.59)	0.19 (01)	240 (107)	-19.133 (011)	-1.49 (09)	-1.78 (29)	-0.02 (00)	2.77 (07)
	<i>H</i>	73.35 (0.75)	0.16 (02)	396 (88)	-18.447 (011)	-0.14 (10)	1.16 (32)	-0.07 (00)	0.22 (08)

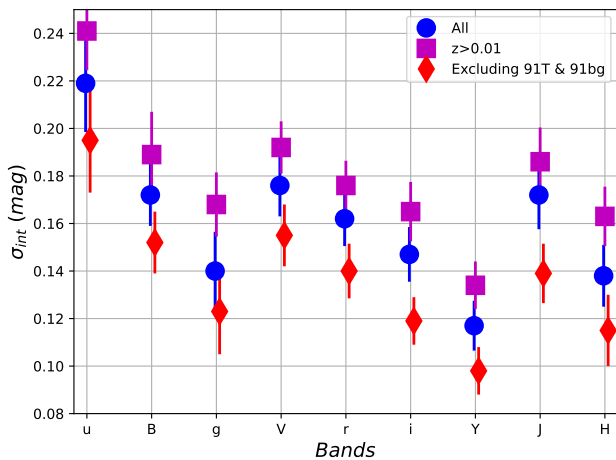

Figure 11. Variation of σ_{int} as a function of wavelength from optical to near-infrared in Cepheid calibration. We notice that σ_{int} decreases if 91T-like and 91bg-like SNe Ia are excluded. Including only distant SNe Ia ($z > 0.01$) increases σ_{int} (see §4.3).

Table 13. Scatter in H_0 from various sample cuts as seen in Tables 9, 10, and 11.

Calibration	Scatter in H_0 (km s ⁻¹ Mpc ⁻¹)	
	<i>B</i>	<i>H</i>
Cepheid	0.35	0.46
TRGB	0.14	0.33
SBF	0.22	0.20
Combined	0.17	0.60

Figure 12. Slopes and Δ_{HR} are given in Table 15. We also reproduce Figure 13 of Uddin et al. (2020) with more data from this work in Figure 13, where we show the behavior of Δ_{HR} across different bands.

With added data from CSP-II, we still find no significant Δ_{HR} , except for *u*-band, where the mass-step is -0.132 ± 0.071 mag ($\sim 2\sigma$). We also find no systematic variation of slope or Δ_{HR} with wavelength. Indeed, our results are consistent with there being no systematic correlation of Δ_{HR} with host galaxy mass.

On the other hand, the correlation between SN Ia Hubble residuals and host stellar mass as measured by the slopes between them show moderate significance ($2 - 3 \sigma$) in all bands except for the *H* band. In the *u*-band, the slope is maximum with a value of -0.075 ± 0.020 mag/dex.

While the origin of this correlation is not well established, Brout & Scolnic (2020) predicted a wavelength dependence of Δ_{HR} with a progressive decrease when moving from the optical to near-infrared (see Figure 13). Their prediction was based on different dust distributions (different R_V) in massive and low-mass hosts, and they concluded that dust is responsible for the observed mass-step. In contrast to their prediction, our results indicate that dust may not be responsible for Δ_{HR} , since we do not see variation of Δ_{HR} with wavelength. A study published by Ponder et al. (2021) is consistent with our findings that dust is not responsible for the observed mass-step, but the study by Johansson et al. (2021) is compatible with the findings in Brout & Scolnic (2020), i.e., it suggests that allowing for diversity in the extinction laws among host galaxies alleviates the need for a mass-step.

We note that SNe Ia in CSP-I were obtained from targeted surveys, and their hosts are mostly massive. Therefore, the initial disagreement with literature results could have been due to the lack of low-mass hosts in CSP-I. In CSP-II, SNe Ia came mostly from untargeted searches, and we have a mixture of massive and

Table 14. Inter-band scatter of H_0 for various cuts.

Calibration	Scatter in H_0 (km s ⁻¹ Mpc ⁻¹)						
	Full	No 91T/91bg	$z > 0.01$	$s_{BV} > 0.5$	$B - V < 0.5$ mag	$t_0 < 5$ day	All cuts
Cepheid	1.10	1.07	1.01	1.01	0.93	1.11	0.89
TRGB	1.24	1.19	1.20	1.21	1.09	1.20	1.01
SBF	1.42	2.07	2.08	2.04	2.03	2.19	2.11

low-mass hosts. However, the disagreement still holds with the addition of more low-mass hosts.

Previously, Childress et al. (2014) argued that the mass-step originates from the differences in progenitor age distributions. Distinguishing SNe Ia into prompt and tardy groups, their empirical formula predicts a redshift evolution of mass-step. But that prediction was not supported by the analysis made in Uddin et al. (2017b).

While it is debatable that dust or SN Ia progenitor age distributions explain a possible mass-step, the effect of metallicity should be investigated. There is a hint in our study that this may be the case. We find that the mass-step is relatively strong in u -band, and expected to be stronger in the ultraviolet (UV) wavelengths, if the variation in metallicity drives this correlation (Lentz et al. 2000; Brown et al. 2014). Studying this correlation using Hubble residuals calculated from UV may reveal the effect of metallicity, which will be investigated in a future work.

4.4.2. SN Ia Luminosity-Projected Distance

Using the CSP-I sample, Uddin et al. (2020) showed that SNe Ia that explode beyond 10 kpc from host centers have a smaller scatter in their Hubble residuals than those that explode within 10 kpc. We extend this study by adding CSP-II data. In Figure 14 we show the distribution of Hubble residuals according to the projected distance for the full CSP sample in various bands. We calculate the dispersion in Hubble residuals of SNe Ia inside and outside 10 kpc from host centers and list them in Table 16. Here, we also find a similar result with a larger sample, namely that SNe Ia beyond 10 kpc have a smaller dispersion in their Hubble residuals. Previously, Wang et al. (1997) performed a similar study where they showed that SNe Ia have 3-4 times less scatter in their observed peak brightness when they explode beyond 7.5 kpc from host centers. To see if the redshift affects this trend, we color code Figure 14 with redshift and find that there is no difference in redshift distributions between these two samples.

Uddin et al. (2020) performed a Monte Carlo simulation and showed that the observed differences in the standard deviations of these two subgroups of SNe Ia are statistically significant. Here we repeat the same

analysis and find that the mean of the differences in the scatter is 0.13 ± 0.05 mag.

To make a statistically robust conclusion, we performed a Kolmogorov–Smirnov (K-S) test to compare these two populations of SNe Ia, with one population inside and the other population outside 10 kpc of host centers. The null hypothesis of the non-parametric K-S is that the two distributions are drawn from the same parent distribution. One can reject the null hypothesis if:

$$D_{n,m} > c(\alpha) \sqrt{\frac{n+m}{n \times m}} \quad (8)$$

where $D_{n,m}$ is the D-statistic for two samples of size n and m . This quantifies the maximum difference between two cumulative distribution functions. For a given confidence level, α the quantity $c(\alpha)$ is defined as:

$$c(\alpha) = \sqrt{-\ln\left(\frac{\alpha}{2}\right)} \times \frac{1}{2} \quad (9)$$

We present K-S test results in Table 17. First, we calculate the D-statistic in each band. Then we calculate the term $c(\alpha)$ for a range of confidence levels (α), and select the α as soon as the null hypothesis rejection condition of Eqn. 8 is met. Cumulative distribution functions (CDF) for these two samples are shown in Figure 15.

It is not clear why we see smaller dispersion in SNe Ia luminosity beyond a distance of 10 kpc from their hosts. We speculate that it could be due to the decrease of dust as we move from the center of a galaxy to its outskirts. From Table 16 we find that the differences in dispersion are smaller in the near-infrared bands than those in the optical. We also notice that (see Figure 16) SNe Ia that explode within 10 kpc from their host exhibit a wider range in $(B - V)$ color compare to those that explode beyond 10 kpc. The larger scatter closer to host centers may also originate from the additional error due to host-galaxy subtraction, for which further investigations are needed.

Table 15. Slope of SN Ia luminosity-host mass correlation and Hubble residual offset in various bands.

Sample	Filter	Correlations		
		Slope (mag/dex)	Δ_{HR} (mag)	Median Host Mass Log (M_0/M_\odot)
CSP-I	<i>u</i>	-0.082 (0.050)	-0.096 (0.109)	10.50
	<i>B</i>	-0.034 (0.036)	-0.040 (0.094)	10.54
	<i>g</i>	-0.022 (0.036)	-0.021 (0.090)	10.54
	<i>V</i>	-0.041 (0.038)	-0.040 (0.095)	10.54
	<i>r</i>	-0.039 (0.033)	-0.054 (0.089)	10.54
	<i>i</i>	-0.034 (0.029)	-0.052 (0.086)	10.54
	<i>Y</i>	-0.061 (0.027)	-0.100 (0.083)	10.55
	<i>J</i>	-0.073 (0.033)	-0.096 (0.096)	10.58
	<i>H</i>	-0.024 (0.029)	-0.077 (0.092)	10.59
CSP-II	<i>u</i>	-0.078 (0.022)	-0.138 (0.104)	10.17
	<i>B</i>	-0.043 (0.013)	-0.109 (0.067)	9.95
	<i>g</i>	-0.042 (0.017)	-0.090 (0.089)	10.13
	<i>V</i>	-0.044 (0.013)	-0.110 (0.068)	9.95
	<i>r</i>	-0.042 (0.012)	-0.107 (0.065)	9.95
	<i>i</i>	-0.046 (0.010)	-0.106 (0.062)	9.95
	<i>Y</i>	-0.039 (0.010)	-0.095 (0.063)	9.96
	<i>J</i>	-0.042 (0.015)	-0.085 (0.075)	10.02
	<i>H</i>	-0.032 (0.015)	-0.052 (0.078)	10.11
CSP-I & II	<i>u</i>	-0.075 (0.020)	-0.132 (0.071)	10.37
	<i>B</i>	-0.037 (0.012)	-0.076 (0.051)	10.18
	<i>g</i>	-0.034 (0.013)	-0.077 (0.062)	10.39
	<i>V</i>	-0.037 (0.012)	-0.076 (0.051)	10.18
	<i>r</i>	-0.035 (0.011)	-0.073 (0.049)	10.18
	<i>i</i>	-0.037 (0.010)	-0.065 (0.048)	10.18
	<i>Y</i>	-0.028 (0.009)	-0.065 (0.050)	10.27
	<i>J</i>	-0.025 (0.013)	-0.038 (0.056)	10.30
	<i>H</i>	-0.015 (0.012)	-0.014 (0.057)	10.34

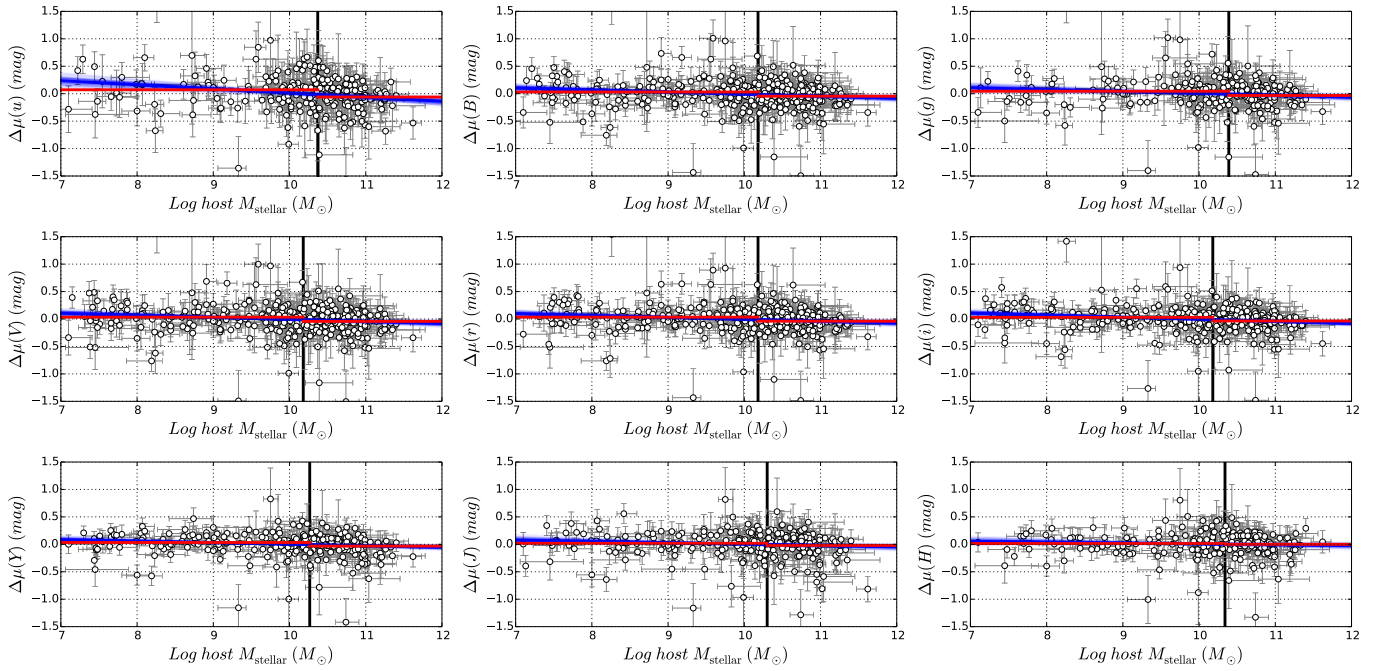


Figure 12. Hubble residuals (Δ_{μ}) as a function of host stellar mass in different bands. The black solid line is the median point of host stellar mass where we split the sample to calculate Δ_{HR} . Red lines are the weighted mean Hubble residuals. Blue thick lines are the best-fit slopes of correlations, and the blue shaded lines are the 1σ dispersion.

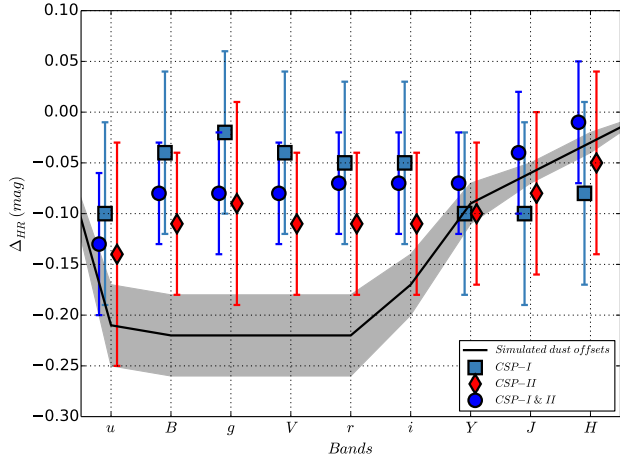


Figure 13. Simulated and observed Hubble residual offsets (Δ_{HR}) as a function of wavelength. This figure is similar to Figure 13 in Uddin et al. (2020), but now including the CSP-II sample. Simulated dust offset calculation is based on Brout & Scolnic (2020). We do not find Δ_{HR} to vary significantly from optical to near-infrared wavelengths. See Uddin et al. (2020) for the construction of the simulated dust offset. See text for discussion.

Table 17. Two sample K-S statistics. In each band, we calculate the D-statistic, sample weighted $c(\alpha)$ for the confidence level (α) at which the condition in Eqn. 8 is met.

Band	K-S Statistics		
	$D_{n,m}$	$c(\alpha) \sqrt{\frac{n+m}{n \times m}}$	α (%)
<i>u</i>	0.188	0.185	89
<i>B</i>	0.102	0.101	40
<i>g</i>	0.168	0.166	84
<i>V</i>	0.109	0.109	51
<i>r</i>	0.095	0.095	30
<i>i</i>	0.126	0.126	69
<i>Y</i>	0.127	0.126	61
<i>J</i>	0.143	0.142	72
<i>H</i>	0.159	0.158	77

Table 16. Dispersion in Hubble residuals (Δ_{μ}) of SNe Ia that are within 10 kpc from their host centers, and those that are beyond 10 kpc in various bands. On average, SNe Ia exploding beyond 10 kpc from host centers have ~ 0.1 mag smaller scatter. SNe Ia are also labeled with respective redshifts.

Band	Dispersion (mag)		
	$< 10 \text{ kpc}$	$> 10 \text{ kpc}$	<i>Difference</i>
<i>u</i>	0.388	0.253	0.135
<i>B</i>	0.312	0.195	0.117
<i>g</i>	0.335	0.197	0.138
<i>V</i>	0.313	0.196	0.118
<i>r</i>	0.295	0.181	0.114
<i>i</i>	0.273	0.171	0.102
<i>Y</i>	0.243	0.179	0.064
<i>J</i>	0.275	0.216	0.060
<i>H</i>	0.251	0.205	0.046

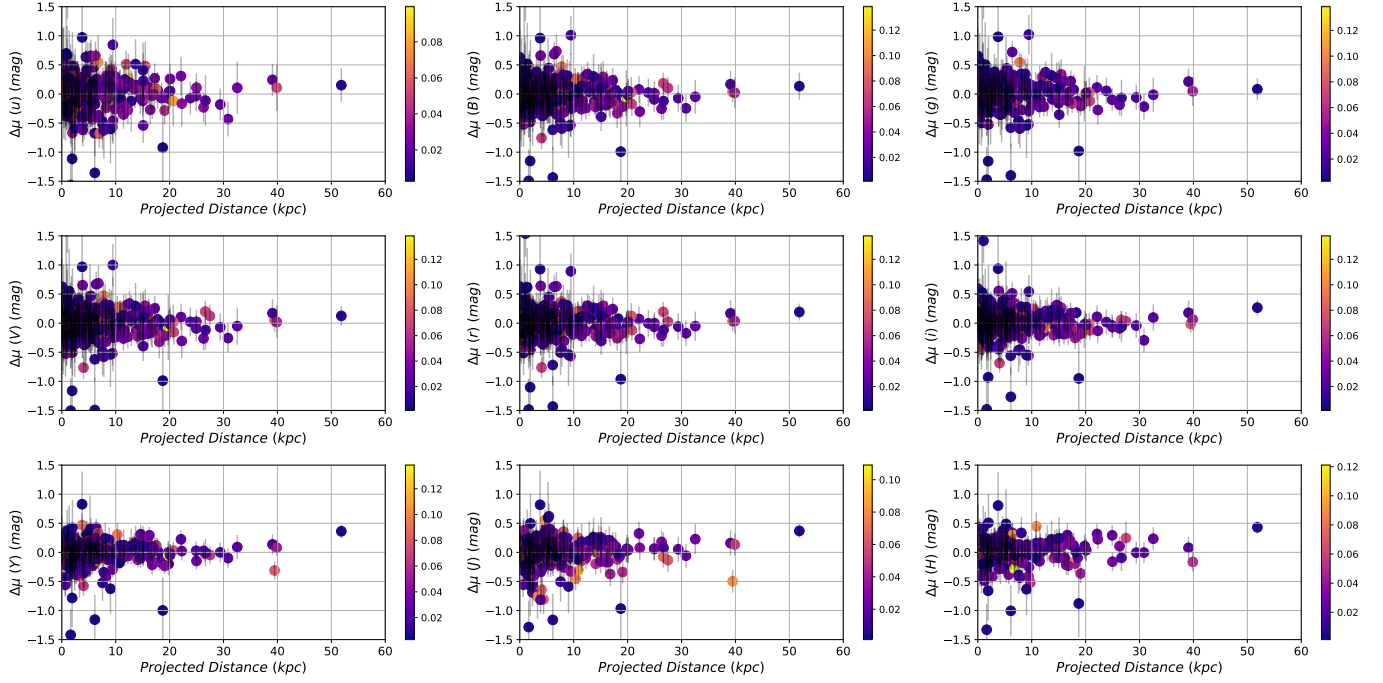


Figure 14. Distribution of $\Delta\mu$ with projected distance from host centers in the $uBgVriYJH$ bands. In all cases, the dispersion of $\Delta\mu$ is smaller for SNe Ia, which explode beyond 10 kpc from their host centers. Color represents redshift.

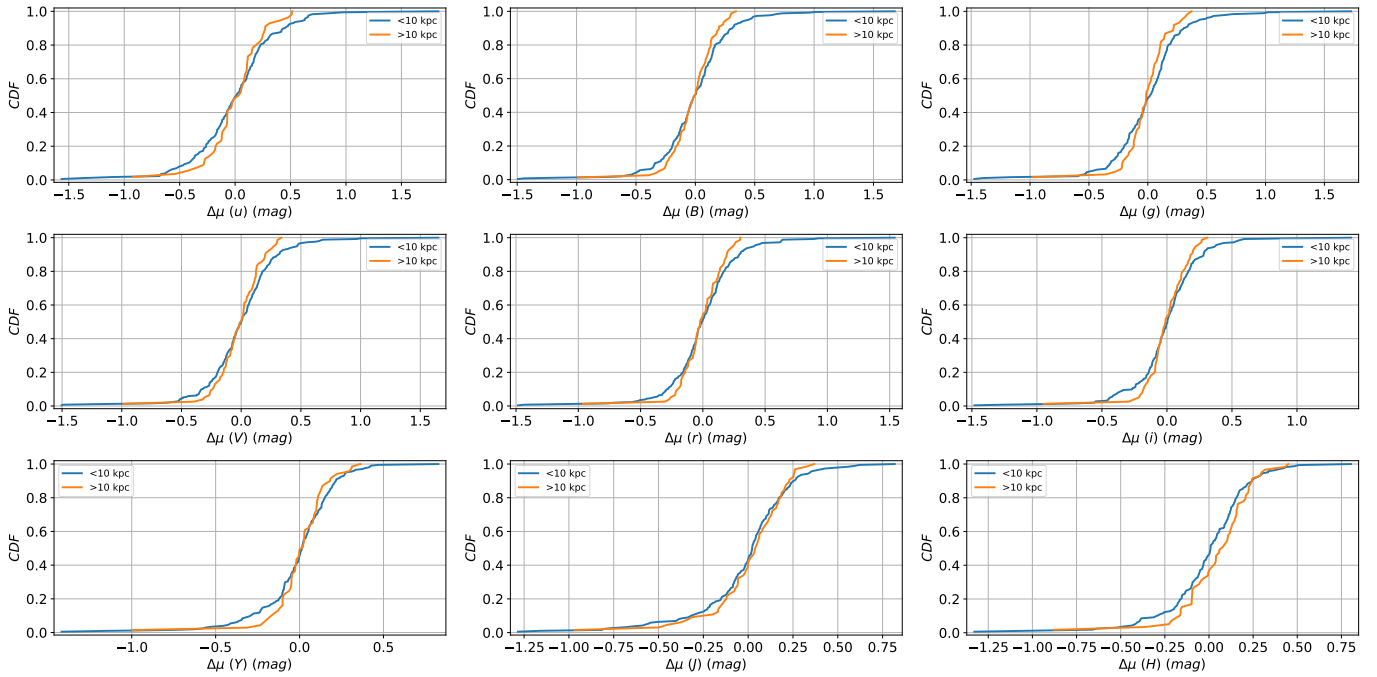


Figure 15. CDFs of Hubble residuals of two samples, shown for all bands. Maximum differences between the distributions can be read from Table 17.

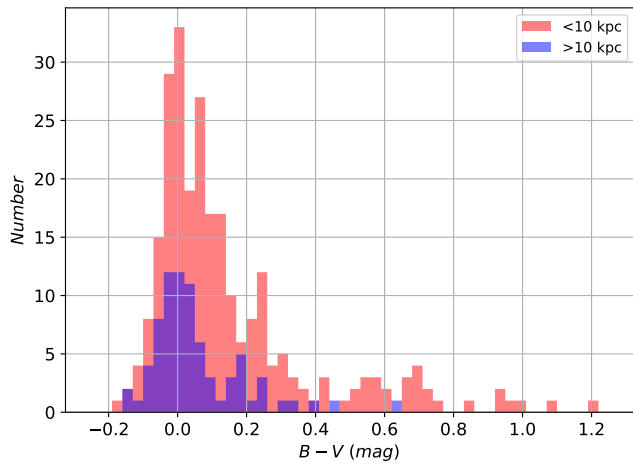


Figure 16. Distributions of SN Ia color for the inner and the outer samples. We see that SNe Ia exploding inside 10 kpc from host centers have a broader ($B - V$) color range compare to those exploding beyond 10 kpc from host centers.

5. CONCLUSION

We have presented an analysis of a combined SNe Ia sample from CSP-I and CSP-II. We calculated the value of the Hubble constant, H_0 , using Cepheid, TRGB, and SBF calibrations applied to this combined sample. Combining all calibration methods, we have derived a global value of Hubble constant as $H_0 = 71.76 \pm 0.58$ (stat) ± 1.19 (sys) $\text{km s}^{-1} \text{Mpc}^{-1}$ from B -band data and $H_0 = 73.22 \pm 0.68$ (stat) ± 1.28 (sys) $\text{km s}^{-1} \text{Mpc}^{-1}$ from H -band data. We have derived systematic errors by assigning equal weights to various calibration methods. We consider these H_0 values to be representative measurements for the current time, given the established disagreements observed in recent H_0 studies.

Using these calibrators separately, although H_0 using the Cepheid and TRGB calibrations are consistent with previous measurements, we found a significant difference in H_0 calculated from two different SBF calibrator compilations. This difference in H_0 may originate from how the SBF distances are measured. In YJH bands, the values of H_0 are larger in the TRGB calibration, and smaller in the SBF calibration in comparison to optical bands ($uBgVri$). Excluding 91T and 91bg-like SNe Ia does not change H_0 significantly, but σ_{int} is reduced. We have found that σ_{int} is the smallest in Y -band, and there is no gradual improvement of σ_{int} from the optical to the near-infrared.

We have revisited the correlation between the luminosity of SNe Ia and their host mass. We did not find any significant correlations from the optical to the NIR, except for u -band, where a $\sim 3\sigma$ negative slope is detected with a $\sim 2\sigma$ difference in Hubble residuals at the median host mass. Dust has been hypothesized as the source of this correlation, but we do not see the corresponding decrease in this correlation with increasing wavelength. Likewise, the progenitor age distribution, that theoretically explains this correlation, predicts a redshift evolution of the mass-step, which is not evident from observed data. We suspect that metallicity may drive this correlation, and therefore, studies should be made in the UV wavelengths where the metallicity effect is more prominent due to increased line opacity.

Finally, we have confirmed our previous findings that SNe Ia exploding more than 10 kpc from their host centers have less scatter in their Hubble residuals than those closer to their host centers. While the exact reason for this finding is unknown, dust may play a role, since we find a reduction of the differences in scatter from optical to near-infrared wavelengths.

ACKNOWLEDGMENTS

We thank Adam Riess for providing feedback on this paper and for discussion on the combined analysis and peculiar velocity correction. We also thank Nandita Khetan for useful discussions on the SBF calibration. The work of the *Carnegie Supernova Project* has been supported by the National Science Foundation (NSF) under grants AST0306969, AST0607438, AST1008343, AST1613426, AST1613472, AST613455., and also by the Danish Agency for Science and Technology and Innovation through a Sapere Aude Level 2 grant (PI Stritzinger). S. U. acknowledges financial support from the Distinguished Professor Chair funds of N. Suntzeff. N. B. S. and K. K. gratefully acknowledge the support from the George P. and Cynthia Woods Mitchell Institute for Fundamental Physics and Astronomy. We also thank the Mitchell Foundation for their support of the Cooks Branch Workshop on Supernovae. M. S. acknowledges grants from the Villum FONDEN No. 24349 and the Independent Research Fund Denmark (IRFD No. 8021-00170B). C. G. acknowledges support from research grant by the VILLUM FONDEN No. 25501. L. G. acknowledges financial support from the Spanish Ministerio de Ciencia e Innovación (MCIN), the Agencia Estatal de Investigación (AEI) 10.13039/501100011033, and the European Social Fund (ESF) "Investing in your future" under the 2019 Ramón y Cajal program RYC2019-027683-I and the PID2020-115253GA-I00 HOSTFLOWS project, from Centro Superior de Investigaciones Científicas (CSIC) under the PIE project 20215AT016, and the program Unidad de Excelencia María de Maeztu CEX2020-001058-M. B. J. S. is supported by NSF grants AST-1920392 and AST-1911074. We acknowledge the Las Campanas Observatory for the outstanding support during our observing runs, and to the Carnegie Observatories Time Allocation Committee for generous time allocations.

Table A1. Description of various columns used to present data.

Parameter	Description
<i>Name</i>	SN Ia name
<i>Host</i>	Host galaxy name
z_{cmb}	CMB redshift
z_{hel}	Heliocentric redshift
B_{max}	Peak B -band magnitude
eB_{max}	Error in B_{max}
s_{BV}	Color-stretch parameter
es_{BV}	Error in s_{BV}
$(B - V)$	$(B - V)$ color
$e(B - V)$	Error in $(B - V)$
$cov(B_{max}, s_{BV})$	Covariance between B_{max} and s_{BV}
$cov(B_{max}, B - V)$	Covariance between B_{max} and $B - V$
$\log(M_*)$	Host galaxy stellar mass in unit of M_\odot
<i>Sample</i>	CSP-I or CSP-II (for Table A2)
<i>Subtype</i>	Ia, 91T, or 91bg (for Table A2)
μ	Distance modulus from calibrators (for Tables A3, A4, A5, and A6)
$e\mu$	Error in μ (for Tables A3, A4, A5, and A6)

APPENDIX

A. DATA

In this section, we present data used in this study. First, we present data for CSP SNe Ia in the B -band. Data for all other bands are available online¹⁸. We also present similar tables for various calibrators. A description of various columns are given in Table A1.

¹⁸ <https://github.com/syeduddin/h0csp>

Table A2. CSP SN Ia light-curve fitting with SNooPy and host galaxy stellar mass. This is a partial table. Full version for various bands are available in github page.

<i>Name</i>	<i>Host</i>	z_{cmb}	z_{hel}	B_{max} (mag)	eB_{max} (mag)	s_{BV}	$e s_{BV}$	$(B - V)$ (mag)	$\epsilon(B - V)$ (mag)	$cov(B_{max}, s_{BV})$	$cov(B_{max}, B - V)$	$\log(M_*)$ (M_{\odot})	<i>Sample</i>	<i>Subtype</i>
ASAS14ad	KUG 1237+183	0.0274	0.0264	16.244	0.005	1.01	0.018	-0.011	0.01118	1e-05	-2e-05	8.61	CSPII	Ia
ASAS14hp	2MASX J21303015-7038489	0.0387	0.03889	16.547	0.003	1.074	0.01	-0.049	0.005	-1e-05	-1e-05	9.09	CSPII	Ia
ASAS14hr	2MASX J01504127-1431032	0.0327	0.0336	17.021	0.009	0.802	0.01	0.061	0.01345	4e-05	-8e-05	10.34	CSPII	Ia
ASAS14hu	ESO 058- G 012	0.0219	0.02159	15.431	0.004	1.052	0.007	-0.045	0.0064	-1e-05	-2e-05	9.93	CSPII	Ia
ASAS14jc	2MASX J07353554-6246099	0.0118	0.01132	15.245	0.006	0.915	0.005	0.437	0.01	1e-05	-4e-05	9.46	CSPII	Ia
ASAS14jg	2MASX J23331223-6034201	0.0143	0.01482	14.732	0.035	1.285	0.022	0.049	0.05941	-2e-05	-0.00122	8.76	CSPII	Ia
ASAS14jz	GALEXASC J184443.33-524819.2	0.0156	0.01579	14.663	0.004	0.989	0.006	-0.041	0.00566	1e-05	-2e-05	8.23	CSPII	Ia
ASAS14kd	2MASX J22532475+0447583	0.0231	0.0243	16.01	0.005	1.169	0.007	0.234	0.00707	2e-05	-2e-05	10.14	CSPII	Ia-91IT
ASAS14kq	2MASX J23451480-2947009	0.0326	0.03358	16.612	0.009	1.147	0.011	-0.021	0.01204	6e-05	-8e-05	8.91	CSPII	Ia
ASAS14lo	UGC 06837	0.021	0.01992	15.876	0.036	0.952	0.018	0.127	0.0608	-1e-05	-0.0013	9.69	CSPII	Ia
ASAS14lp	NGC 4666	0.0062	0.0051	11.914	0.004	1.029	0.004	0.243	0.0064	0.0	-2e-05	10.74	CSPII	Ia
ASAS14lq	2MASX J22571481-2058014	0.0251	0.02617	16.013	0.047	0.999	0.024	0.02	0.0794	-5e-05	-0.00221	10.65	CSPII	Ia
ASAS14lt	IC 0299	0.0315	0.03202	16.368	0.01	0.944	0.008	-0.033	0.0164	2e-05	-0.0001	10.64	CSPII	Ia
ASAS14lw	GALEXASC J010647.95-465904.1	0.0203	0.02089	15.602	0.006	1.25	0.007	-0.012	0.00922	2e-05	-4e-05	6.35	CSPII	Ia
ASAS14me	ESO 113- G 047	0.0174	0.0178	15.074	0.004	1.078	0.005	0.007	0.00566	-0.0	-2e-05	9.05	CSPII	Ia
ASAS14mf	GALEXASC J000454.54-322615.3	0.0302	0.03108	16.511	0.007	0.984	0.005	-0.012	0.01063	1e-05	-5e-05	8.93	CSPII	Ia
ASAS14mw	AM 0139-655 NED02	0.0271	0.02739	15.879	0.003	1.063	0.007	-0.034	0.005	-1e-05	-1e-05	10.68	CSPII	Ia
ASAS14my	NGC 3774	0.0217	0.0205	15.553	0.006	0.923	0.005	0.015	0.01	1e-05	-4e-05	10.31	CSPII	Ia
ASAS15aj	NGC 3449	0.012	0.01091	14.577	0.006	0.831	0.007	0.103	0.00922	1e-05	-4e-05	11.2	CSPII	Ia
ASAS15al	GALEXASC J045749.46-213526.3	0.0338	0.03378	16.841	0.036	1.077	0.028	0.055	0.0592	-3e-05	-0.0013	8.07	CSPII	Ia
ASAS15as	SDSS J093916.69+062551.1	0.0298	0.02868	16.179	0.005	1.076	0.014	0.029	0.00781	-2e-05	-2e-05	7.66	CSPII	Ia
ASAS15ba	SDSS J140455.12+085514.0	0.024	0.02312	15.975	0.004	0.967	0.004	0.008	0.0064	0.0	-2e-05	7.99	CSPII	Ia
ASAS15be	GALEXASC J025245.83-341850.6	0.0214	0.02188	15.611	0.005	1.134	0.006	0.019	0.0064	2e-05	-2e-05	7.8	CSPII	Ia
ASAS15bm	LCRS B150313.2-052600	0.0214	0.02079	15.625	0.007	0.991	0.005	0.127	0.0099	1e-05	-5e-05	10.02	CSPII	Ia
ASAS15cb	VCC 1810	0.0411	0.04001	16.953	0.047	1.086	0.053	0.107	0.0794	-5e-05	-0.00221	10.28	CSPII	Ia
ASAS15cd	CGCG 064-017	0.0354	0.03429	16.693	0.006	1.003	0.005	-0.021	0.00922	1e-05	-4e-05	9.95	CSPII	Ia
ASAS15da	2MASX J05235106-2442201	0.0488	0.0487	17.679	0.044	0.853	0.025	-0.132	0.07603	-2e-05	-0.00194	10.4	CSPII	Ia
ASAS15db	NGC 5996	0.0114	0.01099	14.602	0.004	0.955	0.003	0.086	0.0064	0.0	-2e-05	10.11	CSPII	Ia
ASAS15dd	CGCG 107-031	0.0247	0.02436	16.065	0.006	0.849	0.006	-0.007	0.00922	1e-05	-4e-05	10.41	CSPII	Ia
ASAS15eb	ESO 561- G 012	0.0173	0.01647	15.339	0.01	0.821	0.018	-0.129	0.01562	4e-05	-0.0001	10.96	CSPII	Ia
ASAS15fr	2MASX J09202045-0738229	0.0345	0.03341	16.816	0.039	0.905	0.021	-0.133	0.0658	-2e-05	-0.00152	9.98	CSPII	Ia-91IT
ASAS15ga	NGC 4866	0.0077	0.00663	15.068	0.037	0.496	0.03	0.431	0.04958	0.00074	-0.00137	10.38	CSPII	Ia-91bg
ASAS15go	2MASX J06113048-1629085	0.0193	0.01891	15.847	0.004	1.071	0.012	0.224	0.0064	-1e-05	-2e-05	10.18	CSPII	Ia
ASAS15gr	ESO 366- G 015	0.0248	0.02428	15.867	0.004	1.035	0.007	-0.036	0.0064	-0.0	-2e-05	8.94	CSPII	Ia
ASAS15hf	ESO 375- G 041	0.0072	0.00617	13.996	0.006	0.943	0.005	0.009	0.01	1e-05	-4e-05	9.56	CSPII	Ia

Table A3. Cepheid calibration SN Ia light-curve fitting with SMOOPy, host galaxy stellar mass, and distance modulus.

<i>Name</i>	<i>Host</i>	<i>z_{cmb}</i>	<i>z_{hel}</i>	<i>B_{max}</i> (mag)	<i>eB_{max}</i> (mag)	<i>s_{BV}</i>	<i>e_{s_{BV}}</i>	<i>(B - V)</i> (mag)	<i>ε(B - V)</i> (mag)	<i>cov(B_{max}, s_{BV})</i>	<i>cov(B_{max}, B - V)</i>	<i>log(M_*)</i> (M _⊙)	<i>μ</i> (mag)	<i>eμ</i> (mag)
SN1981B	N4536	0.0072	0.00603	11.979	0.005	0.941	0.019	0.068	0.00781	1e-05	2e-05	10.47	30.835	0.05
SN1990N	N4639	0.0041	0.003	12.714	0.006	1.1	0.006	0.066	0.00849	1e-05	4e-05	10.14	31.812	0.084
SN1994ae	N3370	0.0051	0.004	13.142	0.005	1.043	0.006	0.06	0.00707	2e-05	2e-05	9.69	32.12	0.051
SN1995al	N3021	0.0059	0.005	13.343	0.01	1.043	0.017	0.138	0.01345	5e-05	0.0001	9.87	32.464	0.158
SN1998aq	N3982	0.0043	0.0037	12.357	0.006	0.968	0.004	-0.104	0.00781	1e-05	4e-05	10.02	31.722	0.071
SN2001el	N1448	0.0037	0.0039	12.822	0.008	0.959	0.005	0.144	0.01	2e-05	6e-05	10.34	31.287	0.037
SN2002fk	N1309	0.0066	0.00712	13.202	0.006	0.977	0.004	-0.091	0.00849	1e-05	4e-05	9.94	32.541	0.059
SN2003du	U9391	0.0067	0.00638	13.478	0.005	1.002	0.004	-0.073	0.0064	1e-05	2e-05	8.6	32.848	0.067
SN2005W	N0691	0.008	0.00888	14.208	0.006	0.938	0.006	0.171	0.00781	1e-05	4e-05	9.9	32.83	0.109
SN2005cf	N5917	0.007	0.00646	13.246	0.008	0.972	0.005	0.005	0.01063	1e-05	6e-05	9.65	32.363	0.12
SN2006D	M1337	0.0096	0.00852	14.194	0.005	0.839	0.003	0.098	0.0064	0.0	2e-05	9.76	32.92	0.123
SN2006bh	N7329	0.0105	0.01084	14.369	0.004	0.828	0.003	-0.01	0.00566	0.0	2e-05	10.43	33.246	0.117
SN2007A	N0105	0.0165	0.01763	15.718	0.008	1.047	0.02	0.201	0.01	8e-05	6e-05	10.57	34.527	0.25
SN2007af	N5584	0.0063	0.00546	13.184	0.005	0.949	0.002	0.065	0.00707	0.0	2e-05	9.82	31.772	0.052
SN2007sr	N4038	0.0067	0.00547	12.794	0.047	0.988	0.017	0.145	0.0586	-1e-05	0.00221	10.05	31.603	0.116
SN2009Y	N5728	0.0101	0.00935	13.992	0.008	1.143	0.01	0.146	0.01204	-0.0	6e-05	10.76	33.094	0.205
SN2009ig	N1015	0.008	0.0088	13.453	0.007	1.061	0.014	0.102	0.00922	2e-05	5e-05	10.35	32.563	0.074
SN2011by	N3972	0.0034	0.00284	12.855	0.007	0.968	0.003	-0.006	0.00922	1e-05	5e-05	9.47	31.635	0.089
SN2011fe	M101	0.0012	0.0008	10.004	0.006	0.97	0.002	0.008	0.00721	0.0	4e-05	10.23	29.178	0.041
SN2012cg	N4424	0.0026	0.00146	11.996	0.008	1.013	0.007	0.071	0.00943	3e-05	6e-05	9.7	30.844	0.128
SN2012fr	N1365	0.0051	0.00545	11.935	0.005	1.109	0.004	0.013	0.00583	0.0	2e-05	11.25	31.378	0.056
SN2012ht	N3447	0.0047	0.00356	13.003	0.007	0.868	0.003	-0.016	0.0099	1e-05	5e-05	8.06	31.936	0.034
SN2013aa	N5643	0.0047	0.004	11.098	0.004	1.002	0.002	-0.078	0.005	0.0	2e-05	9.99	30.546	0.052
SN2013dy	N7250	0.0029	0.00389	12.747	0.004	1.091	0.007	0.209	0.005	0.0	2e-05	9.09	31.628	0.125
SN2015F	N2442	0.0053	0.00489	12.753	0.006	0.887	0.003	0.058	0.00721	1e-05	4e-05	10.97	31.45	0.064

Table A4. TRGB calibration SN Ia light-curve fitting with SNIIPy, host galaxy stellar mass, and distance modulus.

<i>Name</i>	<i>Host</i>	z_{cmb}	z_{hel}	B_{max} (mag)	eB_{max} (mag)	s_{BV}	$e s_{BV}$	$(B - V)$ (mag)	$\epsilon(B - V)$ (mag)	$cov(B_{max}, s_{BV})$	$cov(B_{max}, B - V)$	M_* (M_{\odot})	μ (mag)	$e\mu$ (mag)
SN1980N	N1316	0.0055	0.00587	12.458	0.009	0.904	0.006	0.07	0.01204	0.0	8e-05	11.79	31.465	0.04
SN1981B	N4536	0.0072	0.00603	11.979	0.005	0.941	0.019	0.068	0.00781	1e-05	2e-05	10.47	30.969	0.05
SN1981D	N1316	0.0055	0.00587	12.554	0.034	0.793	0.033	0.173	0.03847	0.00017	0.00116	11.79	31.465	0.04
SN1989B	N3627	0.0036	0.00242	12.311	0.01	0.888	0.024	0.364	0.01166	-1e-05	0.0001	11.02	30.226	0.04
SN1994D	N4526	0.0026	0.00149	11.84	0.006	0.824	0.005	-0.047	0.00849	1e-05	4e-05	11.0	31.003	0.07
SN1994ae	N3370	0.0051	0.004	13.142	0.005	1.043	0.006	0.06	0.00707	2e-05	2e-05	9.69	32.278	0.05
SN1995al	N3021	0.0059	0.005	13.343	0.01	1.043	0.017	0.138	0.01345	5e-05	0.0001	9.87	32.226	0.04
SN1998bu	N3368	0.0037	0.00248	12.066	0.006	0.971	0.004	0.345	0.00721	0.0	4e-05	11.26	30.318	0.04
SN2001el	N1448	0.0037	0.0039	12.822	0.008	0.959	0.005	0.144	0.01	2e-05	6e-05	10.69	31.325	0.06
SN2002fk	N1309	0.0066	0.00712	13.202	0.006	0.977	0.004	-0.091	0.00849	1e-05	4e-05	9.94	32.504	0.07
SN2006dd	N1316	0.0055	0.00587	12.228	0.005	0.951	0.003	-0.088	0.00707	1e-05	2e-05	11.79	31.465	0.04
SN2007af	N5584	0.0063	0.00546	13.184	0.005	0.949	0.002	0.065	0.00707	0.0	2e-05	9.82	31.827	0.1
SN2007on	N1404	0.0062	0.00649	13.032	0.009	0.588	0.003	0.116	0.01204	1e-05	8e-05	11.04	31.36	0.06
SN2007sr	N4038	0.0067	0.00547	12.794	0.047	0.988	0.017	0.145	0.0586	-1e-05	0.00221	10.05	31.686	0.05
SN2011fe	M101	0.0012	0.0008	10.004	0.006	0.97	0.002	0.008	0.00721	0.0	4e-05	10.23	29.083	0.04
SN2011iv	N1404	0.0062	0.00649	12.463	0.008	0.699	0.007	0.031	0.01063	1e-05	6e-05	11.04	31.36	0.06
SN2012cg	N4424	0.0026	0.00146	11.996	0.008	1.013	0.007	0.071	0.00943	3e-05	6e-05	9.7	31.005	0.06
SN2012fr	N1365	0.0051	0.00545	11.935	0.005	1.109	0.004	0.013	0.00583	0.0	2e-05	11.25	31.365	0.06
SN2013aa	N5643	0.0047	0.004	11.098	0.004	1.002	0.002	-0.078	0.005	0.0	2e-05	9.99	30.48	0.08
SN2017cbv	N5643	0.0047	0.004	11.124	0.007	1.115	0.006	0.018	0.00922	0.0	5e-05	9.99	30.48	0.08

Table A5. SBF calibration (Jensen et al. 2021) SN Ia light-curve fitting with SNooPy, host galaxy stellar mass, and distance modulus.

<i>Name</i>	<i>z_{cmb}</i>	<i>z_{hel}</i>	<i>B_{max}</i> (mag)	<i>eB_{max}</i> (mag)	<i>s_{BV}</i>	<i>es_{BV}</i>	<i>(B - V)</i> (mag)	<i>e(B - V)</i> (mag)	<i>cov(B_{max}, s_{BV})</i>	<i>cov(B_{max}, B - V)</i>	<i>log M_*</i> (<i>M_⊙</i>)	<i>μ</i> (mag)	<i>eμ</i> (mag)	
CSP15aae	N5490	0.017	0.01618	16.762	0.008	0.505	0.004	0.454	0.01063	0.0	6e-05	11.14	34.267	0.08
PTF13ebh	N0890	0.0125	0.01326	15.043	0.007	0.636	0.004	0.123	0.00922	1e-05	5e-05	10.86	33.296	0.081
SN1970J	N7619	0.012	0.0132	14.278	0.084	0.704	0.071	-0.144	0.12458	0.0039	0.00706	11.34	33.341	0.081
SN1995D	N2962	0.0077	0.00656	13.265	0.008	1.171	0.009	-0.053	0.01	-2e-05	6e-05	10.597	32.532	0.084
SN1997E	N2258	0.0135	0.01354	15.192	0.007	0.831	0.011	0.045	0.00922	3e-05	5e-05	11.199	33.781	0.094
SN1999ej	N0495	0.0128	0.01372	15.435	0.005	0.78	0.022	0.017	0.0064	1e-05	2e-05	10.99	34.049	0.081
SN2000cx	N0524	0.0069	0.00793	13.122	0.006	0.842	0.005	0.053	0.00781	1e-05	4e-05	10.929	32.212	0.09
SN2002cs	N6702	0.0153	0.01577	15.202	0.013	1.196	0.013	0.037	0.01703	8e-05	0.00017	11.324	33.992	0.087
SN2002ha	N6964	0.0131	0.01405	14.743	0.005	0.833	0.005	-0.065	0.00707	1e-05	2e-05	11.021	33.685	0.096
SN2003hv	N1201	0.0051	0.0056	12.447	0.049	0.788	0.019	-0.08	0.0608	-1e-05	0.0024	10.565	31.347	0.074
SN2006ef	N0809	0.017	0.01787	15.438	0.067	0.857	0.02	-0.024	0.08071	-4e-05	0.00449	10.35	34.376	0.109
SN2007cv	IC2597	0.0087	0.0076	15.06	0.012	0.711	0.01	0.017	0.01697	7e-05	0.00014	11.478	33.673	0.082
SN2008L	N1259	0.0189	0.0194	15.273	0.019	0.771	0.016	-0.063	0.02484	0.00015	0.00036	10.888	34.365	0.105
SN2008R	N1200	0.0129	0.01349	15.27	0.008	0.633	0.006	0.12	0.01063	0.0	6e-05	11.25	33.66	0.08
SN2008hs	N0910	0.0166	0.01735	16.031	0.02	0.611	0.006	0.075	0.02441	3e-05	0.0004	11.504	34.459	0.093
SN2008hv	N2765	0.0136	0.01254	14.741	0.009	0.869	0.004	-0.046	0.0114	1e-05	8e-05	10.55	33.725	0.083
SN2008ia	ESO125-G006	0.0225	0.02198	15.881	0.011	0.836	0.006	-0.035	0.01556	1e-05	0.00012	10.77	34.896	0.195
SN2010Y	N8392	0.0113	0.0109	15.005	0.013	0.658	0.006	0.022	0.0164	2e-05	0.00017	10.58	33.861	0.088
SN2014bv	N4386	0.0057	0.00559	14.007	0.018	0.621	0.015	0.214	0.0222	-9e-05	0.00032	10.48	32.427	0.08
SN2015bp	N5839	0.0047	0.00407	13.775	0.01	0.703	0.006	0.082	0.01281	3e-05	0.0001	9.979	32.369	0.078
SN2016ajf	N1278	0.0198	0.0203	16.922	0.05	0.488	0.015	0.556	0.07507	0.00011	0.0025	11.436	34.202	0.106
SN2019ein	N5353	0.0084	0.00776	14.178	0.018	0.863	0.01	-0.014	0.0222	0.00011	0.00032	11.484	32.711	0.076

Table A6. SBF calibration (Khetan et al. 2021) SN Ia light-curve fitting with SMOoPy, host galaxy stellar mass, and distance modulus.

<i>Name</i>	<i>Host</i>	z_{cmb}	z_{hel}	B_{max} (mag)	eB_{max} (mag)	s_{BV}	es_{BV}	$(B - V)$ (mag)	$\epsilon(B - V)$ (mag)	$cov(B_{max}, s_{BV})$	$cov(B_{max}, B - V)$	$\log M_*$ (M_{\odot})	μ (mag)	$e\mu$ (mag)
SN1970J	N7619	0.012	0.0132	14.278	0.084	0.704	0.071	-0.144	0.12458	0.0039	0.00706	11.34	33.341	0.081
SN1980N	N1316	0.0055	0.00587	12.458	0.009	0.904	0.006	0.07	0.01204	0.0	8e-05	11.514	31.59	0.05
SN1981D	N1316	0.0055	0.00587	12.554	0.034	0.793	0.033	0.173	0.03847	0.00017	0.00116	11.514	31.59	0.05
SN1983G	N4753	0.0032	0.00206	12.863	0.081	1.005	0.037	0.188	0.08538	-0.00015	0.00656	11.148	31.92	0.197
SN1992A	N1380	0.0059	0.00626	12.539	0.006	0.787	0.008	0.039	0.00721	2e-05	4e-05	10.931	31.632	0.075
SN1992bo	E352-057	0.0177	0.01851	15.787	0.009	0.744	0.008	-0.01	0.0114	3e-05	8e-05	10.395	34.27	0.15
SN1994D	N4526	0.0026	0.00149	11.84	0.006	0.824	0.005	-0.047	0.00849	1e-05	4e-05	10.996	31.32	0.12
SN1995D	N2962	0.0077	0.00656	13.265	0.008	1.171	0.009	-0.053	0.01	-2e-05	6e-05	10.597	32.532	0.084
SN1996X	N5061	0.0079	0.00689	13.075	0.016	0.917	0.013	-0.033	0.01887	6e-05	0.00026	11.057	32.26	0.19
SN1997E	N2258	0.0135	0.01354	15.192	0.007	0.831	0.011	0.045	0.00922	3e-05	5e-05	11.199	33.781	0.094
SN1998bp	N6495	0.0102	0.01043	15.384	0.01	0.549	0.009	0.265	0.01281	1e-05	0.0001	10.462	33.1	0.15
SN2000cx	N0524	0.0069	0.00793	13.122	0.006	0.842	0.005	0.053	0.00781	1e-05	4e-05	10.929	32.21	0.09
SN2003hv	N1201	0.0051	0.0056	12.447	0.049	0.788	0.019	-0.08	0.0608	-1e-05	0.0024	10.565	31.347	0.074
SN2006dd	N1316	0.0055	0.00587	12.228	0.005	0.951	0.003	-0.088	0.00707	1e-05	2e-05	11.514	31.59	0.05
SN2007on	N1404	0.0062	0.00649	13.032	0.009	0.588	0.003	0.116	0.01204	1e-05	8e-05	10.932	31.526	0.072
SN2008Q	N524	0.0069	0.00793	13.471	0.013	0.791	0.023	-0.04	0.01703	0.00016	0.00017	10.929	31.922	0.212
SN2011iv	N1404	0.0062	0.00649	12.463	0.008	0.699	0.007	0.031	0.01063	1e-05	6e-05	10.932	31.526	0.072
SN2012cg	N4424	0.0026	0.00146	11.996	0.008	1.013	0.007	0.071	0.00943	3e-05	6e-05	9.706	31.02	0.18
SN2014bv	N4386	0.0057	0.00559	14.007	0.018	0.621	0.015	0.214	0.0222	-9e-05	0.00032	10.48	32.427	0.08
SN2015bp	N5839	0.0047	0.00407	13.775	0.01	0.703	0.006	0.082	0.01281	3e-05	0.0001	9.979	32.369	0.078
SN2016coj	N4125	0.0048	0.00448	13.099	0.009	0.807	0.009	0.0	0.01273	3e-05	8e-05	11.083	31.922	0.258
SN2017fgc	N0474	0.0067	0.00772	14.021	0.014	1.17	0.013	0.378	0.01664	-1e-05	0.0002	10.568	32.536	0.133
SN2018aoz	N3923	0.0069	0.0058	12.746	0.009	0.875	0.005	0.012	0.01082	2e-05	8e-05	11.204	31.795	0.101
SN2020ne	N4636	0.0043	0.00313	11.983	0.01	0.714	0.011	-0.089	0.01281	6e-05	0.0001	10.803	30.83	0.13

REFERENCES

- Addison, G. E. 2021, *ApJL*, 912, L1,
doi: [10.3847/2041-8213/abf56e](https://doi.org/10.3847/2041-8213/abf56e)
- Arnett, W. D., Branch, D., & Wheeler, J. C. 1985, *Nature*, 314, 337, doi: [10.1038/314337a0](https://doi.org/10.1038/314337a0)
- Ashall, C., Lu, J., Hsiao, E. Y., et al. 2021, *ApJ*, 922, 205,
doi: [10.3847/1538-4357/ac19ac](https://doi.org/10.3847/1538-4357/ac19ac)
- Avelino, A., Friedman, A. S., Mandel, K. S., et al. 2019,
ApJ, 887, 106, doi: [10.3847/1538-4357/ab2a16](https://doi.org/10.3847/1538-4357/ab2a16)
- Baltay, C., Rabinowitz, D., Hadjijska, E., et al. 2013,
PASP, 125, 683, doi: [10.1086/671198](https://doi.org/10.1086/671198)
- Barone-Nugent, R. L., Lidman, C., Wyithe, J. S. B., et al. 2012, *MNRAS*, 425, 1007,
doi: [10.1111/j.1365-2966.2012.21412.x](https://doi.org/10.1111/j.1365-2966.2012.21412.x)
- Bernal, J. L., Verde, L., Jimenez, R., et al. 2021, *PhRvD*, 103, 103533, doi: [10.1103/PhysRevD.103.103533](https://doi.org/10.1103/PhysRevD.103.103533)
- Betoule, M., Kessler, R., Guy, J., et al. 2014, *A&A*, 568, A22, doi: [10.1051/0004-6361/201423413](https://doi.org/10.1051/0004-6361/201423413)
- Blakeslee, J. P., Jensen, J. B., Ma, C.-P., Milne, P. A., & Greene, J. E. 2021, *ApJ*, 911, 65,
doi: [10.3847/1538-4357/abe86a](https://doi.org/10.3847/1538-4357/abe86a)
- Boone, K., Aldering, G., Antilogus, P., et al. 2021, *ApJ*, 912, 71, doi: [10.3847/1538-4357/abec3b](https://doi.org/10.3847/1538-4357/abec3b)
- Branch, D., & Miller, D. L. 1993, *ApJL*, 405, L5,
doi: [10.1086/186752](https://doi.org/10.1086/186752)
- Branch, D., & Patchett, B. 1973, *MNRAS*, 161, 71,
doi: [10.1093/mnras/161.1.71](https://doi.org/10.1093/mnras/161.1.71)
- Brout, D., & Scolnic, D. 2020, arXiv e-prints,
arXiv:2004.10206. <https://arxiv.org/abs/2004.10206>
- Brown, P. J., & Crumpler, N. R. 2020, *ApJ*, 890, 45,
doi: [10.3847/1538-4357/ab66b3](https://doi.org/10.3847/1538-4357/ab66b3)
- Brown, P. J., Kuin, P., Scalzo, R., et al. 2014, *ApJ*, 787, 29,
doi: [10.1088/0004-637X/787/1/29](https://doi.org/10.1088/0004-637X/787/1/29)
- Burns, C. R., Stritzinger, M., Phillips, M. M., et al. 2011,
AJ, 141, 19, doi: [10.1088/0004-6256/141/1/19](https://doi.org/10.1088/0004-6256/141/1/19)
- . 2014, *ApJ*, 789, 32, doi: [10.1088/0004-637X/789/1/32](https://doi.org/10.1088/0004-637X/789/1/32)
- Burns, C. R., Parent, E., Phillips, M. M., et al. 2018, *ApJ*, 869, 56, doi: [10.3847/1538-4357/aae51c](https://doi.org/10.3847/1538-4357/aae51c)
- Cadonau, R., Sandage, A., & Tammann, G. A. 1985, in
Supernovae as Distance Indicators, ed. N. Bartel, Vol. 224, 151, doi: [10.1007/3-540-15206-7_56](https://doi.org/10.1007/3-540-15206-7_56)
- Carrick, J., Turnbull, S. J., Lavaux, G., & Hudson, M. J. 2015, *MNRAS*, 450, 317, doi: [10.1093/mnras/stv547](https://doi.org/10.1093/mnras/stv547)
- Childress, M., Aldering, G., Antilogus, P., et al. 2013, *ApJ*, 770, 107, doi: [10.1088/0004-637X/770/2/107](https://doi.org/10.1088/0004-637X/770/2/107)
- Childress, M. J., Wolf, C., & Zahid, H. J. 2014, *MNRAS*, 445, 1898, doi: [10.1093/mnras/stu1892](https://doi.org/10.1093/mnras/stu1892)
- Contreras, C., Hamuy, M., Phillips, M. M., et al. 2010, *AJ*, 139, 519, doi: [10.1088/0004-6256/139/2/519](https://doi.org/10.1088/0004-6256/139/2/519)
- de Sitter, W. 1916a, *MNRAS*, 76, 699,
doi: [10.1093/mnras/76.9.699](https://doi.org/10.1093/mnras/76.9.699)
- . 1916b, *MNRAS*, 77, 155, doi: [10.1093/mnras/77.2.155](https://doi.org/10.1093/mnras/77.2.155)
- Dhawan, S., Brout, D., Scolnic, D., et al. 2020, *ApJ*, 894, 54, doi: [10.3847/1538-4357/ab7fb0](https://doi.org/10.3847/1538-4357/ab7fb0)
- Djorgovski, S. G., Drake, A. J., Mahabal, A. A., et al. 2011,
The Catalina Real-Time Transient Survey (CRTS).
<https://arxiv.org/abs/1102.5004>
- Einstein, A. 1915, *Sitzungsberichte der Königlich Preußischen Akademie der Wissenschaften (Berlin)*, Seite 831-839., 831
- Ferrarese, L., Mould, J. R., Kennicutt, Robert C., J., et al. 2000, *ApJ*, 529, 745, doi: [10.1086/308309](https://doi.org/10.1086/308309)
- Filippenko, A. V., Richmond, M. W., Matheson, T., et al. 1992a, *ApJL*, 384, L15, doi: [10.1086/186252](https://doi.org/10.1086/186252)
- Filippenko, A. V., Richmond, M. W., Branch, D., et al. 1992b, *AJ*, 104, 1543, doi: [10.1086/116339](https://doi.org/10.1086/116339)
- Folatelli, G., Morrell, N., Phillips, M. M., et al. 2013, *ApJ*, 773, 53, doi: [10.1088/0004-637X/773/1/53](https://doi.org/10.1088/0004-637X/773/1/53)
- Foreman-Mackey, D., Hogg, D. W., Lang, D., & Goodman, J. 2013, *PASP*, 125, 306, doi: [10.1086/670067](https://doi.org/10.1086/670067)
- Freedman, W. L. 2021, *ApJ*, 919, 16,
doi: [10.3847/1538-4357/ac0e95](https://doi.org/10.3847/1538-4357/ac0e95)
- Freedman, W. L., Madore, B. F., Gibson, B. K., et al. 2001,
ApJ, 553, 47, doi: [10.1086/320638](https://doi.org/10.1086/320638)
- Freedman, W. L., Madore, B. F., Hatt, D., et al. 2019, *ApJ*, 882, 34, doi: [10.3847/1538-4357/ab2f73](https://doi.org/10.3847/1538-4357/ab2f73)
- Friedmann, A. 1922, *Zeitschrift fur Physik*, 10, 377,
doi: [10.1007/BF01332580](https://doi.org/10.1007/BF01332580)
- Fukugita, M., & Hogan, C. J. 1991, *ApJL*, 368, L11,
doi: [10.1086/185936](https://doi.org/10.1086/185936)
- Galbany, L., de Jaeger, T., Riess, A., et al. 2022, arXiv e-prints, arXiv:2209.02546,
doi: [10.48550/arXiv.2209.02546](https://doi.org/10.48550/arXiv.2209.02546)
- Garnavich, P., Wood, C. M., Milne, P., et al. 2022, arXiv e-prints, arXiv:2204.12060.
<https://arxiv.org/abs/2204.12060>
- Gelman, A., Roberts, G. O., & Gilks, W. 1996, *Bayesian Statistics* 5, 599
- Goobar, A., & Leibundgut, B. 2011, *Annual Review of Nuclear and Particle Science*, 61, 251,
doi: [10.1146/annurev-nucl-102010-130434](https://doi.org/10.1146/annurev-nucl-102010-130434)
- Goodman, J., & Weare, J. 2010, *Communications in Applied Mathematics and Computational Science*, 5, 65,
doi: [10.2140/camcos.2010.5.65](https://doi.org/10.2140/camcos.2010.5.65)
- Hamuy, M., Cartier, R., Contreras, C., & Suntzeff, N. B. 2021, *MNRAS*, 500, 1095, doi: [10.1093/mnras/staa3350](https://doi.org/10.1093/mnras/staa3350)
- Hamuy, M., Phillips, M. M., Maza, J., et al. 1995, *AJ*, 109, 1, doi: [10.1086/117251](https://doi.org/10.1086/117251)

- Hamuy, M., Phillips, M. M., Suntzeff, N. B., et al. 1996, *AJ*, 112, 2398, doi: [10.1086/118191](https://doi.org/10.1086/118191)
- Hamuy, M., Folatelli, G., Morrell, N. I., et al. 2006, *PASP*, 118, 2, doi: [10.1086/500228](https://doi.org/10.1086/500228)
- Hoeflich, P., & Khokhlov, A. 1996, *ApJ*, 457, 500, doi: [10.1086/176748](https://doi.org/10.1086/176748)
- Holz, D. E., & Hughes, S. A. 2005, *ApJ*, 629, 15, doi: [10.1086/431341](https://doi.org/10.1086/431341)
- Hoyt, T. J., Beaton, R. L., Freedman, W. L., et al. 2021, *ApJ*, 915, 34, doi: [10.3847/1538-4357/abfe5a](https://doi.org/10.3847/1538-4357/abfe5a)
- Hsiao, E. Y., Conley, A., Howell, D. A., et al. 2007, *ApJ*, 663, 1187, doi: [10.1086/518232](https://doi.org/10.1086/518232)
- Hsiao, E. Y., Phillips, M. M., Marion, G. H., et al. 2019, *PASP*, 131, 014002, doi: [10.1088/1538-3873/aae961](https://doi.org/10.1088/1538-3873/aae961)
- Hsiao, E. Y., Hoeflich, P., Ashall, C., et al. 2020, *ApJ*, 900, 140, doi: [10.3847/1538-4357/abaf4c](https://doi.org/10.3847/1538-4357/abaf4c)
- Hubble, E. 1929, *Proceedings of the National Academy of Science*, 15, 168, doi: [10.1073/pnas.15.3.168](https://doi.org/10.1073/pnas.15.3.168)
- Hubble, E., & Humason, M. L. 1931, *ApJ*, 74, 43, doi: [10.1086/143323](https://doi.org/10.1086/143323)
- Hubble, E. P. 1926, *ApJ*, 64, 321, doi: [10.1086/143018](https://doi.org/10.1086/143018)
- Humason, M. L., Mayall, N. U., & Sandage, A. R. 1956, *AJ*, 61, 97, doi: [10.1086/107297](https://doi.org/10.1086/107297)
- Jacoby, G. H., Branch, D., Ciardullo, R., et al. 1992, *PASP*, 104, 599, doi: [10.1086/133035](https://doi.org/10.1086/133035)
- Jensen, J. B., Blakeslee, J. P., Ma, C.-P., et al. 2021, *ApJS*, 255, 21, doi: [10.3847/1538-4365/ac01e7](https://doi.org/10.3847/1538-4365/ac01e7)
- Johansson, J., Cenko, S. B., Fox, O. D., et al. 2021, *ApJ*, 923, 237, doi: [10.3847/1538-4357/ac2f9e](https://doi.org/10.3847/1538-4357/ac2f9e)
- Kelly, B. C. 2007, *ApJ*, 665, 1489, doi: [10.1086/519947](https://doi.org/10.1086/519947)
- Khetan, N., Izzo, L., Branchesi, M., et al. 2021, *A&A*, 647, A72, doi: [10.1051/0004-6361/202039196](https://doi.org/10.1051/0004-6361/202039196)
- Kirshner, R. P., & Kwan, J. 1974, *ApJ*, 193, 27, doi: [10.1086/153123](https://doi.org/10.1086/153123)
- Kowal, C. T. 1968, *AJ*, 73, 1021, doi: [10.1086/110763](https://doi.org/10.1086/110763)
- Kragh, H., & Smith, R. W. 2003, *History of Science*, 41, 141
- Krisciunas, K., Phillips, M. M., & Suntzeff, N. B. 2004, *ApJL*, 602, L81, doi: [10.1086/382731](https://doi.org/10.1086/382731)
- Krisciunas, K., Contreras, C., Burns, C. R., et al. 2017, *AJ*, 154, 211, doi: [10.3847/1538-3881/aa8df0](https://doi.org/10.3847/1538-3881/aa8df0)
- Lampeitl, H., Smith, M., Nichol, R. C., et al. 2010, *ApJ*, 722, 566, doi: [10.1088/0004-637X/722/1/566](https://doi.org/10.1088/0004-637X/722/1/566)
- Le Borgne, D., & Rocca-Volmerange, B. 2002, *A&A*, 386, 446, doi: [10.1051/0004-6361:20020259](https://doi.org/10.1051/0004-6361:20020259)
- Leavitt, H. S., & Pickering, E. C. 1912, *Harvard College Observatory Circular*, 173, 1
- Leibundgut, B., & Sullivan, M. 2018, *SSRv*, 214, 57, doi: [10.1007/s11214-018-0491-8](https://doi.org/10.1007/s11214-018-0491-8)
- Leibundgut, B., Kirshner, R. P., Phillips, M. M., et al. 1993, *AJ*, 105, 301, doi: [10.1086/116427](https://doi.org/10.1086/116427)
- Lemaître, G. 1927, *Annales de la Société Scientifique de Bruxelles*, 47, 49
- Lentz, E. J., Baron, E., Branch, D., Hauschildt, P. H., & Nugent, P. E. 2000, *ApJ*, 530, 966, doi: [10.1086/308400](https://doi.org/10.1086/308400)
- Li, W. D., Filippenko, A. V., Treffers, R. R., et al. 2000, *AIP Conference Proceedings*, 522, 103, doi: [10.1063/1.1291702](https://doi.org/10.1063/1.1291702)
- Lu, J., Ashall, C., Hsiao, E. Y., et al. 2021, *ApJ*, 920, 107, doi: [10.3847/1538-4357/ac1606](https://doi.org/10.3847/1538-4357/ac1606)
- Lu, J., Hsiao, E. Y., Phillips, M. M., et al. 2022, *arXiv e-prints*, arXiv:2211.05998, doi: [10.48550/arXiv.2211.05998](https://doi.org/10.48550/arXiv.2211.05998)
- . 2023, *ApJ*, 948, 27, doi: [10.3847/1538-4357/acc100](https://doi.org/10.3847/1538-4357/acc100)
- Ma, C.-P., Greene, J. E., McConnell, N., et al. 2014, *ApJ*, 795, 158, doi: [10.1088/0004-637X/795/2/158](https://doi.org/10.1088/0004-637X/795/2/158)
- Macaulay, E., Nichol, R. C., Bacon, D., et al. 2019, *MNRAS*, 486, 2184, doi: [10.1093/mnras/stz978](https://doi.org/10.1093/mnras/stz978)
- Madore, B. F., & Freedman, W. L. 1995, *AJ*, 109, 1645, doi: [10.1086/117391](https://doi.org/10.1086/117391)
- Madore, B. F., Freedman, W. L., Hatt, D., et al. 2018, *ApJ*, 858, 11, doi: [10.3847/1538-4357/aab7f4](https://doi.org/10.3847/1538-4357/aab7f4)
- Mould, J., Aaronson, M., & Huchra, J. 1980, *ApJ*, 238, 458, doi: [10.1086/158002](https://doi.org/10.1086/158002)
- Neill, J. D., Sullivan, M., Howell, D. A., et al. 2009, *ApJ*, 707, 1449, doi: [10.1088/0004-637X/707/2/1449](https://doi.org/10.1088/0004-637X/707/2/1449)
- Perlmutter, S., Aldering, G., Goldhaber, G., et al. 1999, *ApJ*, 517, 565, doi: [10.1086/307221](https://doi.org/10.1086/307221)
- Peterson, E. R., Kenworthy, W. D., Scolnic, D., et al. 2022, *ApJ*, 938, 112, doi: [10.3847/1538-4357/ac4698](https://doi.org/10.3847/1538-4357/ac4698)
- Peterson, E. R., Jones, D. O., Scolnic, D., et al. 2023, *MNRAS*, 522, 2478, doi: [10.1093/mnras/stad1077](https://doi.org/10.1093/mnras/stad1077)
- Phillips, M. M. 1993, *ApJL*, 413, L105, doi: [10.1086/186970](https://doi.org/10.1086/186970)
- . 2012, *PASA*, 29, 434, doi: [10.1071/AS11056](https://doi.org/10.1071/AS11056)
- Phillips, M. M., Lira, P., Suntzeff, N. B., et al. 1999, *AJ*, 118, 1766, doi: [10.1086/301032](https://doi.org/10.1086/301032)
- Phillips, M. M., Wells, L. A., Suntzeff, N. B., et al. 1992, *AJ*, 103, 1632, doi: [10.1086/116177](https://doi.org/10.1086/116177)
- Phillips, M. M., Contreras, C., Hsiao, E. Y., et al. 2019, *PASP*, 131, 014001, doi: [10.1088/1538-3873/aae8bd](https://doi.org/10.1088/1538-3873/aae8bd)
- Phillips, M. M., Ashall, C., Burns, C. R., et al. 2022, *ApJ*, 938, 47, doi: [10.3847/1538-4357/ac9305](https://doi.org/10.3847/1538-4357/ac9305)
- Pietrzyński, G., Graczyk, D., Gellenne, A., et al. 2019, *Nature*, 567, 200, doi: [10.1038/s41586-019-0999-4](https://doi.org/10.1038/s41586-019-0999-4)
- Planck Collaboration, Aghanim, N., Akrami, Y., et al. 2018, *arXiv e-prints*, arXiv:1807.06209, <https://arxiv.org/abs/1807.06209>
- Ponder, K. A., Wood-Vasey, W. M., Weyant, A., et al. 2021, *ApJ*, 923, 197, doi: [10.3847/1538-4357/ac2d99](https://doi.org/10.3847/1538-4357/ac2d99)
- Pskovskii, I. P. 1977, *Soviet Ast.*, 21, 675
- Pskovskii, Y. P. 1984, *Soviet Ast.*, 28, 658

- Refsdal, S. 1964, *MNRAS*, 128, 307,
doi: [10.1093/mnras/128.4.307](https://doi.org/10.1093/mnras/128.4.307)
- Reid, M. J., Pesce, D. W., & Riess, A. G. 2019, *ApJL*, 886, L27, doi: [10.3847/2041-8213/ab552d](https://doi.org/10.3847/2041-8213/ab552d)
- Riess, A. G., Casertano, S., Yuan, W., et al. 2021, *ApJL*, 908, L6, doi: [10.3847/2041-8213/abdbaf](https://doi.org/10.3847/2041-8213/abdbaf)
- Riess, A. G., Press, W. H., & Kirshner, R. P. 1995, *ApJL*, 438, L17, doi: [10.1086/187704](https://doi.org/10.1086/187704)
- Riess, A. G., Filippenko, A. V., Challis, P., et al. 1998, *AJ*, 116, 1009, doi: [10.1086/300499](https://doi.org/10.1086/300499)
- Riess, A. G., Macri, L. M., Hoffmann, S. L., et al. 2016, *ApJ*, 826, 56, doi: [10.3847/0004-637X/826/1/56](https://doi.org/10.3847/0004-637X/826/1/56)
- Riess, A. G., Yuan, W., Macri, L. M., et al. 2022, *ApJL*, 934, L7, doi: [10.3847/2041-8213/ac5c5b](https://doi.org/10.3847/2041-8213/ac5c5b)
- Rigault, M., Copin, Y., Aldering, G., et al. 2013, *A&A*, 560, A66, doi: [10.1051/0004-6361/201322104](https://doi.org/10.1051/0004-6361/201322104)
- Robertson, H. P. 1928, *Phil. Mag*, 5, 835,
doi: [10.1080/14786440508564528](https://doi.org/10.1080/14786440508564528)
- Roman, M., Hardin, D., Betoule, M., et al. 2018, *A&A*, 615, A68, doi: [10.1051/0004-6361/201731425](https://doi.org/10.1051/0004-6361/201731425)
- Ruiz-Lapuente, P., Cappellaro, E., Turatto, M., et al. 1992, *ApJL*, 387, L33, doi: [10.1086/186299](https://doi.org/10.1086/186299)
- Rust, B. W. 1974, PhD thesis, Oak Ridge National Laboratory, Tennessee
- Sandage, A. 1958, *ApJ*, 127, 513, doi: [10.1086/146483](https://doi.org/10.1086/146483)
- Sandage, A., & Tammann, G. A. 1974, *ApJ*, 190, 525,
doi: [10.1086/152906](https://doi.org/10.1086/152906)
- . 1982, *ApJ*, 256, 339, doi: [10.1086/159911](https://doi.org/10.1086/159911)
- . 1993, *ApJ*, 415, 1, doi: [10.1086/173137](https://doi.org/10.1086/173137)
- Schlafly, E. F., & Finkbeiner, D. P. 2011, *ApJ*, 737, 103,
doi: [10.1088/0004-637X/737/2/103](https://doi.org/10.1088/0004-637X/737/2/103)
- Shajib, A. J., Birrer, S., Treu, T., et al. 2020, *MNRAS*, 494, 6072, doi: [10.1093/mnras/staa828](https://doi.org/10.1093/mnras/staa828)
- Shappee, B. J., Prieto, J. L., Grupe, D., et al. 2014, *ApJ*, 788, 48, doi: [10.1088/0004-637X/788/1/48](https://doi.org/10.1088/0004-637X/788/1/48)
- Slipher, V. M. 1915, *Popular Astronomy*, 23, 21
- . 1917, *Proceedings of the American Philosophical Society*, 56, 403
- Stritzinger, M. D., Phillips, M. M., Boldt, L. N., et al. 2011, *AJ*, 142, 156, doi: [10.1088/0004-6256/142/5/156](https://doi.org/10.1088/0004-6256/142/5/156)
- Sullivan, M., Conley, A., Howell, D. A., et al. 2010, *MNRAS*, 406, 782, doi: [10.1111/j.1365-2966.2010.16731.x](https://doi.org/10.1111/j.1365-2966.2010.16731.x)
- Tammann, G. A., & Leibundgut, B. 1990, *A&A*, 236, 9
- Tonry, J., & Schneider, D. P. 1988, *AJ*, 96, 807,
doi: [10.1086/114847](https://doi.org/10.1086/114847)
- Trimble, V. 1996, *PASP*, 108, 1073, doi: [10.1086/133837](https://doi.org/10.1086/133837)
- . 2013, arXiv e-prints, arXiv:1307.2289.
<https://arxiv.org/abs/1307.2289>
- Tripp, R. 1998, *A&A*, 331, 815
- Tully, R. B. 2023, arXiv e-prints, arXiv:2305.11950,
doi: [10.48550/arXiv.2305.11950](https://doi.org/10.48550/arXiv.2305.11950)
- Tully, R. B., & Fisher, J. R. 1977, *A&A*, 54, 661
- Uddin, S. A., Mould, J., Lidman, C., Ruhlmann-Kleider, V., & Hardin, D. 2017a, *PASA*, 34, e009,
doi: [10.1017/pasa.2017.2](https://doi.org/10.1017/pasa.2017.2)
- Uddin, S. A., Mould, J., Lidman, C., Ruhlmann-Kleider, V., & Zhang, B. R. 2017b, *ApJ*, 848, 56,
doi: [10.3847/1538-4357/aa8df7](https://doi.org/10.3847/1538-4357/aa8df7)
- Uddin, S. A., Burns, C. R., Phillips, M. M., et al. 2020, *ApJ*, 901, 143, doi: [10.3847/1538-4357/abafb7](https://doi.org/10.3847/1538-4357/abafb7)
- Valentino, E. D., Mena, O., Pan, S., et al. 2021, In the Realm of the Hubble tension – a Review of Solutions.
<https://arxiv.org/abs/2103.01183>
- Vitale, S., & Chen, H.-Y. 2018, *PhRvL*, 121, 021303,
doi: [10.1103/PhysRevLett.121.021303](https://doi.org/10.1103/PhysRevLett.121.021303)
- Wang, L., Höflich, P., & Wheeler, J. C. 1997, *ApJL*, 483, L29, doi: [10.1086/310737](https://doi.org/10.1086/310737)
- Yang, J., Wang, L., Suntzeff, N., et al. 2022, *ApJ*, 938, 83,
doi: [10.3847/1538-4357/ac8c97](https://doi.org/10.3847/1538-4357/ac8c97)
- Zwicky, F., Humason, M. L., Gomes, A. M., & Gates, H. S. 1961, *PASP*, 73, 351, doi: [10.1086/127709](https://doi.org/10.1086/127709)